

**From static difference to time-resolved spectroscopy of coupled  
electron and proton transfer in the quinol: fumarate reductase of  
*Wolinella succinogenes***

Dissertation  
zur Erlangung des Doktorgrades  
der Naturwissenschaften

vorgelegt beim Fachbereich Biochemie, Chemie und Pharmazie  
der Johann Wolfgang Goethe-Universität  
in Frankfurt am Main

von  
**Rajsekhar Paul**  
aus Kalkutta, Indien

**Frankfurt am Main, 2011**

vom Fachbereich Biochemie, Chemie und Pharmazie der Johann Wolfgang Goethe–  
Universität als Dissertation angenommen.

Dekan: Prof. Dr. Dieter Steinhilber

1. Gutachter: Prof. Dr. Josef Wachtveitl

2. Gutachter: Prof. Dr. C. Roy D. Lancaster

Datum der Disputation: 16.08.2011

## Veröffentlichungen

---

Die meisten Ergebnisse dieser Arbeit sind veröffentlicht oder hierfür in Vorbereitung:

**Lancaster, C.R.D., Herzog, E., Juhnke, H.D., Madej, M.G., Müller, F.G., Paul, R., and Schleidt P. (2008)** Electroneutral and electrogenic catalysis by dihaem-containing succinate:quinone oxidoreductases. *Biochem. Soc. Trans.* **36**, 996-1000.

**Paul, R., Haas, A.H., Madej, M.G., Mäntele, W., and Lancaster, C.R.D. (2011)** The role of Glu C180 in the pH-dependence of the heme midpoint potentials of *Wolinella succinogenes* QFR, *manuscript in preparation*.

**Paul, R., Hellwig, P., Khoury Y., and Lancaster, C.R.D. (2011)** FTIR spectroscopic analysis of the histidine-ligand contributions in the QFR from *Wolinella succinogenes* in the low frequency spectral range, *manuscript in preparation*.

**Paul, R., Bamann C., Enela Džafić, E., Mileni, M., Fendler, K., Mäntele, W., and Lancaster, C.R.D. (2011)** Synthesis, photochemical characterisation and application of a new caged substrate:  $\alpha$ -carboxy-*o*-nitrobenzyl fumarate, *manuscript in preparation*.

## Zusammenfassung

---

Das Enzym Chinol:Fumarat-Reduktase (*engl.* quinol:fumarate reductase; QFR) des anaeroben  $\epsilon$ -Proteobakteriums *Wolinella succinogenes* katalysiert den terminalen Schritt der Fumaratatmung. Bei dieser Form der anaeroben Atmung wird Sauerstoff durch Fumarat als terminaler Elektronenakzeptor ersetzt. Die QFR ist ein dihämhaltiger Membranproteinkomplex, der die Oxidation von Menachinol zu Menachinon an die Reduktion von Fumarat zu Succinat koppelt. Beide *b*-Typ Hämgruppen (das Niedrigpotentialhäm wird auch als distales und das Hochpotentialhäm als proximales Häm *b* in der Transmembranuntereinheit C bezeichnet) sind Teil der Elektronentransportkette zwischen den zwei katalytischen Seiten des Redox-Enzyms. Obwohl die Reduktion von Fumarat durch Menachinol exergonisch ist, reicht die Energie nicht für die Erzeugung eines membrandurchspannenden elektrochemischen Protonenpotentials  $\Delta p$  aus. Es wurde bewiesen, dass diese Reaktion durch einen neuartigen Mechanismus katalysiert wird, bei dem der Transmembranelektronentransfer durch einen Transmembranprotonentransfer ermöglicht wird. Dieser neuartige, essentielle und kompensatorische Transmembranprotonentransfer (E-Weg) ist im oxidierten Zustand der QFR inaktiviert, wobei der Aminosäurerest Glu C180 der Transmembranhelix V (lokalisiert in der C-Untereinheit) und das C-Ring-Propionat des distalen Häms Schlüsselfunktionen übernehmen.

Ziel dieses Projekts war durch die Anwendung einer Kombination aus sowohl zeitaufgelösten, als auch statischen spektroskopischen Versuchen, eine detaillierte Einsicht in den Mechanismus des transmembranen, elektronengekoppelten Protonentransfers zu erhalten. Durch statische FTIR Differenzspektroskopie können Änderungen von oxidierten und reduzierten Zuständen eines Redox-Proteinsystems selektiv und sensitiv bestimmt werden. Als Techniken werden in diesem Kontext elektrochemisch induzierte FTIR Differenzspektroskopie und komplementäre computergestützte elektrostatische Berechnungen angewandt. Um den katalytischen Mechanismus der QFR zu eruieren, sind zeitaufgelöste Experimente nötig. "Rapid scan" FTIR Differenzspektroskopie erlaubt es, den Verlauf der Reaktion in einer zeitabhängigen Weise zu verfolgen. Dazu werden die zeitaufgelöste Fourier transformierte Infrarot- (tr-FTIR) und transiente Absorptionsspektroskopie verwandt. Im Folgenden werden die Details der individuellen Unterprojekte kurz erläutert.

## 1. pH-Abhängigkeit der Redox-Mittelpunktpotentiale der Hämgruppen

Die elektrostatischen Wechselwirkungen zwischen protonierbaren und redoxaktiven Gruppen resultiert in einer Kopplung von Protonierung und Reduktion in biologischen Ladungstransferreaktionen, die im Allgemeinen als Bohr-Effekt bekannt sind. Im Kontext des derzeit diskutierten Mechanismus von gekoppelten Elektronen- und Protonentransfer in der QFR von *W. succinogenes*, wurde der Aminosäurerest Glu C180 als Schlüsselkomponente des "E-pathway" identifiziert. Für die Wildtyp QFR von *W. succinogenes* wurde mittels elektrochemisch induzierter statischer FTIR Spektroskopie (im Bereich von 1800 bis 1000  $\text{cm}^{-1}$ ) gezeigt, dass die redoxabhängige Protonierung des konservierten Restes Glu C180 pH-abhängig ist.

Solche pH-Abhängigkeiten von oxidierten-reduzierten Mittelpunktpotentialen von Hämgruppen wurden schon vorher gemessen. In der vorliegenden Arbeit wurde dieses für Enzymvariante E180Q gemessen. Der Vergleich der Ergebnisse zeigt, dass der Rest Glu C180 eine Schlüsselrolle bei der Herstellung der pH-Abhängigkeit im Wildtyp-Enzym spielt. Mittels FTIR Doppeldifferenzspektroskopie konnte gezeigt werden, dass die Reduktion eines Häms für eine signifikante Protonierung des Glu C180 ausreichend ist, und dass eine sehr kleine zusätzliche Protonierung dieses Restes im vollständig reduzierten Enzym im physiologischen pH-Bereich stattfindet. Die pH-Abhängigkeit der Protonierung des Glu C180 während einer Einzelreduktion wurde auch durch korrespondierende MCCE (multiconformation continuum elektrostatischen) Berechnungen vorausgesagt. Diese pH-Abhängigkeit korreliert genau mit der pH-Abhängigkeit der Chinol-Oxidationsaktivität des Enzyms.

## 2. pH- und Redox-Abhängigkeit der individuellen Hämprophyrine und anderer relevanter Reste

In diesem Teil des Projekts werden elektrochemisch induzierte Fourier-Transformation Infrarot (FTIR) Differenzspektren von Wildtyp QFR aus *W. succinogenes* diskutiert. Der spektrale Bereich umfasst 1800-500  $\text{cm}^{-1}$  mit einer detaillierten Beschreibung des niedrigfrequenten Bereichs. Das Protein weist eine prominente Schwingungsbande bei 840-825  $\text{cm}^{-1}$  auf. Diese spezifische Bande ist pH-unabhängig, jedoch abhängig vom Oxidationszustand des Häms. Dies basiert auf der  $\gamma(\text{C}_m\text{H})$  Schwingung des Hämprophyrinrings. Weitere spektrale Eigenschaften, wie die Ringschwingung, die

empfindlich auf den Redox-Zustand des Proteins reagiert, erscheinen in der Niedrigfrequenzregion zwischen 800 und 650  $\text{cm}^{-1}$ . In einigen wichtigen Enzymen ist die Eisen-Histidin-Bindung die einzige starke Bindung zwischen der Hämgruppe und dem umgebenden Protein, deshalb ist es von großem Interesse, Eigenschaften dieser Wechselwirkungen zu charakterisieren. Die Signale bei 926 (ox), 915 (red), 864 (red) und 860 (ox)  $\text{cm}^{-1}$  sind charakteristisch für Histidinliganden, die eine markante pH-Abhängigkeit besitzen. Der Übergang des Niedrigpotential-Häms  $b_D$  trägt signifikant zum FTIR-Vollbereich-Differenzspektrum bei. Dieses weist in allen Fällen eine pH-Unabhängigkeit auf. Die axialen Histidinliganden des Niedrigpotentialhäms  $b_D$  wurden als wichtige Reste identifiziert. Die Ergebnisse deuten darauf hin, dass Protonierung, Deprotonierung und Konformationsänderungen an den Redoxübergang der Häme der QFR gekoppelt sind.

### **3. Analyse des katalytischen Mechanismus der QFR durch Verwendung von durch Lichtimpuls freigesetzter Substratbindung**

Das Interesse am Verständnis des katalytischen Reaktionsmechanismus der QFR führte zur Untersuchung der Möglichkeit, die Reaktionschemie des Enzyms durch Lichtimpuls freigesetztes Substrat (caged compounds) zu untersuchen. Ein Vorteil der Benutzung von "caged compounds" in der FTIR Differenzspektroskopie besteht darin, dass man mit dieser Methode simultan Informationen über den Redox-Zustand und über den Protonierungszustand involvierter Co-Faktoren, sowie weitere Details über die das Verhalten des Proteins erhalten kann.

"Rapid scan" FTIR ist bereits angewandt worden, um den Mechanismus der fotochemischen Freisetzung von Fumarat von seiner "caged" Fumaratvorstufe zu untersuchen. *Alpha-carboxy-o-nitrobenzyl* (CNB)-caged Substrate sind im Allgemeinen für kinetische Messungen im sub-Millisekunden Bereich geeignet. Hier wird demonstriert, dass die neu entwickelte CNB-Fumaratverbindung als fotolabiles Substrat für diese Zwecke genutzt werden kann. Die Synthese, fotochemische Charakterisierung und die Anwendbarkeit dieser neuartigen "caged compounds" wird diskutiert. Es wurden signifikante Unterschiede in der spektralen Position der spezifischen Absorptionsdifferenzbanden zwischen den kinetischen Spektren von verkapseltem Fumarat in Abwesenheit und Anwesenheit von der QFR beobachtet. Diese

Beobachtungen demonstrieren, dass die Bindung von Fumarat an die QFR im Millisekundenbereich direkt nach dem Lichtimpuls mit möglicher Beteiligung von nur einigen Bindungsstellen spezifischer Aminosäurereste vonstatten geht. Zusammengenommen hilft die exakte Erforschung der schnellen Freisetzung von Fumarat bei dem Verständnis molekularer Prozesse, die assoziiert während der katalytischen Aktivität der QFR auftreten.

Konsistent und komplementär zum vorherigen Versuch der Benutzung von caged Fumarat wurde "caged" Menachinol (*2-Methyl-3-methylamino-1,4-napthoquinone(ol)*, kurz MMAN(H<sub>2</sub>)) in einem ähnlichen Versuch zur Untersuchung kinetischer Phänomene charakterisiert. Die FTIR Differenzspektroskopie nutzt den molekularen Mechanismus mit Chinolfreisetzung aus, in dem Markerbanden für das Zielsubstrat detektiert werden. Im vorliegenden Kontext ist die bevorzugte "caging"-Gruppe *1-(4,5-dimethoxy-2-nitrophenyl)ethyl* (DMNPE). "Caged" Chinone können die Substratchinone in Lösung freisetzen, welche dabei in Lösung reduziert werden können und Chinole generieren; dadurch kann die enzymatische Reaktion der QFR eingeleitet werden. Es wurden Experimente in Anwesenheit der QFR in optimierten Versuchsbedingungen durchgeführt. Für die kontrollierten Lichtimpulse wurde der XeCl eximer Laser zusammen mit einem Bucker IFS-66 Setup benutzt.

#### **4. Bestimmung der Lebenszeit des angeregten Zustandes und der Elektronentransfergleichgewichtsrate zwischen Niedrig- und Hochpotentialhäm in der QFR**

Dieses Kapitel befasst sich mit einem Initialversuch zur Bestimmung der Lebenszeit des angeregten Zustands und der Elektronentransfergleichgewichtsrate zwischen Niedrig- und Hochpotentialhäm in der QFR. Dabei wird transiente Laser-Spektroskopie (transient ultrafast pump probe spectroscopy) mit einer Auflösung im Picosekundenbereich angewandt. Wie zuvor erwähnt besitzt die membranständige Untereinheit der QFR zwei *b*-Typ Hämgruppen, die für den transmembranen Elektronentransfer essentiell sind. Sie verbinden die zum Periplasma orientierte Stelle der Chinoloxidation mit dem Ort der Fumaratreduktion, der cytoplasmatisch in der Untereinheit A lokalisiert ist. Die Ergebnisse erlauben es, zum ersten Mal in einer zeitaufgelösten Weise, eine Reihe von widersprüchlichen Vorhersagen betreffend katalytischer Reaktionen der QFR zwischen

sowohl experimentellen, als auch theoretischen Studien betreffend zu testen. In diesem Kontext wurde die potentielle physiologische Relevanz von schnellen Gleichgewichten, die assoziiert sind mit Redoxreaktionen mit geringem elektrochemischem Potential diskutiert.



## Summary

---

The enzyme quinol:fumarate reductase (QFR) from the anaerobic  $\epsilon$ -proteobacterium *Wolinella succinogenes* is a membrane protein complex that couples the catalysis of the oxidation of menaquinol to menaquinone to that of the reduction of fumarate to succinate. This is the terminal step in fumarate respiration, a form of anaerobic respiration in which oxygen is replaced by fumarate as the terminal electron acceptor in many anaerobic microorganisms. In QFR, both the heme groups (low-potential distal and high-potential proximal heme *b* group in transmembrane subunit C) are part of the electron transport chain between the two catalytic sites of the redox enzyme. Although the reduction of fumarate by menaquinol is exergonic, it is not exergonic enough to support the generation of a transmembrane electrochemical proton potential  $\Delta p$ . Evidence has previously shown that this reaction is catalysed by a novel mechanism, involving the facilitation of transmembrane electron transfer by transmembrane proton transfer via an essential compensatory transmembrane proton transfer pathway (“E-pathway”) which is inactive in the oxidized state of the enzyme. The two key constituents of the pathway are the amino acid residue Glu C180 of the transmembrane helix V (located in subunit C) and the ring C propionate of the distal heme *b<sub>D</sub>*.

The aim of the project was to obtain, by employing a combination of time-resolved as well as static spectroscopic approaches, a detailed insight of the transmembrane electron coupled proton transfer mechanism. Minute changes in both the oxidized and reduced states of a redox protein system can be selectively and sensitively monitored by static Fourier Transformed Infrared (FTIR) difference spectroscopy. The technique employed in this context, electrochemically induced FTIR difference spectroscopy, is complemented by computer-based electrostatic calculations. In order to elucidate the catalytic mechanism of the important reactions in QFR, it is necessary to investigate these in a time-resolved manner. Rapid scan FTIR difference spectroscopy is a suitable technique that allows the course of the reaction to be monitored in a time dependent fashion. The techniques employed in this context are time-resolved (tr-FTIR) and transient absorption spectroscopy. In the following, the details of individual sub-projects are discussed in brief.

## 1. pH-dependence of the redox midpoint potentials of the heme groups

The electrostatic interactions between protonatable and redox-active groups result in the coupling of protonation and reduction in biological charge transfer reactions which is commonly known as the redox Bohr effect. In the context of the currently discussed mechanism of coupled electron and proton transfer in the QFR of *W. succinogenes*, the amino acid residue Glu C180 emerged as a key component in the “E-pathway”. For *W. succinogenes* wild-type QFR, electrochemically induced static FTIR difference spectroscopy (in the mid-infrared region from 1800 to 1000  $\text{cm}^{-1}$ ) has been employed. The study showed that the redox-dependent protonation change of the conserved residue Glu C180 is a function of pH. Comparisons of the results obtained for the E180Q variant enzyme indicated a key role of Glu C180 in establishing this pH-dependence in the wild-type enzyme. As indicated by FTIR double difference spectroscopy, single heme reduction was sufficient for significant protonation of Glu C180 to occur and there was very little additional protonation of this residue in the fully reduced enzyme in the physiological pH range. The pH dependence of the protonation of Glu C180 upon single heme reduction was also predicted by the corresponding multiconformation continuum electrostatics (MCCE) calculations. Furthermore, this pH dependence correlated perfectly with the pH dependence of the quinol oxidation activity of the enzyme.

## 2. pH- and redox-dependence of individual heme porphyrins and other relevant residues

In this part of the project, electrochemically-induced FTIR difference spectra of *W. succinogenes* wild type QFR in the spectral range from 1800-500  $\text{cm}^{-1}$  has been reported with a detailed description of the low frequency range. The protein showed a prominent vibrational band at 840-825  $\text{cm}^{-1}$ . This particular band is independent of pH but depends on the heme oxidation state. It originates from the  $\gamma(\text{C}_m\text{H})$  motion of the heme porphyrin ring. Further spectral features such as the ring vibrations sensitive to the protein's redox state are shown in the low frequency infrared region between 800 and 650  $\text{cm}^{-1}$ . It is of crucial interest to find markers for the interaction in the iron-histidine bond. The signals at 926  $\text{cm}^{-1}$  (oxidised), 915  $\text{cm}^{-1}$  (reduced), 864  $\text{cm}^{-1}$  (reduced) and 860  $\text{cm}^{-1}$  (oxidised) are characteristic of histidine ligands that demonstrate a prominent pH-dependent behaviour. In the low infrared region, there is a significant contribution of

the low potential heme  $b_D$  transition to the full range FTIR difference spectra, that is, in all cases, independent of pH. The axial histidine ligands to the low potential heme  $b_D$  are identified as important residues. Protonation/deprotonation and conformational changes are experimentally shown to be coupled to the QFR heme redox transition.

### **3. Monitoring QFR catalytic mechanism by involving photo-releasable substrates binding**

The interest in understanding the underlying catalytic reaction mechanism of QFR led to the exploration of the possibility of using photo-releasable substrate to probe the reaction chemistry of the enzyme. One of the advantages of using caged compounds in FTIR difference spectroscopy is that this method can simultaneously provide information on the redox and/or protonation state of the cofactor involved and subsequent details on the protein response.

Rapid scan FTIR spectroscopy has been applied to study the mechanism of photochemical release of fumarate from its “caged”-fumarate precursor. Alpha-carboxy-*o*-nitrobenzyl (CNB)-caged substrates are generally suitable compounds for kinetic measurements in the sub-millisecond range. Here it is demonstrated that the newly developed compound (CNB-fumarate) can be used as a photolabile substrate for this purpose. The photochemical characterisation and applicability of this novel caged-compound is reported. Significant differences in the spectral positions of specific absorbance difference bands have been observed between the kinetic traces of caged fumarate in the absence and presence of QFR. These observations demonstrate that binding of fumarate to the QFR enzyme occurs within milliseconds time window following the flash with possible involvement of only few binding site specific amino acid residues. Overall, an accurate and sensitive probing of rapid release of fumarate helps to understand the molecular processes associated during catalytic activity of QFR.

Complementary with the previous approach of employing caged fumarate, in a similar approach to study the kinetic phenomena, caged menaquinol (2-Methyl-3-methylamino-1,4-naphthoquinone(ol) (MMAN( $H_2$ )) has been characterised. The suitability of FTIR difference spectroscopy to harness the molecular mechanisms involving quinol release relies on the identification of marker bands for the target substrate and therefore detailed characterisation of the cage substance. In the present context, the preferred

caging group is 1-(4,5-dimethoxy-2-nitrophenyl)ethyl (DMNPE). Caged quinones can release the substrate quinone in solution which can thereby be reduced in solution generating quinol; and can thus trigger the QFR enzymatic reaction. Experiments were performed with the presence of QFR in optimised experimental conditions.

#### **4. Determination of excited state life time and electron transfer equilibration rate between the low- and high-potential hemes in QFR**

The two heme *b* groups in the membrane integral subunit of QFR are essential for transmembrane electron transfer linking the site of quinol oxidation oriented towards the periplasm to the site of fumarate reduction located in the cytoplasmically located subunit A. This particular study describes an initial attempt to determine the excited state life-time and an electron transfer equilibration rate between the low- and high-potential hemes in QFR by using transient ultrafast pump-probe spectroscopy with picosecond time resolution. The results allow, for the first time, in a time-resolved fashion, to test a number of conflicting predictions regarding the catalytic reactions of QFR between both experimental and theoretical studies. The potential relevance of fast equilibration associated with the low-driving-force redox reaction is discussed in this context.



*Dedicated to my beloved parents*



# Table of Contents

<b>Veröffentlichungen</b> .....	<b>iii</b>
<b>Zusammenfassung</b> .....	<b>iv</b>
<b>Summary</b> .....	<b>ix</b>
<b>List of Figures</b> .....	<b>xix</b>
<b>List of Tables</b> .....	<b>xxi</b>
<b>Symbols and Abbreviations</b> .....	<b>xxii</b>
<b>1 Introduction</b> .....	<b>1</b>
1.1 Respiration and chemiosmotic theory .....	1
1.1.1 Cellular respiration and ATP generation .....	1
1.1.2 Aerobic respiration .....	2
1.1.3 Anaerobic respiration .....	2
1.2 Anaerobic fumarate respiration in <i>Wolinella succinogenes</i> .....	3
1.3 Structural and functional properties of Quinol Fumarate Reductase (QFR).....	5
1.3.1 QFR is a member of the succinate:quinone oxidoreductases (SQORs) superfamily .....	5
1.3.2 The 3D structure and catalytic reactions in QFR .....	5
1.3.3 Catalytic sites are oriented to opposite sides of the membrane.....	7
1.3.4 Proton-coupled electron transfer (PCET) reactions in QFR .....	9
1.3.5 The E-pathway hypothesis explains the overall electroneutrality.....	10
1.3.6 Experimental evidence for E-pathway and alternative implementation of the E-pathway hypothesis.....	13
1.3.7 The redox Bohr effect and the role of Glu C180 as a key residue in the E-pathway .....	14
1.4 Static and Time-resolved Approaches Towards a Detailed Investigation of Coupled Electron and Proton Transfer in QFR.....	17
1.4.1 Static approaches .....	17
1.4.2 Time-resolved approaches .....	18
1.5 Relevance and usefulness of the employed methods.....	20
<b>2 Materials and methods</b> .....	<b>23</b>
2.1 Materials .....	23



2.1.1	List of mediators .....	23
2.1.2	List of chemicals .....	24
2.1.3	List of laboratory equipment.....	24
2.2	Infrared Spectroscopy .....	25
2.2.1	Vibrational and vibrational-rotational (infrared) spectroscopy .....	25
2.2.2	The Michelson interferometer .....	25
2.2.3	Fourier transformation.....	27
2.2.4	Fourier transform infrared spectroscopy .....	27
2.3	Electrochemistry .....	28
2.3.1	The electrochemical cell .....	29
2.3.2	Surface modification of the gold grid working electrode.....	30
2.3.3	Redox mediators.....	30
2.3.4	Electrochemically induced FTIR spectroscopy of QFR.....	30
2.4	Time-resolved FTIR difference spectroscopy .....	32
2.4.1	Caged substrates.....	32
2.4.2	Time-resolved FTIR measurements.....	35
2.4.3	ATR-FTIR microdialysis cell.....	37
2.5	Transient absorption spectroscopy .....	38
2.5.1	Sample preparation .....	38
2.5.2	Stationary spectroscopy.....	38
2.5.3	Time-resolved absorption spectroscopy .....	38
2.6	Electrostatic calculations.....	39
2.6.1	The “Multiconformation Continuum Electrostatics” (MCCE) method.....	39
2.6.2	The individual steps in MCCE calculation .....	40
2.6.3	Simulated pH titrations.....	41
<b>3</b>	<b>Results .....</b>	<b>43</b>
3.1	Electrochemically induced static FTIR approaches.....	43
3.1.1	pH-dependence of the protonation of Glu C180 with heme redox transition in QFR WT .. .....	43
3.1.2	The pH-dependence comparison of E180Q enzyme variant with wild-type enzyme ....	43
3.1.3	Individual heme porphyrin signal with heme redox transition.....	49
3.2	Time-resolved FTIR approaches.....	57
3.2.1	Caged fumarate .....	57
3.2.2	Caged 2-Methyl-3-methylamino-1,4-naphthoquinone(ol) (MMAN(H <sub>2</sub> )) .....	75

3.3	Transient absorption spectroscopy .....	81
3.3.1	Steady state absorption study of WT QFR.....	82
3.3.2	Cryo temperature static VIS redox difference spectra of WT QFR .....	83
3.3.3	Time-resolved absorption changes of WT QFR.....	86
3.3.4	Absorption anisotropy and heme reorientation dynamics in QFR.....	89
<b>4</b>	<b>Discussion.....</b>	<b>90</b>
4.1	Electrochemically induced static FTIR spectroscopic approaches.....	90
4.1.1	pH dependence of FTIR difference spectra of enzyme variant E180Q and QFR WT ...	90
4.1.2	pH and redox dependence of the individual heme porphyrin signal and other relevant residues in QFR WT.....	92
4.2	Time-resolved FTIR spectroscopic approaches.....	95
4.2.1	Comparison of the kinetic FTIR difference spectra of fumarate substrate .....	95
4.2.2	Comparison of the kinetic FTIR difference spectra of the caged MMAN with the absence and presence of QFR WT.....	97
4.3	Interheme electron transfer in the semi-reduced state of QFR WT.....	98
<b>5</b>	<b>Concluding remarks and perspectives .....</b>	<b>102</b>
<b>6</b>	<b>References.....</b>	<b>105</b>
<b>7</b>	<b>Appendix.....</b>	<b>121</b>
<b>8</b>	<b>Acknowledgements .....</b>	<b>123</b>
<b>9</b>	<b>Curriculum Vitae .....</b>	<b>126</b>

## List of Figures

<b>Figure 1</b> The schematic reaction of two-electron reduction of fumarate to succinate .....	4
<b>Figure 2</b> The scheme of anaerobic respiration in <i>Wolinella succinogenes</i> .....	4
<b>Figure 3</b> Classification of succinate:quinone oxidoreductase (SQOR) superfamily .....	5
<b>Figure 4</b> The 3-dimensional structure of <i>W. succinogenes</i> QFR .....	7
<b>Figure 5</b> Possible mechanism of fumarate reduction in <i>W. succinogenes</i> QFR. ....	8
<b>Figure 6</b> The ‘E-pathway’ hypothesis and the electron and proton transfer in the <i>Wolinella succinogenes</i> QFR.....	12
<b>Figure 7</b> Alternative implementation of the E-pathway hypothesis .....	14
<b>Figure 8</b> Graphical scheme of the redox Bohr effect mechanism .....	16
<b>Figure 9</b> The pH dependence for the redox potential of centres participating in the redox Bohr effect .....	17
<b>Figure 10</b> Optical schematic of a Michelson interferometer .....	26
<b>Figure 11</b> A schematic view of the spectroelectrochemical cell.....	29
<b>Figure 12</b> Reaction scheme for the synthesis of the CNB-fumarate.....	34
<b>Figure 13</b> The two-step reaction required for synthesizing the caged menaquinol from the menaquinone precursor of DMNPE .....	35
<b>Figure 14</b> Scheme describing a typical time-resolved FTIR measurement.....	36
<b>Figure 15</b> The pH dependence of electrochemically induced FTIR difference spectra.....	45
<b>Figure 16</b> The pH dependence of electrochemically induced FTIR double difference spectra .....	46
<b>Figure 17</b> The pH dependence of the FTIR double difference spectra of QFR WT-minus-E180Q (from 1760 to 1720 $\text{cm}^{-1}$ ).....	46
<b>Figure 18</b> The pH dependence of the FTIR double difference spectra of QFR WT-minus-E180Q at 1740 $\text{cm}^{-1}$ .....	49
<b>Figure 19</b> Oxidised-minus-reduced FTIR difference spectra of <i>W. succinogenes</i> QFR at pH 7.4 ....	50
<b>Figure 20</b> Spectral summation of trace “l” (contribution of low potential distal heme $b_D$ transition) and trace “h” (contribution of high potential proximal heme $b_P$ transition) and its comparison with full potential range spectra.....	51
<b>Figure 21</b> Superimposition of full potential range spectra at pH 7.4 and full potential range spectra at pH 8.5.....	52
<b>Figure 22</b> Oxidised-minus-reduced FTIR difference spectra of <i>W. succinogenes</i> QFR at pH 5.6; ...	53
<b>Figure 23</b> Absorption spectra of caged fumarate.....	58
<b>Figure 24</b> Photolysis of CNB-fumarate and CNB-glutamate in 50 mM K-phosphate, pH 7.4. ....	59
<b>Figure 25</b> IR absorption spectra of caged fumarate only (dotted line) and caged fumarate with WT QFR (solid line).. .....	60
<b>Figure 26</b> Photolysis mechanism of CNB-caged compounds.....	61

<b>Figure 27</b> IR absorption spectra of fumaric acid at pH 2, pH 4 and pH 8.....	62
<b>Figure 28</b> Kinetic FTIR difference bands assignment in caged fumarate with and without the presence of QFR WT .....	64
<b>Figure 29</b> Enzymatic activity of QFR. ....	66
<b>Figure 30</b> Flash photolysis of caged fumarate at different pH values .....	67
<b>Figure 31</b> Plot of exponential decay of IR difference spectral absorption intensity monitored at 1527 $\text{cm}^{-1}$ .....	68
<b>Figure 32</b> Binding of fumarate with QFR WT (in 50 mM phosphate buffer at pH 7.4) by ATR FTIR method .....	70
<b>Figure 33</b> Time dependence of FTIR difference spectra for photolysis of caged fumarate.....	73
<b>Figure 34</b> Absorption spectra of caged-MMAN.....	76
<b>Figure 35</b> FTIR absorption spectra of the MMAN and caged-MMAN. ....	77
<b>Figure 36</b> Characterisation of FTIR bands after caged MMAN photolysis.....	78
<b>Figure 37</b> Kinetic FTIR difference bands assignment in caged MMAN .....	80
<b>Figure 38</b> Absorption spectra of QFR WT at pH 7.4 in two different redox states. ....	83
<b>Figure 39</b> Changes in absorption spectra of fully reduced QFR measured at a temperature range from 298K to 88K .....	84
<b>Figure 40</b> Plot of the absorption maxima for the $\alpha$ - band and $\beta$ - band with the variation of temperatures .....	84
<b>Figure 41</b> Changes in absorption spectra of fully oxidised QFR measured at a range of temperatures ranging 298K to 96K .....	85
<b>Figure 42</b> Comparison of transient absorbance changes of QFR WT sample probed at 558 nm.....	87
<b>Figure 43</b> Temporal evolution of difference absorption spectra of semi-reduced QFR.....	88
<b>Figure 44</b> Transient bleach VIS absorption spectra of QFR semi-reduced redox state under 0.1 ps and 1 ps time delay. ....	89
<b>Figure 45</b> Oxidation-reduction (midpoint) potentials (in mV) of the constituents of the electron transport chain of the <i>W. succinogenes</i> QFR.....	100
<b>Figure 46</b> The simulated pH dependence of the occupancy of Glu <sup>0</sup> C180 as a function of the four considered heme redox states. ....	122
<b>Figure 47</b> The simulated pH dependence of the difference in occupancy of Glu <sup>0</sup> C180 as a function of the four considered heme redox states. ....	122

## List of Tables

<b>Table 1</b> Redox midpoint potential ( $E_m$ ) of the cofactors from the <i>W. succinogenes</i> QFR.....	9
<b>Table 2</b> List of mediators for electrochemical measurements. ....	23
<b>Table 3</b> List of chemicals. ....	24
<b>Table 4</b> List of laboratory equipment.....	24
<b>Table 5</b> Summary of tentative IR band assignments (from $1000\text{ cm}^{-1}$ to $600\text{ cm}^{-1}$ ) for <i>W. succinogenes</i> QFR.....	56
<b>Table 6</b> Summary of tentative IR band assignments for CNB-fumarate dissociation. ....	63
<b>Table 7</b> Summary of tentative IR band assignments for <i>W. succinogenes</i> QFR.....	63
<b>Table 8</b> Summary of tentative IR band assignments for caged MMAN( $\text{H}_2$ ) dissociation.....	78
<b>Table 9</b> The simulated pH dependence of the occupancy of Glu <sup>0</sup> C180 as a function of the four considered heme redox states. ....	121
<b>Table 10</b> The simulated pH dependence of the difference in occupancy of Glu <sup>0</sup> C180 as a function of the four considered heme redox states. ....	121

## Symbols and Abbreviations

$^1\text{H}/^2\text{H}$	hydrogen/deuterium;
3D	three dimensional
$^{\circ}\text{C}$	celsius degrees
ADP	adenosine diphosphate
Å	angstrom(s)
AAPH3	2,2'-azobis(2-amidino-propane) dihydrochloride
ATP	adenosine triphosphate
BCMB	3',5'-bis(carboxymethoxy)benzoin
BISTRIS	Bis-(2-hydroxy-ethyl)-amino-tris(hydroxymethyl) methane
CHES	(2-(Cyclohexylamino)-ethanesulphonic acid)
cmc	critical micelle concentration
CNB	$\alpha$ -carboxy- <i>o</i> -nitrobenzyl caging group
cyt. <i>b</i>	cytochrome <i>b</i>
$\delta$	bending vibration
$\Delta E$	redox difference potential
$\Delta G$	free energy (Gibbs)
$\Delta H_c$	energy of reaction (kJ/mole)
$\Delta p$	electrochemical proton potential
$\Delta \text{pH}$	transmembrane proton gradient
$\Delta \psi$	transmembrane potential gradient
Da	dalton
DCNB	dicarboxy-2-nitrobenzyl
DEAD	diethyl azodicarboxylate
DM	decyl maltoside
DMB	3',5'-dimethoxybenzoin
DMN	2,3-dimethyl-1,4-naphthoquinone
DMNH <sub>2</sub>	2,3-dimethyl-1,4-naphthoquinol
DMNPE	1-(4,5-dimethoxy-2-nitrophenyl)ethyl
DMSO	dimethylsulfoxide
DTGS	deuterated triglycine sulfate
DTT	dithiothreitol
$E_h$	environmental redox potential
$E_m$	redox midpoint potential
EC	enzyme classification
EDTA	ethylenediaminetetraacetic acid
ET	electron transfer
ETC	electron transfer chain
EtOH	ethanol
FAD	flavin-adenine dinucleotide
Fdh	formate dehydrogenase
FMN	flavin mononucleotide
Frd	fumarate reductase
FTIR	Fourier transformed infrared
Fum	fumarate
Heme <i>b<sub>D</sub></i>	distal heme <i>b</i>
Heme <i>b<sub>P</sub></i>	proximal heme <i>b</i>

Heme $b_H$	high potential heme $b$
Heme $b_L$	low potential heme $b$
HEPES	4-(2-hydroxyethyl)-1-piperazineethanesulfonic acid
$I_{\max}$	maximum absorbance intensity
IR	infrared
JWGU	Johann Wolfgang Goethe University
$KP_i$	potassium phosphate
LM	laurylmaltoside (n-dodecyl- $\beta$ -D-maltoside)
MCCE	multiconformation continuum electrostatics
MCT	mercury-cadmium-telluride
MD	molecular dynamics
MES	morpholinoethanesulfonic acid
Min	minute(s)
MK $_{-n}$	menaquinone-n (according to IUPAC-IUB)
MKH $_2$ $_{-n}$	menaquinol-n
mM	millimolar
MMAN	2-Methyl-3-methylamino-1,4-naphthoquinone
MMAN(H $_2$ )	2-Methyl-3-methylamino-1,4-naphthoquinon(ol)
MPIBP	Max Planck Institute of Biophysics
ms	millisecond
mV	millivolt(s)
MW	molecular weight
$\nu$	vibrational frequency
$\nu_{as}$	the antisymmetric stretching vibration
$\nu_s$	the symmetric stretching vibration
$n=1$	one electron involved
NADH	nicotinamide adenine dinucleotide
nm	nanometers
NPE	1-(2-nitrophenyl)ethyl
OD	optical density
$\pi^*$	pi star, anti-bonding orbital
PDB	protein data bank
PMF	proton motive force
PT	proton transfer
ps	picosecond
QFR	quinol:fumarate reductase
RC	reaction centre;
RT	room temperature
SDS	sodium dodecyl sulfate
SHE	standard hydrogen electrode
SQORs	succinate:quinone oxidoreductases
SQR	succinate:quinone reductase
TFA	trifluoroacetic acid
THF	tetrahydrofuran
Tris	tris-(hydroxymethyl)-aminomethane
U	enzymatic unit
UV	ultraviolet
UQ	ubiquinone (according to IUPAC-IUB)

V	volt
VDW	van der Waals
VIS	visible
vitK <sub>2</sub>	vitamin K <sub>2</sub> (= MK-4)
WT	wild type



# 1 Introduction

## 1.1 Respiration and chemiosmotic theory

### 1.1.1 Cellular respiration and ATP generation

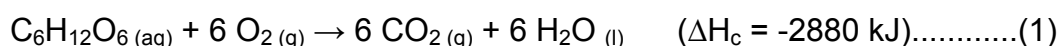
A cell can harvest energy from food by the means of cellular respiration. Cellular respiration consists of metabolic reactions and processes that take place in a cell or across the cell membrane to obtain biochemical energy from the oxidation of fuel molecules (e.g. glucose, amino acids, fatty acids etc.). The energy released is stored as "high-energy" carriers. Glycolysis, the first step of process, is the breakdown or splitting of glucose into pyruvic acid. The second step, oxidative phosphorylation, is the complete oxidation of pyruvic acid to carbon dioxide and water where electrons are transferred from electron donors to electron acceptors such as oxygen, in oxidation-reduction ("redox") reactions.

Organisms that use oxygen as a final electron acceptor in respiration are described as aerobic. There are organisms, however, that can respire using organic molecules as terminal electron acceptors instead of oxygen. These are referred to as anaerobic. The redox reactions in oxidative phosphorylation release energy, which is used to form adenosine triphosphate (ATP). In eukaryotes, these redox reactions are carried out by a series of protein complexes within mitochondria, whereas in prokaryotes, these proteins are located in inner membranes of the cell. These linked sets of enzymes are called electron transport chains. In eukaryotes, five major protein complexes are involved, whereas in prokaryotes many different enzymes are present, using a variety of electron donors and acceptors depending on adaptation with respect to environment. The energy released as electrons flowing through this electron transport chain is used to transport protons across the inner mitochondrial membrane, in a process called chemiosmosis.

The "chemiosmotic hypothesis" postulated by Peter Mitchell (Mitchell, 1961) states that chemiosmosis generates potential energy in the form of a pH gradient and an electrical potential ( $\Delta p$ ) across this membrane. This storage of energy is tapped by allowing protons to flow back across the membrane and down this thermodynamic gradient, through ATP synthase. The latter uses this energy to generate ATP from adenosine diphosphate (ADP) (Voet *et al.*, 1999).

### 1.1.2 Aerobic respiration

Aerobic respiration is the release of energy from glucose or other organic substrates in the presence of oxygen. Aerobic respiration is divided into three processes: glycolysis, Krebs cycle and the electron transport chain, which produces ATP through chemiosmotic phosphorylation. After the pyruvate broken down from glycolysis, it enters the mitochondrion to be fully oxidized by the Krebs cycle. The product of this process is energy in form of ATP by substrate-level phosphorylation, NADH and FADH<sub>2</sub>. The energy conversion is as follows:

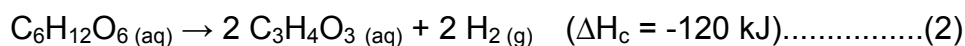


The post glycolytic reactions take place in the mitochondria in eukaryotic cells, and in the cytoplasm (or mitochondrial matrix) in prokaryotic cells. In mitochondria, respiratory enzyme complexes (complex I-V) are anchored in the inner membrane. Three (complex I, III, and IV) of them are proton pumps. Complex I (NADH coenzyme Q reductase) transfers electrons from the Krebs cycle electron carrier nicotinamide adenine dinucleotide (NADH), to ubiquinone, which also receives electrons from succinate via complex II (succinate dehydrogenase). Complex III (cytochrome *bc*<sub>1</sub> complex) catalyses electron transfer from the quinol (QH<sub>2</sub>) to cytochrome *c* (cyt *c*). Complex IV (cytochrome *c* oxidase) uses the electrons and hydrogen ions to reduce molecular oxygen to water. The electrochemical proton potential generated therein is finally used by complex V (ATP synthase) for the production of ATP from ADP and inorganic phosphate.

### 1.1.3 Anaerobic respiration

Although all eukaryotes are strictly aerobes, prokaryotes can use terminal electron acceptors other than oxygen, such as nitrate (NO<sub>3</sub><sup>-</sup>), nitrite (NO<sub>2</sub><sup>-</sup>), sulphate (SO<sub>4</sub><sup>2-</sup>), fumarate, dimethyl sulfoxide (DMSO) and others in their different modified respiratory systems (Enger, 2003), (Karp, 2008). Anaerobic respiration is far less efficient than aerobic respiration, but many organisms can use it when necessary, usually when oxygen is lacking. These are called facultative anaerobes and include yeasts and other fungi, bacteria, parts of plants such as germinating seeds and waterlogged roots, certain worms and similar animals found in stagnant water or at the sea-bottom, and mammalian muscle cells. A few bacteria and similar microbes are obligate anaerobes

because they can not use oxygen at all, oxygen being highly poisonous to them. Without oxygen, pyruvate is not metabolized by cellular respiration, rather undergoes a process of fermentation. The pyruvate is not transported into the mitochondrion, but remains in the cytoplasm. Anaerobic respiration is less efficient at using the energy from glucose since 2 ATP are produced during anaerobic respiration per glucose, compared to the 30 ATP per glucose produced by aerobic respiration. Anaerobic respiration may be used by a cell even before the oxygen levels are depleted. The results are usually substances such as lactic acid (lactate), pyruvic acid (pyruvate) or ethyl alcohol (ethanol). The reaction can be represented by the general chemical equation:



## 1.2 Anaerobic fumarate respiration in *Wolinella succinogenes*

*Wolinella succinogenes*, a member of  $\epsilon$ -subclass of the proteobacteria, performs oxidative phosphorylation with fumarate instead of molecular oxygen as terminal electron acceptor and molecular hydrogen or formate as electron donors (Kröger and Innerhofer, 1976), (Kröger *et al.*, 2002), (Lancaster, 2004). Fumarate respiration, defined by the reduction of fumarate by the above donors, is catalyzed by an electron transport chain in the bacterial membrane and the free energy associated with the electron transfer reactions is responsible for the generation of a transmembrane electrochemical proton potential ( $\Delta p$ ) across the bacterial membrane. The proton potential in turn drives the reaction catalysed by the ATP synthase. The fumarate respiratory chain, shown in Figure 2, consists of hydrogenase, fumarate reductase, formate dehydrogenase and the ATP synthase. Fumarate respiration is the most commonly occurring type of anaerobic respiration, probably due to the fact that fumarate can be formed from the common substances of life (e.g. carbohydrates and proteins).

The enzyme quinol:fumarate reductase (QFR) is a diheme-containing membrane protein complex that couples the two-electron reduction of fumarate to succinate (reaction 1, Figure 1) to the two-electron oxidation of the low-potential menaquinol to menaquinone (reaction 2, Figure 1). QFR is also able to catalyse the reverse reaction *in vitro* (Lemma *et al.*, 1991) and can thus also operate as a succinate:quinone reductase

(SQR). Menaquinone-6 and methyl-menaquinone-6 (both are derivatives of 1, 4-naphthoquinone with a six isoprenyl side chain) are the major quinone species (Lancaster and Simon, 2002) involved here. The high potential quinones are generally used in aerobic respiration and the low potential quinones are used in bacterial anaerobic respiration (Figure 2).

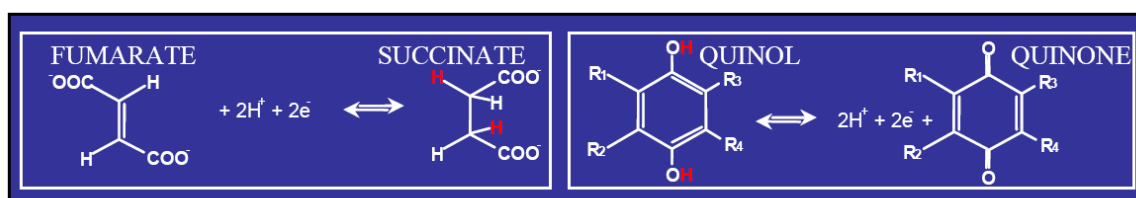


**Figure 1** The schematic reaction of two-electron reduction of fumarate to succinate (reaction 1) to the two-electron oxidation of quinol to quinone (reaction 2) (Kröger *et al.*, 1992), (Lancaster, 2004), (Lemma *et al.*, 1991).

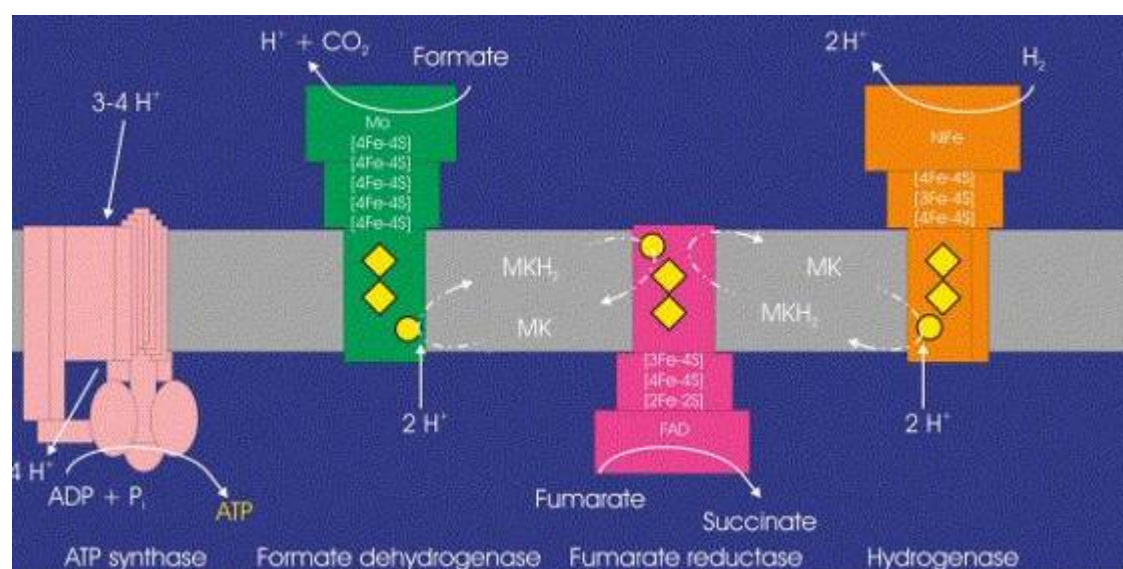


**Figure 2** The scheme of anaerobic respiration in *Wolinella succinogenes* (Lancaster, 2003). The key enzymes involved in fumarate respiration are shown here. The MK/MKH<sub>2</sub> indicates menaquinone/menaquinol couple. QFR is shown in pink.

## 1.3 Structural and functional properties of Quinol Fumarate Reductase (QFR)

### 1.3.1 QFR is a member of the succinate:quinone oxidoreductases (SQORs) superfamily

Succinate:quinone reductase (SQR or aerobic respiratory “complex II”) (Cecchini, 2003), (Lancaster, 2004), (Saraste, 1999) catalyzes the oxidation of succinate by quinone, the reverse reaction to that catalysed by QFR. Both SQR and QFR complexes together constitute the succinate:quinone oxidoreductases (SQORs; EC 1.3.5.1) superfamily (Hägerhäll, 1997), (Lancaster and Simon, 2002), (Lancaster, 2003), (Ohnishi *et al.*, 2000). SQORs are classified in five different types (A-E) (Figure 3) based on their individual hydrophobic domain and heme content. QFR from *W. succinogenes* is a type “B” SQOR having one hydrophobic subunit C and two heme groups, one proximal and another distal with respect to the hydrophilic subunit (Lancaster *et al.*, 1999). As QFR and SQR catalyze the same reaction in both directions, they can be distinguished only based on the direction of the catalysed reaction *in vivo*.

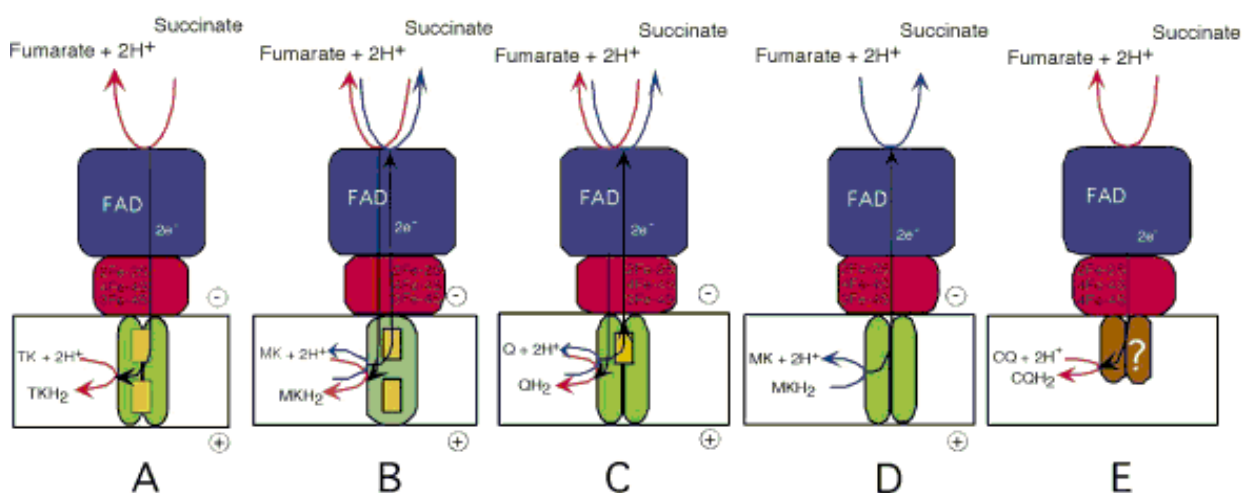


**Figure 3** Classification of succinate:quinone oxidoreductase (SQOR) superfamily. The integral transmembrane subunits (in green) can contain heme groups (yellow rectangles). The hydrophilic subunits are drawn in red (subunit B) and blue (subunit A) (modified from (Lancaster, 2001)).

### 1.3.2 The 3D structure and catalytic reactions in QFR

The 3D structure of two different crystal forms (A and B) of *W. succinogenes* QFR in its oxidized state has been previously solved at resolutions of 2.2 and 2.33 Å, respectively (PDB ID 1QLA and 1QLB, respectively) (Lancaster *et al.*, 1999). The structure is shown

in Figure 4. Recently an improved crystal structure was solved at 1.78 Å resolution (PDB ID 2BS2) (Madej *et al.*, 2006a).

The enzyme is a homo-dimer and each monomer comprises two hydrophilic subunits (FrdA & FrdB with their respective molecular masses 73 kDa and 27 kDa) and one hydrophobic, membrane-integrated subunit FrdC (molecular mass 30 kDa). The larger hydrophilic subunit A contains a covalently bound flavin adenine dinucleotide (FAD), the smaller hydrophilic subunit B contains three iron-sulphur clusters ([2Fe-2S], [4Fe-4S], [3Fe-4S]) and the hydrophobic subunit C contains two heme *b* groups, proximal heme  $b_P$  and distal heme  $b_D$  (proximal and distal convention is used according to their relative proximity to the hydrophilic subunits A and B). Heme  $b_P$  corresponds (Haas and Lancaster, 2004) to the “high-potential” heme  $b_H$  ( $E_{m,7} = -9$  mV) (Lancaster *et al.*, 2000) and heme  $b_D$  to the low-potential heme  $b_L$  ( $E_{m,7} = -152$  mV) (Lancaster *et al.*, 2000).

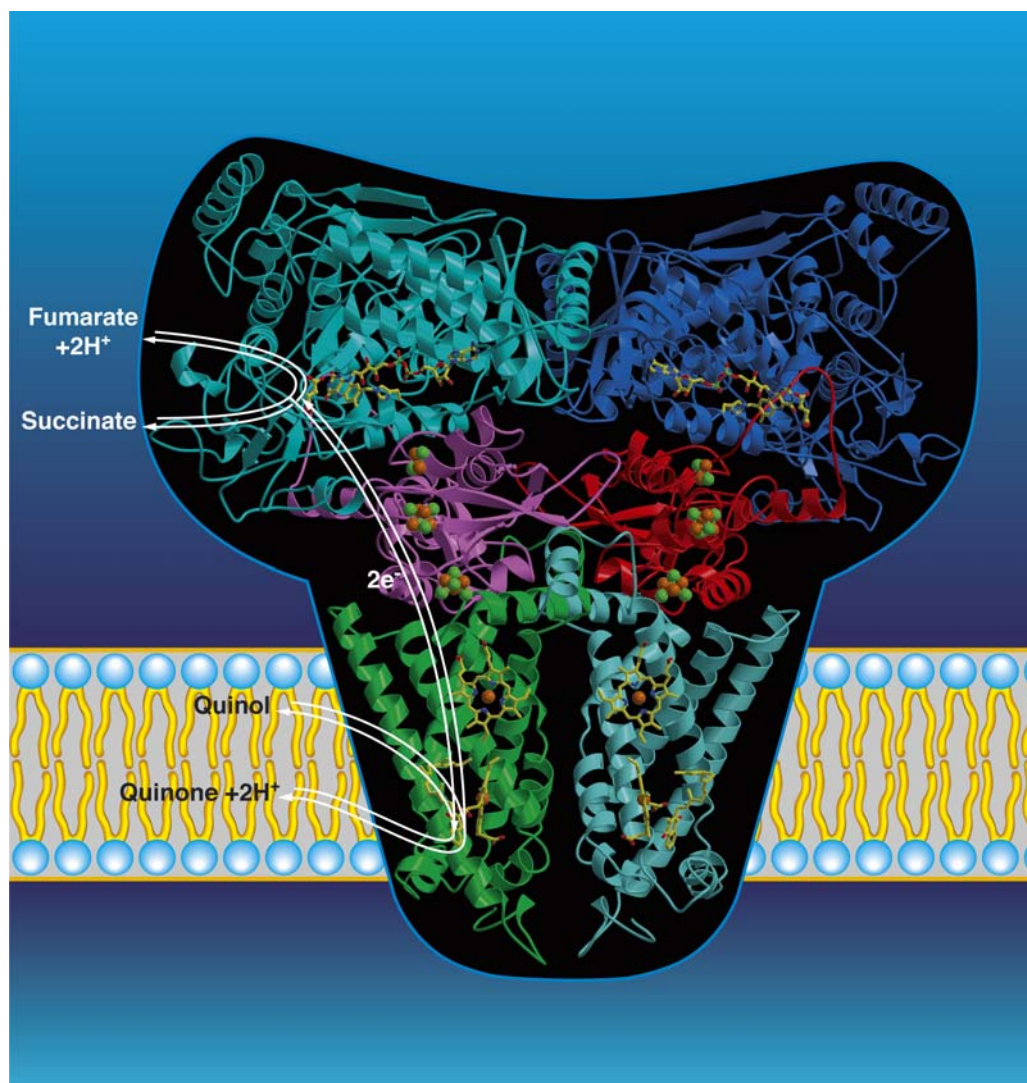


**Figure 4** The 3-dimensional structure of *W. succinogenes* QFR homo-dimer of the hetero-trimeric complexes of subunits A (turquoise and blue), B (purple and red) and C (green and light blue) (Lancaster *et al.*, 1999). The six prosthetic group in each hetero-trimer are the covalently-bound FAD, the [2Fe-2S], the [4Fe-4S] and the [3Fe-4S], the proximal heme ( $b_H$ ) and the distal heme ( $b_L$ ).

### 1.3.3 Catalytic sites are oriented to opposite sides of the membrane

As evident from the high-resolution X-ray structure of *W. succinogenes* QFR, the binding site of succinate/fumarate is located between the FAD-binding domain and the capping domain next to the plane of the FAD isoalloxazine ring (Lancaster, 2004), (Lancaster *et al.*, 2001). The polar nature due to the H-bonding environment around the carboxylic groups generates a positive charge at the C- $\beta$  position of the polarised fumarate (Figure 5). The hydride transfer to this C- $\beta$  position from FAD cofactor along with protonation at

C- $\alpha$  by an arginine located at the opposite side of fumarate catalytic site constitutes the reduction of fumarate with two protons (Lancaster *et al.*, 2001).

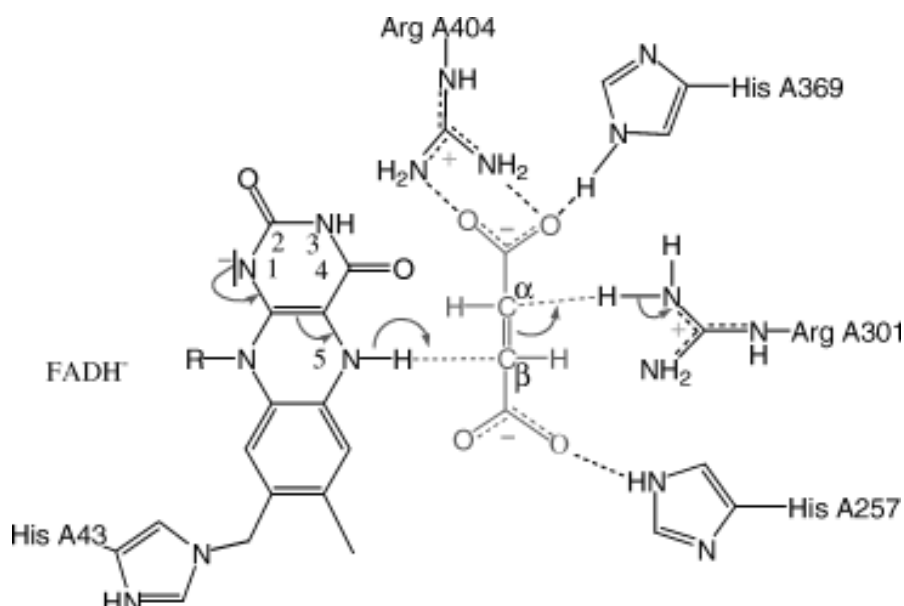


**Figure 5** Possible mechanism of fumarate reduction in *W. succinogenes* QFR. Hydride transfer from the N5 of FAD to the  $\beta$ -methylene of fumarate is coupled to proton transfer to the position of the substrate from the side chain of Arg A301 (Lancaster *et al.*, 2001).

The site for menaquinol oxidation is located distally, close to the periplasmic site of the membrane and close to the low potential heme  $b_D$  (Lancaster *et al.*, 2000). The functional role and location of the glutamate residue (FrdC-E66) indicates that this particular residue plays a vital role in transferring two protons which are liberated upon menaquinol oxidation in the hydrophobic phase can be released on the periplasmic aqueous phase.

Catalytic functionality of QFR, therefore, couples the two-electron reduction of fumarate to succinate to the two-electron oxidation of menaquinol to menaquinone, transferring electrons from periplasmic quinol-oxidising site to the cytoplasmic fumarate-reducing site. The linear arrangement of the prosthetic groups in the complex (Figure 4) provides a straight forward pathway by which electrons could be transferred efficiently between the two sites of catalysis (Lancaster, 2004). In case of electron transfer proteins, it has been postulated (Page *et al.*, 1999) that physiological electron transfer between prosthetic groups occurs if their edge-to-edge distance is shorter than 14 Å.



Based on this, efficient electron tunnelling can only be ensured in case of the cofactors of each single heterotrimer in QFR, but not between the two different monomers.

The redox midpoint potentials ( $E_m$ ) of the cofactors are summarized in Table 1 and taken from the references mentioned in Table 1. Furthermore, calculation of the electron transfer rate constants between cofactors has allowed identification of the rate-limiting steps of the catalytic reaction (Figure 4).

**Table 1** Redox midpoint potential ( $E_m$ ) of the cofactors from the *W. succinogenes* QFR. The titration of heme groups was determined at pH 7.0, iron-sulphur clusters and FAD at pH 7.3 (Mileni *et al.*, 2006). The midpoint potentials for MK/MKH<sub>2</sub> and fumarate/succinate couples were taken from (Lancaster, 2004), (Lancaster *et al.*, 2000).

Cofactor type	$E_m$ (mV)
Fumarate/Succinate	25
FAD <sup>-</sup>	-125
[2Fe-2S] <sup>2+/1+</sup>	-112
[4Fe-4S] <sup>2+/1+</sup>	-340
[3Fe-4S] <sup>1+/0</sup>	-61
Proximal heme	-9
Distal heme	-152
MK/MKH <sub>2</sub>	-75

The establishment of various enzymatic activity assays on QFR (Lancaster *et al.*, 2000), (Lancaster *et al.*, 2005) has provided powerful methods for its functional study. The QFR from *W. succinogenes* is a highly active membrane protein complex with turnover times (i.e. the inverse of turnover rates) in the range of tens of milliseconds (calculated from a specific activity of 7.4 U mg<sup>-1</sup> (Lancaster *et al.*, 2000)).

### 1.3.4 Proton-coupled electron transfer (PCET) reactions in QFR

The orientation of the catalytic sites of fumarate reduction (Lancaster *et al.*, 2001), associated with proton binding, and menaquinol oxidation (Lancaster *et al.*, 2000), associated with proton release, towards opposite sides of the membrane indicated that quinol oxidation by fumarate should be an electrogenic process in *W. succinogenes* (Figure 4), i.e. associated directly with the establishment of an electrochemical proton

potential across the membrane. Support for the  $\Delta p$  and  $\Delta pH$  generation came from the experiments of some diheme-containing representatives of the superfamily of QFRs and succinate:menaquinone reductases (SQRs). When quinones with finely-tuned oxidation/reduction potential were used, the succinate:menaquinone reductase from *Bacillus licheniformis* supported the  $\Delta p$  generation making the otherwise thermodynamically unfavourable oxidation of succinate by menaquinol (Madej *et al.*, 2006b). However, analogous experiments for isolated *W. succinogenes* QFR reconstituted into liposomes had shown that the oxidation of quinol by fumarate as catalysed by this enzyme is an electroneutral process (Biel *et al.*, 2002), (Geisler *et al.*, 1994), (Kröger *et al.*, 2002), (Madej *et al.*, 2006b).

### 1.3.5 The E-pathway hypothesis explains the overall electroneutrality

To reconcile these apparently conflicting experimental observations mentioned in 1.3.4, the so-called ‘E-pathway hypothesis’ (Lancaster, 2002) was proposed (Figure 6). According to this working hypothesis, the transmembrane transfer of two electrons in *W. succinogenes* QFR is coupled to the compensatory, parallel translocation of one proton per electron from the periplasm to the cytoplasm. The proton transfer pathway used is transiently established during reduction of the heme groups and is closed in the oxidised enzyme. Two most prominent constituents of this suggested pathway are thought to be the ring C propionate of the distal heme  $b_D$  and, in particular, the amino acid residue Glu C180, after which the “E-pathway” was named (Figure 6). Since the first proposal of this hypothesis, a number of theoretical (Haas and Lancaster, 2004) and experimental results (Haas *et al.*, 2005), (Lancaster *et al.*, 2005), (Mileni *et al.*, 2005) have been obtained that support it (reviewed in (Lancaster *et al.*, 2006), (Lancaster *et al.*, 2005)).

A combination of  $^{13}C$  labelling of the heme propionates (Mileni *et al.*, 2005) with redox-induced FTIR experiments and multiconformation continuum electrostatics (MCCE) calculations (Haas and Lancaster, 2004) support a (de)protonation event, possibly accompanied by a conformational change (of at least one of the two distal heme propionates) upon heme reduction. Since it was established that the ring D propionate of the low-potential heme is involved in an extensive salt-bridge interaction with a nearby Arg residue (Haas and Lancaster, 2004), (Lancaster *et al.*, 1999) the

obvious candidate for the observed effects is the ring C propionate, which is fully consistent with the proposed role of the residue in the E-pathway hypothesis.

The Glu C180 residue is conserved in all  $\epsilon$ -proteobacterial diheme-containing QFR enzymes (Lancaster, 2002). The essential role of Glu C180 residue was first supported by multiconformation continuum electrostatics calculations (Haas and Lancaster, 2004), which predicted that this residue undergoes the combination of a change in protonation and conformation upon reduction of the heme groups, a result that was also obtained experimentally by the combination of FTIR difference spectroscopy (Haas *et al.*, 2005) and site-directed mutagenesis, involving the replacement of Glu C180 with a Gln residue (Lancaster *et al.*, 2005). The mutant E180Q was unable to grow with fumarate as the terminal electron acceptor. The mutant did grow when fumarate was replaced by nitrate and the variant QFR was produced. After refining the structure of the variant QFR at 2.2 Å resolution, any major structural changes compared to the structure of the wild-type enzyme was ruled out (Lancaster *et al.*, 2005).

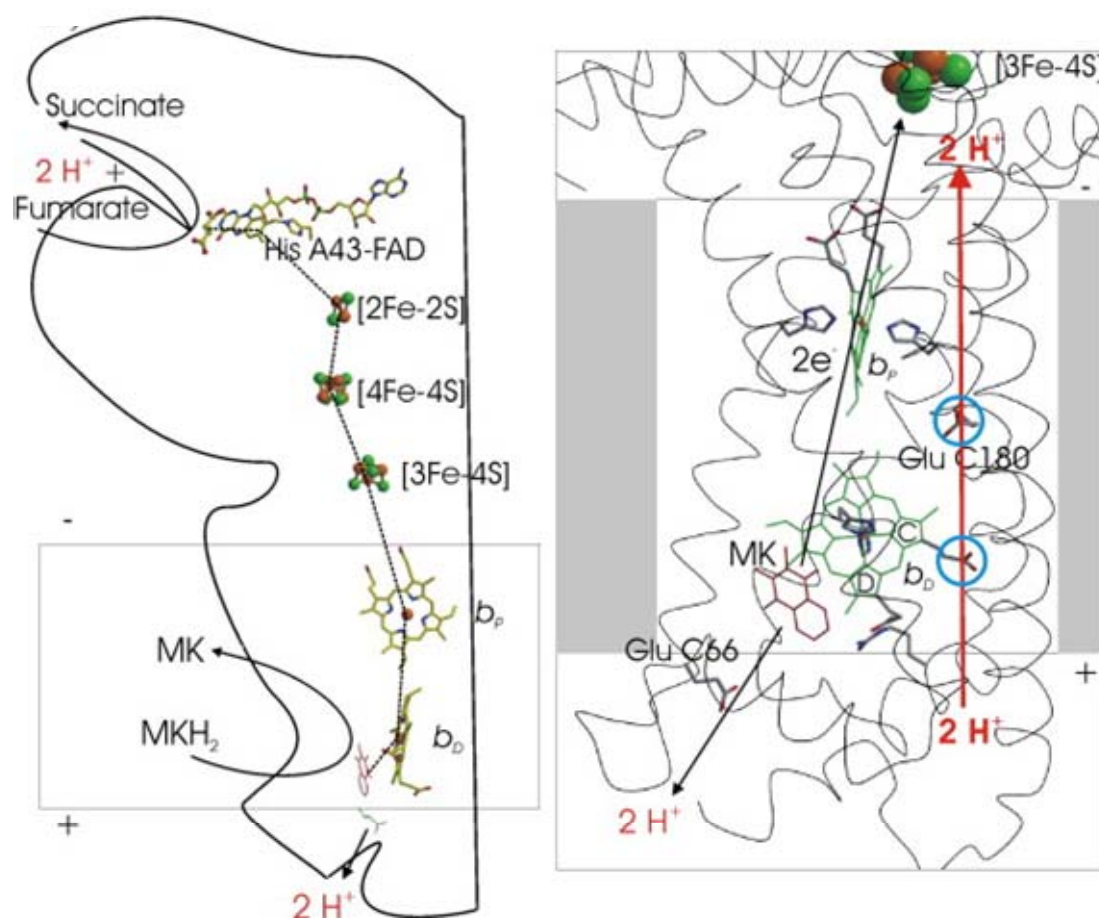


**Figure 6** The ‘E-pathway’ hypothesis and the electron and proton transfer in the *Wolinella succinogenes* QFR. (Lancaster, 2002), (Lancaster *et al.*, 2006). On the left side, hypothetical  $\Delta p$  generation is shown as suggested by the essential role of Glu C66 for menaquinol oxidation by *W. succinogenes* QFR (Lancaster *et al.*, 2000). The prosthetic groups of the *W. succinogenes* QFR dimer are displayed (coordinate set 1QLA; (Lancaster *et al.*, 1999)). Also indicated are the side chain of Glu C66 and a tentative model of menaquinol ( $MKH_2$ ) binding, based on the coordinates of QFR-bound DMN (PDB entry 2BS4 (Lancaster *et al.*, 2005)). The position of bound fumarate is taken from PDB entry 1QLB (Lancaster *et al.*, 1999). The arrangement of the prosthetic groups such as heme  $b_d$ , heme  $b_p$ , [3Fe-4S], [4Fe-4S], [2Fe-2S] and FAD as well as determined midpoint ( $E_m$ ) potentials (Table 1) suggest that electron transfer is proceeding in such an order. On the right side, “E-pathway hypothesis” is depicted. The two protons that are liberated upon oxidation of menaquinol ( $MKH_2$ ) are released to the periplasm (bottom) via the residue Glu C66. In compensation, coupled to electron transfer via the two heme groups, protons are transferred from the periplasm via the ring C propionate of the distal heme  $b_d$  and the residue Glu C180 (indicated by the blue circles) to the cytoplasm (top), where they replace those protons which are bound during fumarate reduction. In the oxidised state of the enzyme, the “E-pathway” is blocked. However, upon reduction, the ‘E-pathway’ is open.

### 1.3.6 Experimental evidence for E-pathway and alternative implementation of the E-pathway hypothesis

Non-functionality of the 'E-pathway' in the E180Q variant gave rise to the electrogenicity of catalysis. This came from the observation that the variant E180Q was only very weakly catalytically active upon 2,3-dimethyl-1,4-naphthoquinol (DMNH<sub>2</sub>) oxidation by fumarate and the addition of the protonophore carbonyl cyanide *m*-chlorophenylhydrazone (CCCP) enabled the catalysis of DMNH<sub>2</sub> oxidation (Madej *et al.*, 2006a). Initially, the problem to detect the  $\Delta p$  in the E180Q variant was attributed to the small difference in the oxidation-reduction midpoint potential between the 2,3-dimethyl,1,4-naphthoquinone (DMN/DMNH<sub>2</sub>) couple ( $E_m = -35$  mV) (and the fumarate/succinate) couple, making the overall reaction only mildly exergonic ( $\Delta G \approx -12$  kJ/mol) under standard conditions at pH 7 (Madej *et al.*, 2006a). Therefore, a substrate analogue with lower redox midpoint potential, namely the 2-methyl-3-methylamino-1,4-naphthoquinone (MMAN), was designed. The advantage of the MMAN/MMANH<sub>2</sub> couple was its lower redox potential compared to that of the DMN/DMNH<sub>2</sub> couple, ( $\Delta E_m = -90$  mV (Madej *et al.*, 2006a)), thus increasing the  $\Delta G$  of the reaction from  $\Delta G \approx -12$  kJ/mol to  $\Delta G \approx -30$  kJ/mol under standard conditions at pH 7 (Madej *et al.*, 2006a) and, in principle, providing sufficient driving force for the establishment of  $\Delta p$  in the direction of quinol oxidation by fumarate.

In contrast to the results obtained with the wild-type enzyme, quinol oxidation by the E180Q variant was clearly associated with an acidification of the interior of the proteoliposomes (the generation of a proton gradient,  $\Delta pH$ ) (Madej *et al.*, 2006a) as well as TPB<sup>-</sup> entry into the proteoliposomes (the generation of a membrane potential  $\Delta\psi$ ) (Madej *et al.*, 2006a). Taken together with the results obtained for the proteoliposomal wild-type enzyme, these results clearly demonstrate the presence and absence of the "E-pathway" in the WT and E180Q-variant enzymes, respectively (Madej *et al.*, 2006a).

While the E-pathway hypothesis as depicted in Figure 6 is the simplest model compatible with the experimental data obtained so far, it is by no means unique. The simplifying assumption that both protons released upon quinol oxidation are released via the same pathway may turn out not to be true, as may the assumption that both E-pathway protons have the same entry point. In particular, the scenario that one proton is transferred directly from the quinol oxidation site to the E-pathway (Figure 7) also

explains the available data. However, there is no such proton transfer connectivity apparent from the structure of the oxidised enzyme, so this scenario would require an appropriate conformational change during catalysis (Lancaster *et al.*, 2008), (Madej *et al.*, 2009).

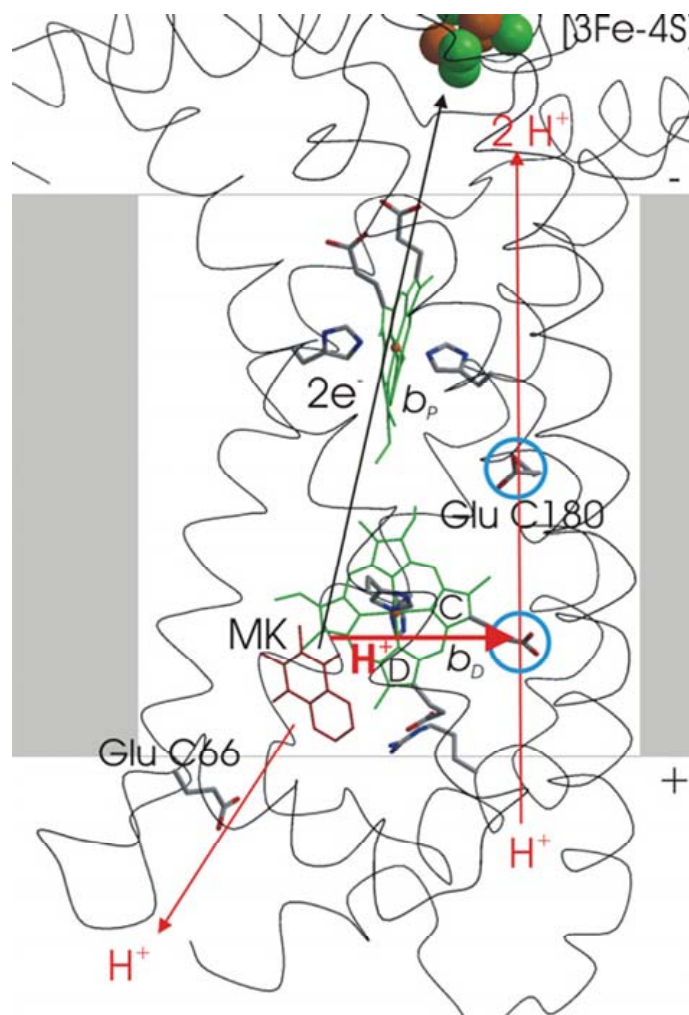


**Figure 7** Alternative implementation of the E-pathway hypothesis. (Lancaster *et al.*, 2008), (Madej *et al.*, 2009)

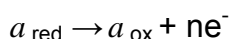
### 1.3.7 The redox Bohr effect and the role of Glu C180 as a key residue in the E-pathway

Functional cooperativity between specific protein centres plays a major role in global regulation in protein functionality. Change of the redox state of a single metal ion, for instance, within the protein structure can impair the proton effectors to bind (or unbind) to a particular residue or charged group. This coupled electrostatic interaction between

the redox-active groups and the protonable residues is called redox Bohr effect in biological redox proteins (Papa *et al.*, 1998). In many complex redox-active membrane bound proteins, this electron/proton linkage, therefore, play a major role in energy transduction processes. Redox Bohr effect can also influence the vectorial proton translocation in specific proton pumping mechanisms in respiratory chain (Papa, 1976), (Papa *et al.*, 1994).

### Theoretical and thermodynamic background of the redox Bohr effect

The standard Nernst equation (derived by W. H. Nernst in 1889) (potentials with respect to the SHE at pH 7.0) for a half cell reaction



The equilibrium redox potential ( $E_h$ ) can be represented as

$$E_h = E_{m_x} - \frac{RT}{nF} \ln \frac{a_{\text{red}}}{a_{\text{ox}}} \dots\dots\dots(3)$$

Where,  $E_{m_x}$  is the midpoint potential of the redox reaction with x as the ambient pH value, R is the universal gas constant ( $8.314 \text{ J}^{-1} \text{ K}^{-1} \text{ mol}^{-1}$ ), T is the absolute temperature ( $T_K = 273.15 + T^{\circ}\text{C}$ ), n is the number of electron transferred in the half cell reaction, F is the Faraday constant (columbic charge per mole of electron) ( $9.64853 \times 10^4 \text{ Cmol}^{-1}$ ),  $a_{\text{red}}$  and  $a_{\text{ox}}$  are the activities of the reduced and oxidized species respectively.

For a single electron (n=1) redox-coupled reaction where both acidic and basic form exist for a particular chemical species, the two half cell reaction can be represented in a combined way (Dutton, 1978). For a single protonation reaction, which also involves a single electron change (n=1),

$\text{red H} = \text{ox} + e^{-} + \text{H}^{+}$  under standard condition ( $T = 298.15\text{K}$ ) yields equation (4) as

$$E_h = E_{m0} - 0.06 \log \frac{[\text{red H}]}{[\text{ox}]} - 0.06 \text{ pH} \dots\dots\dots(4)$$

Equation (4) represents a linear pH dependence of  $E_{m0}$  being valid within an ambient pH range. For a broader range of pH, the release and uptake of proton and electron can be schematically represented as depicted in Figure 8. The scheme reflects the basis of the mechanistic aspect of the redox Bohr effect (Papa *et al.*, 1998).

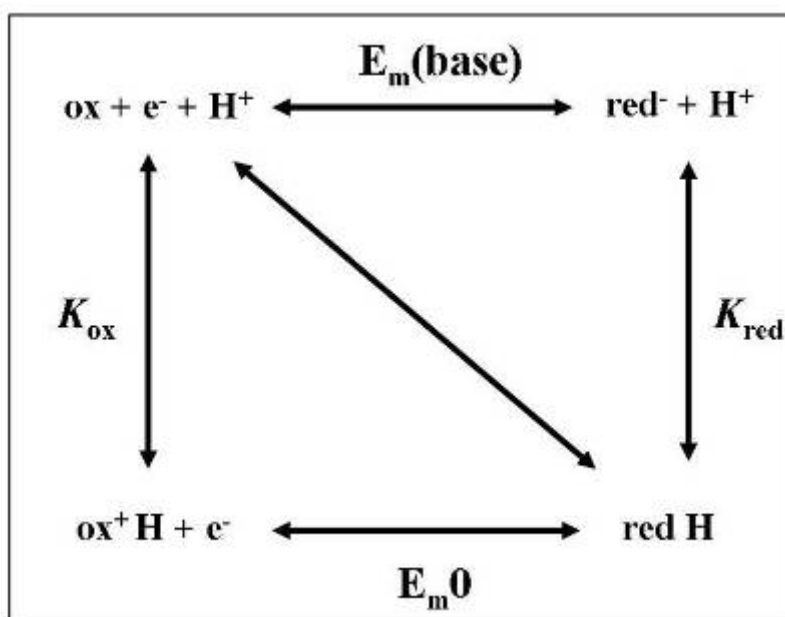


**Figure 8** Graphical scheme of the redox Bohr effect mechanism (figure adapted and modified from Louro *et al.*, 1996). Proton exchange reactions in either the fully reduced or fully oxidized state are indicated by vertical arrows. Pure redox reactions of the protonated or deprotonated species are indicated by horizontal arrows. The diagonal line indicates the coupled reaction.

$K_{\text{red}}$  and  $K_{\text{ox}}$  are the dissociation constants for the deprotonation of the fully reduced species and deprotonation of fully oxidized species, respectively.

$$K_{\text{red}} = \frac{[\text{red}^-][\text{H}^+]}{[\text{red H}]} \dots\dots\dots(5a)$$

$$K_{\text{ox}} = \frac{[\text{ox}][\text{H}^+]}{[\text{ox}^+ \text{H}]} \dots\dots\dots(5b)$$

Considering the total oxidized species and the total reduced species, the entire redox reaction (2) can be represented as:

$$E_{\text{h}} = E_{\text{m}0} - 0.06 \log \frac{[\text{red}^-] + [\text{red H}]}{[\text{ox}] + [\text{ox}^+ \text{H}]} \dots\dots\dots(6)$$

In equation (6), replacing the  $[\text{red H}]$  and  $[\text{ox}^+ \text{H}]$  from equations (5a) and (5b) respectively, we obtain:

$$E_{\text{h}} = E_{\text{m}0} + 0.06 \log \frac{(K_{\text{red}} + [\text{H}^+])}{(K_{\text{ox}} + [\text{H}^+])} \dots\dots\dots(7)$$

This final equation (5) can be schematically represented as:



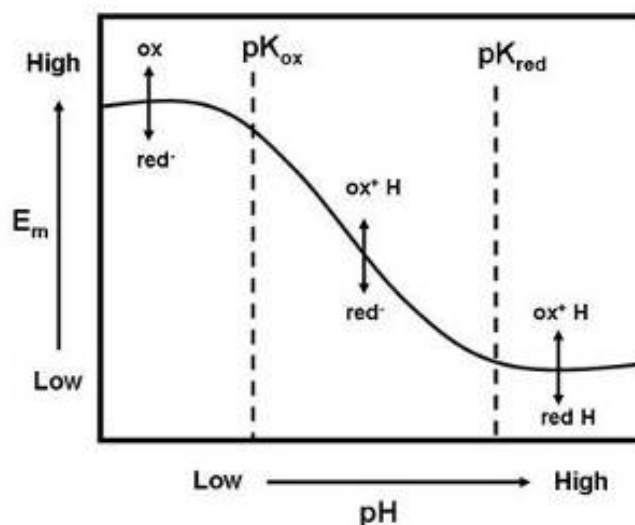


**Figure 9** The pH dependence for the redox potential of centres participating in the redox Bohr effect (figure adapted and modified from Louro *et al.*, 1996).

## 1.4 Static and Time-resolved Approaches Towards a Detailed Investigation of Coupled Electron and Proton Transfer in QFR

Only a limited number of existing biophysical techniques can be employed to investigate the details of the substrate-protein interactions (Breton and Navedryk, 1996), (Breton *et al.*, 1996), (Brudler *et al.*, 1995). Although limited by its resolution, X-ray crystallography (Deisenhofer and Michel, 1989), (Ermler *et al.*, 1994), (Lancaster *et al.*, 1995) provides the most crucial information on the general geometry of the binding site and on the identity of the involved amino-acid residues. Techniques like EPR and solid-state NMR can be utilized though they are also limited for detecting a single redox state of the system. Minute changes in both the oxidized and reduced states of a redox protein system can be selectively and sensitively monitored by Fourier Transformed Infrared (FTIR) difference spectroscopy. Rapid scan FTIR difference spectroscopy is a suitable technique that allows the course of the reaction to be monitored in a time dependent fashion (Barth *et al.*, 1995), (Barth *et al.*, 1996).

### 1.4.1 Static approaches

In the case of *W. succinogenes* QFR, the circumstances for investigating redox Bohr effects are favourable since the amino acid sequence (Körtner *et al.*, 1990), (Lauterbach

*et al.*, 1990) as well as the crystal structure of the enzyme is known (Lancaster *et al.*, 1999). Furthermore, a mutagenesis system for *W. succinogenes* QFR is established (Simon *et al.*, 1998) that allows investigating specific enzyme variants. One of the general consequences of the redox Bohr effects in cytochromes is the pH dependence of the heme midpoint potentials (Wilson and Leigh, 1972). In this present study, the (de)protonation event with respect to the heme redox transition in the *W. succinogenes* QFR wild-type enzyme and variant E180Q were investigated with the help of electrochemically induced FTIR spectroscopy.

Although considerable efforts have been devoted and significant details are already known regarding the catalytic mechanism and enzymatic function of QFR, only little is known to date about the low infrared contribution of the heme porphyrin modes and the heme-ligating groups. Heme porphyrin ring vibration and involvement of heme ligating groups have been previously well studied (Boucher and Katz, 2002), (Dörr *et al.*, 2006), (Dörr *et al.*, 2008) and hence, are expected to contribute in this spectral region of interest (Berthomieu *et al.*, 2006), (Marboutin *et al.*, 2006), (Marboutin *et al.*, 2009), (Xerri *et al.*, 2009). Therefore, in another approach employing static FTIR technique, we used static electrochemically induced FTIR difference spectroscopy to unveil the redox- and pH-dependent properties of heme porphyrins and heme ligands with individual contributions from both heme groups, namely the proximal heme  $b_H$  and the distal heme  $b_L$ . Individual contributions from the low- and the high- potential heme give rise to different signals in the low infrared range. The role of axially ligated histidine ligands can also be investigated by changes in their FTIR signal with pH variation within a certain physiological pH (or pD depending upon solvent/buffer used) range of QFR. In the case of heme-containing redox proteins, electron-coupled proton transfer reactions are frequently mediated by changes in the hydrogen bonding pattern of heme-ligated histidines (Costa *et al.*, 1992), (Haas *et al.*, 2005), (Lancaster *et al.*, 2005).

#### 1.4.2 Time-resolved approaches

Possible involvement of specific amino acid residues and cofactors in this electron-coupled proton transfer pathway has been reported in previous studies (Lancaster *et al.*, 2005), (Haas *et al.*, 2005). Earlier studies of Unden *et al.* (1984) on QFR demonstrated that the kinetic response of the redox cofactors to the addition of 2,3-dimethyl-1,4-

naphthoquinol is consistent with the results obtained from the reconstitution experiments (Lancaster *et al.*, 2000). Therefore, the necessary components of the electron transport chain are kinetically competent as members of the catalytic process. A special interest underlied in the question of possible structural and redox-related changes upon substrate binding that might be involved in the control of such a transiently established proton transfer pathway. This interest in understanding the underlying catalytic reaction mechanism of QFR led to explore the possibility of using photo-releasable substrate to probe the reaction chemistry of the enzyme (Gerwert, 1993), (Lübben and Gerwert, 1996). One of the advantages of using caged compounds in FTIR difference spectroscopy is that this method can simultaneously provide information on the redox and/or protonation state of the cofactor involved and subsequent details on the protein response (Mezzetti *et al.*, 2003).

For studying rapid reactions, the conventional techniques are limited in time resolution to resolve the underlying mechanisms. Therefore, in order to probe dynamics of ultrafast molecular events, short pulses are essential for initial perturbation (Barth *et al.*, 1995), (Barth *et al.*, 1996). Based on the fact that the two heme groups in QFR have different redox potentials, chemical reduction can generate a mixed-valence state in QFR. Upon excitation by a short laser flash on such a semi-reduced state of QFR, electrons on the reduced high potential heme can be selectively excited and thereby the decay of the transient absorption can be monitored.

The planar heme prosthetic group (Fe-Protoporphyrin) gives this class of proteins their rich and interesting spectroscopic properties. The absorbance of the hemes is due to redox induced charge transfer between the electronic systems of the central iron and the porphyrin ring or the ligands ligated to the hemes (Franzen and Boxer, 1997). For the hemes, a ground state,  $S_0$ , and three excited states,  $S_1$  to  $S_3$ , are considered; and the corresponding transitions are of the type  $\pi$ - $\pi^*$  (Guest and Noe, 1988), (Franzen and Boxer, 1997). The two dominant contributions in the spectra are caused by  $S_0 \rightarrow S_1$  ( $\alpha$ -band) and  $S_0 \rightarrow S_3$  (Soret-band) transitions. Thus, the strong  $\pi$  to  $\pi^*$  electronic excitation of the porphyrin ring around 400 nm is commonly known as Soret band (or gamma band) in cytochromes. This band couples the nuclear motion of the heme and its axial ligands. This coupling leads to spectral broadening of the optical transition and a strong Raman signal (Shelnutt, 1981). The Soret band in *W. succinogenes* QFR is

positioned at 415 nm in the oxidised state of the heme and at 428 nm in the reduced state of the heme. Changes in the overlap between the  $d_{yz}$ ,  $d_{xz}$  (or  $d_{\pi}$ ) orbitals of the iron with the  $e_g \pi^*$  orbitals of the porphyrin affect the absorption energy and are hence responsible for the Soret band bathochromic shift in different heme redox states (Franzen and Boxer, 1997), (Franzen *et al.*, 2002).

## 1.5 Relevance and usefulness of the employed methods

In the so-called mid-infrared region ( $2300\text{-}1000\text{ cm}^{-1}$ ), reaction-induced FTIR difference spectroscopy is a very powerful and highly sensitive technique to extract information about subtle changes occurring within the active sites of the protein (Mäntele, 1993). A variation in the redox state of active centres in proteins can bring about structural changes. Electrochemically-induced FTIR difference spectroscopy is a useful method to study these conformational reorganisations of the protein backbone, side chains, cofactors and subsequent protonation/deprotonation events (Haas *et al.*, 2005), (Hellwig *et al.*, 1996), (Hellwig *et al.*, 1998), (Mäntele, 1993), (Mileni *et al.*, 2005). In order to investigate the pH dependence of the amino acid residue Glu C180 in the framework of redox Bohr effect, electrochemically induced FTIR difference spectroscopy has been performed in the mid-infrared region from  $1800$  to  $1000\text{ cm}^{-1}$ . The protonation/deprotonation state and the change of the hydrogen-bonding environment of Glu C180 has been previously investigated (Haas *et al.*, 2005) with respect to the heme redox transition. In the present study, spectra of WT QFR and QFR E 180Q variant have been recorded between pH 5.5 and pH 9.0 showing a strong pH dependency of the protonated carboxylic acid band assigned to Glu C180 around  $1740\text{ cm}^{-1}$  indicating protonation changes of the involved carboxylic acid group therein. The observed differences between WT and E180Q are discussed with respect to the mechanism of the proposed “E-pathway hypothesis”.

Various methods have been developed which can be applied to calculate  $pK_a$ s of residues in proteins. The biophysics simulation program MultiConformation Continuum Electrostatics (MCCE) combines the molecular mechanics and the continuum electrostatics (Alexov and Gunner, 1997), (Beroza and Case, 1996), (Gunner and Alexov, 2000), (Spasov *et al.*, 2001), (You and Bashford, 1995). These methods keep the protein dielectric constant low and allow the consideration of multiple positions of

side chains. Analysis of the results provides a picture of different residues throughout the protein that change their position or charge and occupancy upon simulated pH and/or  $E_h$  titration. In the present context; MCCE, calculations have been performed in order to obtain Glu C180 residue occupancy with four different modeled redox states of the distal and proximal heme groups with respect to the variation in pH range from 5 to 9. It has been shown that the experimentally obtained results perfectly correlate with theoretical electrostatic calculations (Haas and Lancaster, 2004) of simulated heme reduction and are relevant for the understanding of the catalytic mechanism of QFR.

In the case of redox-active proteins, studying metal-ligand vibrations is crucial to obtain important information about the metal-ligand bond strength and its role in specific redox-linked mechanisms. Vibrational spectroscopy can be applied to probe specific chemical groups involved in metal binding and the characteristics of metal-ligand interactions. Vibrational transitions are independent of the metal's magnetism and redox state and hence describe the electronic properties of a particular amino acid ligated to a specific metal (Gourion-Arsiquaud *et al.*, 2005). Metal–ligand vibrations of single bonds contribute to the spectrum in the low- and far- infrared range ( $1000 - 50 \text{ cm}^{-1}$ ). FTIR measurement in the low-frequency (“low-frequency” region of IR spectrum is generally referred to  $<1000 \text{ cm}^{-1}$ ) spectral range is often limited by the extensive absorption of water modes (Chu *et al.*, 1999), (Dörr *et al.*, 2006), (Wolpert and Hellwig, 2006). The use of  $\text{D}_2\text{O}$  (Goulden, 1959), small sample layer thickness (Fabian and Mäntele, 2002) and sufficiently concentrated protein samples can solve this problem to a significant extent. Reliable low-frequency FTIR difference spectra can be obtained with a precise temperature control of  $\pm 0.1^\circ\text{C}$ .

Time-resolved FTIR (tr-FTIR) spectroscopy is a useful and established tool to analyse the changes in secondary structural population (or conformational changes) in protein's substrate binding domain with the ligand binding process (Barth and Zscherp, 2000). Mechanism of photochemical release of fumarate from the caged fumarate was studied. Vibrational difference spectra for the formation first of the *aci*-nitro anion intermediate and subsequent structural and functional reorganisations were traced in the millisecond to second time domain. Spectral characteristics of the reaction products arising from the caging group have been determined. Although the entire reaction kinetics was completed within approximately 200 ms after the flashing, it was possible

to obtain difference spectra between the cage only and the released cage with QFR in solution (in phosphate buffer, pH 7.4) in the presence of glutathione. For the assignment kinetic data were compared to the equilibrium measurements of fumarate binding to QFR reflected in attenuated total reflection (ATR) FTIR experiments and its correlation with the possible structural changes. This allows identification of the transient intermediates upon substrate binding.

In another time-resolved approach to investigate the inter-heme electron transfer in QFR, VIS difference spectra were obtained by separately applying chemical reducing agent such as dithionite and/or DMNH<sub>2</sub> (2, 3-dimethyl-1, 4-naphthoquinol). DMNH<sub>2</sub> reduction was particularly carried out in order to make specific reduction of only the high potential heme. As the DMN/DMNH<sub>2</sub> redox couple has midpoint potential of -75 mV (Madej *et al.*, 2006a) which is only able to reduced the high potential heme specifically, it is therefore suitable for kinetic studies to create such a state where the high potential heme only will be occupied with electron and thereby the measurement of electron transfer from the high potential heme to the low potential heme would be feasible. A single-beam spectrum was measured and taken as a reference for subsequent potential steps that covered the heme potential range between fully reduced and fully oxidized.

## 2 Materials and methods

### 2.1 Materials

#### 2.1.1 List of mediators

One of the rate-limiting factors in protein electrochemistry is the diffusion of the protein to the working electrode. Addition of small redox-active substances (so called “redox mediators”) can considerably shorten the diffusion time (Baymann *et al.*, 1991), (Baymann *et al.*, 1999), (Dutton, 1978) of the large protein complexes and therefore fasten the electron exchange rate between the protein and electrode surface. This electrical contact is important in case of large and slowly-diffusing proteins containing redox-active groups (cofactors) which are deeply lying and hidden within the protein’s core. Effective electron transmission is ensured by matching the range of the redox midpoint potential of the cofactors and that of the used mediator’s composition. Since QFR contains several cofactors with different redox midpoint potential values (Mileni *et al.*, 2006), the mediator composition was designed accordingly with substances (Haas *et al.*, 2005), (Hellwig *et al.*, 1998), (Hellwig *et al.*, 2000) which covered the entire potential range under examination. Table 2 shows the actual list of mediators used for electrochemical measurements.

**Table 2** List of mediators for electrochemical measurements.

Mediator	MW (g/mol)	$E_m$ (mV) vs. Ag/AgCl	Solvent	Company
tetrachlorobenzoquinone	245.9	72	diethyl ether	Aldrich
2,6-dichlorophenolindophenol	290.1	9	ethanol	Sigma
ruthenium hexaminchloride	274.2	-8	water	Aldrich
anthraquinone-2,6-disulphonate	368.0	-23	water	Fluka
1,2-naphtoquinone	158.2	-63	ethanol	Aldrich
anthraquinone	207.1	-108	ethanol	Fluka
trimethylhydroquinone	152.2	-108	ethanol	Aldrich
5-hydroxy-1,4-naphtoquinone	174.2	-158	ethanol	Fluka
duroquinone	164.2	-198	ethanol	Fluka
menadione	172.2	-220	acetone	Sigma
2-hydroxy-1,4-naphtoquinone	174.2	-333	ethanol	Aldrich
anthraquinone-2-sulphonate	328.3	-433	ethanol	Aldrich
neutral red	288.8	-515	ethanol	Sigma
benzyl viologen	409.4	-568	water	Sigma

methyl viologen	257.2	-628	water	Sigma
-----------------	-------	------	-------	-------

### 2.1.2 List of chemicals

**Table 3** List of chemicals.

Substance	Company	Website
Mercaptopropionic acid	Fluka, Switzerland	<a href="http://www.sigmaaldrich.com">www.sigmaaldrich.com</a>
K <sub>2</sub> HPO <sub>4</sub> and KH <sub>2</sub> PO <sub>4</sub>	Carl Roth GmbH & Co., Germany	<a href="http://www.carlroth.com">www.carlroth.com</a>
KCl	Merck, Darmstadt, Germany	<a href="http://www.merck.de">www.merck.de</a>
n-dodecyl-β-D-maltoside (LM)	Glycon Biochemicals, Germany	<a href="http://www.glycon.de">www.glycon.de</a>
Sodium borate	Merck, Germany	<a href="http://www.merck.de">www.merck.de</a>
Cacodylic acid - sodium salt, 3 H <sub>2</sub> O	Fluka, Switzerland	<a href="http://www.sigmaaldrich.com">www.sigmaaldrich.com</a>
Hydrochloric acid	Merck, Germany	<a href="http://www.merck.de">www.merck.de</a>
D <sub>2</sub> O (99.9% purity)	Deutero GmbH, Germany	<a href="http://www.deutero.de">www.deutero.de</a>
EDTA	GERBU, Germany	<a href="http://www.gerbu.de">www.gerbu.de</a>
L-Glutathione	Fluka, Switzerland	<a href="http://www.sigmaaldrich.com">www.sigmaaldrich.com</a>
DTT	Merck, Germany	<a href="http://www.merck.de">www.merck.de</a>
Tris	Carl Roth GmbH & Co., Germany	<a href="http://www.carlroth.com">www.carlroth.com</a>
Morpholinoethanesulfonic acid (MES)	Carl Roth GmbH & Co., Germany	<a href="http://www.carlroth.com">www.carlroth.com</a>
CHES	Merck, Germany	<a href="http://www.merck.de">www.merck.de</a>
Mono-ethyl fumarate	Fluka, Switzerland	<a href="http://www.sigmaaldrich.com">www.sigmaaldrich.com</a>

### 2.1.3 List of laboratory equipment

**Table 4** List of laboratory equipment

Device	Company
Modified IFS 25 FTIR spectrometer (Including UV/VIS spectrometer as provided by Institute of Biophysics, JWGU)	Bruker Optics, Ettlingen, Germany
Modified IFS 66 FTIR spectrometer	Bruker Optics, Ettlingen, Germany
Potentiostat (designed and constructed in JWGU)	as provided by Institute of Biophysics, JWGU
Spectroelectrochemical cell	as provided by Institute of Biophysics, JWGU
Potentiostat chi600C	IJ Cambria Scientific Ltd, Carms UK
Spectroelectrochemical cell type 1	IJ Cambria Scientific Ltd, Carms UK
Spectroelectrochemical cell type 2	IJ Cambria Scientific Ltd, Carms UK
Gold mesh (for working electrode)	Buckbee-Mears, St. Paul, USA
Table centrifuge "4 K 10"	Sigma, Steinheim, Germany
Table centrifuge "Labofuge 200"	Heraeus, Hanau, Germany
Table centrifuge "5415C"	Eppendorf, Hamburg, Germany
Precision balances	Sartorius, Göttingen, Germany



---

Centrisart I filtration tubes	Sartorius, Göttingen, Germany
Vivaspin 500 $\mu$ L concentrators	Vivascience, Hannover, Germany
pH meter	SevenEasy Mettler Toledo (for buffer), Roth
FTIR (IFS 66) CaF <sub>2</sub> windows	Innovectis GmbH, Frankfurt Main, Germany
FTIR (IFS 66) sample holders	as provided by Institute of Biophysics, JWGU
AtmosBag <sup>TM</sup> (AL-211)	Sigma-Aldrich Co., Milwaukee, USA
ZnSe windows	Thorlabs, Munich, Germany
Double-beam spectrophotometer	U3000, Hitachi, Japan
XeCl excimer laser (RD-EXC-200)	Radiant Dyes Laser Accessories GmbH, Wermelskirchen, Germany.
fs laser system	CLARK CPA 2001 (Dexter, MI, USA)

---

## 2.2 Infrared Spectroscopy

### 2.2.1 Vibrational and vibrational-rotational (infrared) spectroscopy

These spectra originate from transitions induced between the vibrational energy levels of a molecule on the absorption of radiation belonging to the infrared (IR) region (Phan, 2009). IR spectra are shown by molecules when vibrational motion is accompanied by a change in dipole moment of the molecule. An infrared spectrum represents a fingerprint of a sample with absorption peaks which correspond to the frequencies of vibrations between the bonds of the atoms making up the molecule (Fabian and Mäntele, 2002). Because each different material is a unique combination of atoms, no two compounds produce the exact same infrared spectrum. Therefore, infrared spectroscopy can result in a positive identification (qualitative analysis) of every different kind of material. In addition, the size of the peaks in the spectrum is a direct indication of the amount of material present. With modern software algorithms, infrared is an excellent tool for quantitative analysis (Rahmelow *et al.*, 1998).

### 2.2.2 The Michelson interferometer

The main component in the FTIR spectrometer is a Michelson interferometer (Griffiths, 1986), (Moss *et al.*, 1990). This device splits and recombines a beam of light such that the recombined beam produces a wavelength-dependent interference pattern or an interferogram.

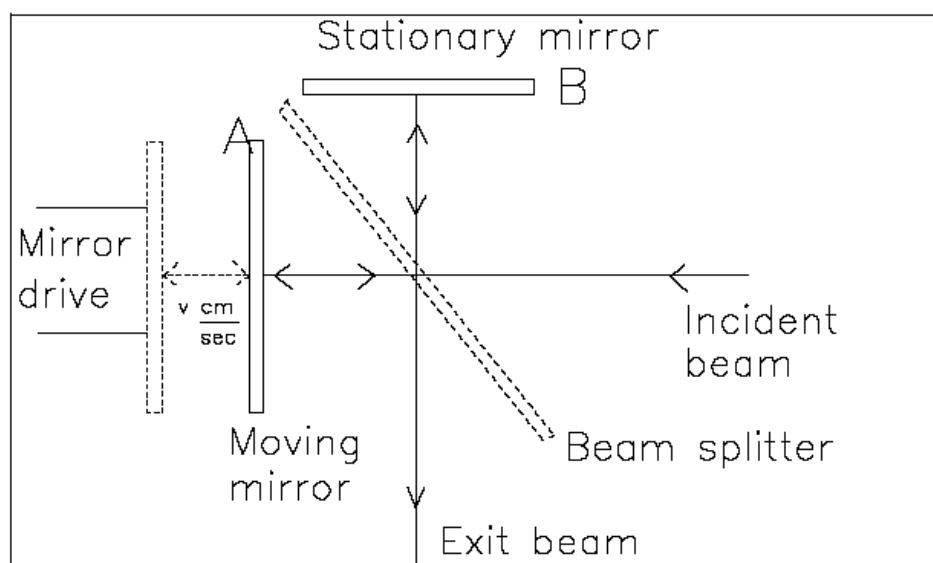


**Figure 10** Optical schematic of a Michelson interferometer. (Adapted from “Fundamental Infrared Spectroscopy” by Hue Phan) (Phan, 2009)

A typical Michelson interferometer consists of two mirrors and a beamsplitter positioned at an angle of 45 degrees to the mirrors. A KBr beamsplitter coated with Germanium is used for mid IR region. Incident light strikes the beamsplitter so that half of the light is transmitted through the beamsplitter and half is reflected to the mirrors. The two components are then reflected back and recombined at the beamsplitter with half of the light passing on toward the sampling areas and half travelling back toward the source. The signal at the detector is a cosine wave.

The interference signal measured by the detector as a function of the optical path length difference is called the interferogram. An interferogram shows the intensity of the infrared radiation as a function of the displacement of the moving mirror. At the peak position, the optical path length is exactly the same for the radiation that comes from the moving mirror as it is for the radiation that comes from the fixed mirror. The interferogram contains the basic information on frequencies and intensities characteristic of a spectrum but in a form that is not directly interpretable. Thus, the information is converted to a more familiar form, a spectrum, using Fourier Transform methods. A spectrum is calculated from the interferogram by computing the cosine Fourier transform of the interferogram.

### 2.2.3 Fourier transformation

Interferogram measured by an interferometer is the sum of the interferograms of all the constituent frequencies present in the source. The Fourier transformation, then, breaks down the interferogram to reveal these constituent frequencies telling us which are present, and in what amount. The interferogram belongs in the length (e.g. cm) domain. Fourier transformation (FT) is a well-known computer-aided mathematical technique that inverts the dimension, so the FT of the interferogram belongs in the reciprocal length domain, which is the wavenumber ( $\text{cm}^{-1}$ ) domain. The spectral resolution in wavenumbers per cm is equal to the reciprocal of the maximum retardation in cm.

### 2.2.4 Fourier transform infrared spectroscopy

FTIR spectroscopy is preferred over conventional dispersive infrared spectroscopy for several reasons. It is an essentially non-destructive technique which provides a precise measurement method without any external calibration. Furthermore, it can increase speed and sensitivity having a greater optical throughput. The interferometer device can overcome the slow scanning speed by measuring all the infrared frequencies simultaneously rather than individually. The interferometer produces a unique type of signal which has all of the infrared frequencies “encoded” into it. Every data point (a function of the moving mirror position) in an interferogram has information about every infrared frequency which comes from the source. There are three significant practical advantages of FTIR over the dispersive technique which renders the FTIR method accurate and reproducible: **(1)** Multiplex (or Fellgett) Advantage: Because all of the frequencies are measured simultaneously, most measurements by FTIR are made in a matter of seconds rather than several minutes. **(2)** Throughput (or Jacquinot) Advantage: Sensitivity is dramatically improved with FTIR for many reasons. The detectors employed are much more sensitive, the optical throughput is much higher which results in much lower noise levels, and the fast scans enable the coaddition of several scans in order to reduce the random measurement noise to any desired level (referred to as signal averaging). **(3)** Internally Calibration (or Connes) Advantage: Instruments generally employ a HeNe laser as an internal wavelength calibration standard. These instruments are self-calibrating and never need to be calibrated by the user (Herres and Gronholz, 1985).

The sensitive identification has made FTIR an invaluable tool for quality control applications. In addition, the sensitivity and accuracy of FTIR detectors have dramatically increased the practical use of infrared for quantitative analysis.

### 2.3 Electrochemistry

Classical electrochemistry can be applied for investigating redox-active proteins. However suitable conditions and adaptations of the electrochemical techniques are required. The redox state of an entire protein or a specific cofactor can be triggered by imposing a certain redox potential value (Moss *et al.*, 1990), (Mäntele, 1996). Afterwards the redox induced changes within the protein can be monitored by suitable spectroscopic means. The electrolyte solution basically contains freely moving ions where the two electrodes system constitutes a “half-cell”. Depending on the applied voltage, in the boundary surface between electrode and solution, a half-cell potential arises and therefore electrons tend to flow along their gradient resulting in a reduction or oxidation reaction.

The Nernst equation describes the correlation between the redox potential of the half-cell and the activity of the oxidised/reduced species at a certain temperature. The redox potential of a half-cell can be determined only when it is compared with a second half-cell. The potential of the second cell can be set to zero (reference electrode) e.g. standard hydrogen electrode (SHE). Since the NHE works corrosively and explosively, it is hardly used in practice. Instead reference electrodes are used like the Ag/AgCl or the calomel electrode. One can get the actual potential by adding the reference potential to the measured potential value. One of the major advantages of this technique is to monitor the redox potential to some intermediate conditions or any desired value, the other being the reversibility of the reaction. The measurement can be hampered by the high flow of current resulting in Ohm's voltage drop in the cell. Introduction of a third electrode called counter electrode, can solve this problem by constituting a three-electrode array.

### 2.3.1 The electrochemical cell

All electrochemically induced FTIR and UV/VIS difference spectra presented in this work were collected using the ultra-thin-layer spectroelectrochemical cell (Mäntele, 1993), (Moss *et al.*, 1990) shown in Figure 11.

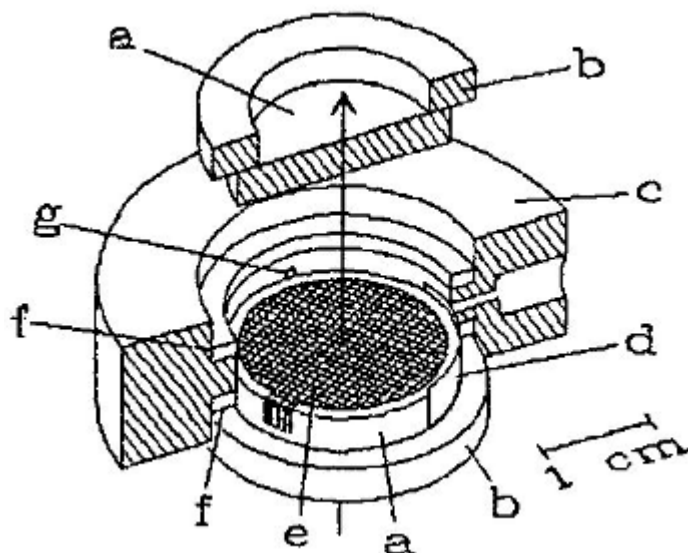


**Figure 11** A schematic view of the spectroelectrochemical cell: a: CaF<sub>2</sub>-window, b: Plexiglass ring, c: PVC body, d: Platinum counter electrode, e: Gold grid working electrode, f: Rubber O ring, g: Inlet for the Ag/AgCl reference electrode. The figure was taken from ref. (Moss *et al.*, 1990).

The cell consists of a PVC body with four openings. In the cell the three-electrode array is described. The cell is completely assembled with the two CaF<sub>2</sub>-windows after filling with sample. 7-8  $\mu\text{L}$  of the prepared protein solution is applied on the window, which is then fit in such a way into the cell that a thin sample film is formed. This must be nonporous and cover the entire window area. The gold grid working electrode (E) has a mesh size of  $30 \times 30 \mu\text{m}$  with about 50% optical transparency. Afterwards the cell is fixed between two screwable metal plates. Depending on the strength of pressing the plates, a sample layer thickness of the film on 5-10  $\mu\text{m}$  can be adjusted. The arrow in the Figure 11 shows the direction of the optical radiation. The water absorption within the sample layer is thus optimised to a value under 1 OD so that the detector can produce a sufficiently large signal. In order to establish the contact between the electrodes and the protein solution, the cell compartment is filled up by with buffer. Finally the reference electrode, connected with the inside of the cell by a salt bridge, is screwed in.

### 2.3.2 Surface modification of the gold grid working electrode

Full reversibility of the electrode reaction is ensured only if a direct contact of the protein with the electrode surface can be avoided. Proteins with redox-active groups "poison" the electrodes by adsorbing at the metal surface and thereby denaturing irreversibly. A reversible electrode reaction is then no more ensured. In order to avoid this direct contact of the protein with the electrode surface, a protective layer of surface-modifying substances are used, which can set a contact with the protein with the metal surface and this contact can be received at the same time. They are called "surface modifier" (or "activators") (Veiseha *et al.*, 2007) and must be specified accordingly with respect to the protein under examination, the rate of the reaction and accessibility upon right orientation of the electrode surface. Usually the mediator substances contain two different functional groups, of which one is in contact with the metal surface and another one interacts with the protein. A solution of 2 mM mercapto propionic acid (Gries *et al.*, 1997) in ethanol was used and afterwards a monolayer of the surface modifier was created using an ultrasonic bath for 20 minutes.

### 2.3.3 Redox mediators

With increasing size of the protein, the charge transfer between electrode and protein runs more slowly. Often the redox-active cofactors lie buried within the protein core and thus badly attainable. Both the problems can be solved by the using redox mediators. These are small, redox-active molecules which can diffuse in contact zones making fast electron transfer possible to the cofactors. Generally one uses several mediators in a solution mixture (see chapter 2.1.1). The mixture of fifteen different redox mediator substances is listed in Table 2 (also see (Haas *et al.*, 2005)).

### 2.3.4 Electrochemically induced FTIR spectroscopy of QFR

#### 2.3.4.1 Sample preparation

Cells of *W. succinogenes* wild-type enzyme were grown and the QFR enzyme purified by Nicole Hilgendorff according to a protocol described previously (Lancaster *et al.*, 1999). The protein solution was washed with the corresponding buffer in a centrifuge filtration tube (Sartorius, Göttingen, Germany) of 100 kDa cutoff mass with 4 washing cycles of 20 min each. The final sample volume was adjusted in Vivaspin 500  $\mu$ L

concentrators (Vivascience, Hannover, Germany) (Haas *et al.*, 2005). Buffer solutions were prepared at a concentration of 50 mM in H<sub>2</sub>O (or D<sub>2</sub>O) with 100 mM KCl and 0.03% LM detergent present in it. 7-8  $\mu$ L of 0.6 mM protein solution was sufficient to fill the spectroelectrochemical cell. For measurements with pH values 5.6, and 7.4, MES (Morpholinoethanesulfonic acid) and Tris-HCl buffers were used, respectively. For pH 8.5, CHES (2-(Cyclohexylamino)-ethanesulphonic acid) buffer was used. For high and low pH buffer preparations the pH was finally adjusted by adding DCl or NaOD solution, respectively.

#### 2.3.4.2 Spectroelectrochemistry

For the estimation of the layer thickness of the protein solution before each measurement, an IR absorption spectrum was recorded where the empty sample chamber served as reference. It was essential to maintain the the optical path length of the spectroelectrochemical cell as a thin layer (an order of 10  $\mu$ m) for fast equilibration in the cell. The sample could be fully oxidized or reduced, depending on the applied electrode potential. The miniature Ag/AgCl/3M KCl reference electrode was inserted in one side of the cell, close to the working electrode. The electrical contact was ensured by the buffer solution filled from the other side. First, a potential was applied to the sample. In the present work the potential range was examined from -0.6 to +0.3 V with respect to the SHE. Within the range of 2000 to 1000  $\text{cm}^{-1}$ , 128 interferograms with spectral of 4  $\text{cm}^{-1}$  were acquired. After a certain time when a redox equilibration was established, a second potential is applied and then a second spectrum was taken. Now from both the spectra the actual difference spectrum was computed. In order to achieve a good signal-to-noise ratio, 15-20 difference spectra were averaged.

For the low-frequency IR experiments, FTIR redox difference spectra in the range from 2000-500  $\text{cm}^{-1}$  were collected using a modified Bruker setup (IFS 25 and IFS 28). A KBr beam splitter and a DTGS detector were used. The spectra were obtained by averaging 2 times 256 scans at a spectral resolution of 4  $\text{cm}^{-1}$ . FTIR difference spectra were calculated from the two different single beam spectra with the initial single beam spectrum taken as reference. For a single experiment, 50-100 (ideally 80) difference spectra have been averaged. The spectrum of the early cycle and those of the late cycles were very similar indicating no significant change in spectral

pattern during the course of several redox cycles. The ultra-thin spectroelectrochemical cell (Moss *et al.*, 1990) for the visible and IR was adapted to a lower spectral range. For this purpose the infrared windows were changed to ZnSe and the pathlength was reduced to 5-6  $\mu\text{m}$  (Wolpert *et al.*, 2004). To avoid denaturation of protein, prior to the measurement, the gold grid working electrode was chemically modified by a mixture of 2 mM solution of mercaptopropionic acid and cysteamine in 1:1 ratio (see chapter 2.3.2). Redox mediators were used at a final concentration of 35  $\mu\text{M}$ , thereby shortening the time required for equilibration (Haas *et al.*, 2005), (Hellwig *et al.*, 1998). Control measurements showed that there were no spectral contributions from the mediators at identical experimental conditions. Approximately 7  $\mu\text{L}$  protein solution was sufficient to fill the spectroelectrochemical cell. The equilibration generally took 7-8 minutes for the full potential step from -0.37 V to +0.21 V with respect to the SHE at pH 7.0. For obtaining FTIR difference spectra due to individual single heme redox transitions, an intermediate potential value was used (Mileni *et al.*, 2005). The spectrometer was equipped with a thermostated water bath for experiments at a fixed temperature of 5  $^{\circ}\text{C}$ . Spectroscopic data processing and analysis were performed by the Bruker OPUS and the ORIGIN program.

## 2.4 Time-resolved FTIR difference spectroscopy

### 2.4.1 Caged substrates

Flash photolysis of photoactivable probes provides a means of controlling the release, both spatially and temporarily (Marriott, 1998). 2-nitrobenzyl (NB) derivatives are by far the most common photolabile protecting groups. Most of the caged reagents described in the literatures have been derivatives of *ortho*-nitrobenzylic compounds (such as, 2 nitrobenzaldehyde, 2-nitrobenzyl and/or 1-(2-nitrophenyl) ethyl acetate/phosphate/sulphate/tosylate) (Bonetti *et al.*, 1997),(Janko and Reichert, 1987),(Viappiani *et al.*, 1998) which are activated by photolysis at <360 nm. Their application in biochemistry was pioneered in the usage of caged-ATP (Kaplan *et al.*, 1978) and later on the work on the release of photolabile chelators for the rapid photorelease of divalent cations (Kaplan and Ellis-Davies, 1988). Photo-fragmentation of the usual NB (2-nitrobenzyl) or NPE (1-(2-nitrophenyl)ethyl) groups with a carboxy substituent on the benzylic carbon (e.g.  $\alpha$ -carboxy- 2-nitrobenzyl (CNB)) has been



widely applied as the most common photochemistry among the available range of photolabile protecting groups for rapid release of biologically-active species at or near their site of action in biological systems (Corrie *et al.*, 2008). The ionized side chain confers improved water solubility and rapid release of the bioactive species upon flash photolysis occurs from corresponding NB or NPE cages. Previous studies of CNB cages make the implicit assumption that the carboxy substituent is an inert bystander that does not participate in the photocleavage reaction (Corrie *et al.*, 2008). In most cases their application is limited by the low efficiency of activation and the generation of reactive *o*-nitrosocarbonyl photoproducts (Barth *et al.*, 1997), (Geißler *et al.*, 2005). In these kinetic studies of QFR, the suitability of caged fumarate is an important issue. This is dependent on the stability of the cage against spontaneous hydrolysis, inactivity of QFR in presence of unphotolysed caged substrate and a non-inhibitory effect on the photoproduct. Synthesis of a novel cage substrate called  $\alpha$ -carboxy-*o*-nitrobenzyl (CNB)-caged fumarate (Paul, R., Bamann C., Enela Džafić, E., Mileni, M., Fendler, K., Mäntele, W., and Lancaster, C.R.D., *in preparation*) is presented here. In case of CNB-caged compounds, since the photolysis process is irreversible, the method consists of controlled illumination and quantification of the photo product. The new caged-compound is characterised with regard to its suitability in studies incorporating QFR. It is shown that the photolysis of the caged fumarate activates indeed the QFR without inhibition by the photoproducts or the unphotolysed caged fumarate.

Complementary to our approach of employing caged fumarate in a similar approach to study the kinetic phenomena, caged menaquinol (2-Methyl-3-methylamino-1,4-naphthoquinone(ol)) was characterized. Caged quinols can release the substrate quinol in solution and can thus trigger the QFR enzymatic reaction. Experiments were performed in the presence of QFR under optimised experimental conditions. The XeCl excimer laser equipped with a Bucker IFS-66 setup was used for the controlled photo-flashing.

#### 2.4.1.1 Synthesis of the caged fumarate

The reaction scheme of the synthesis is illustrated in Figure 12.

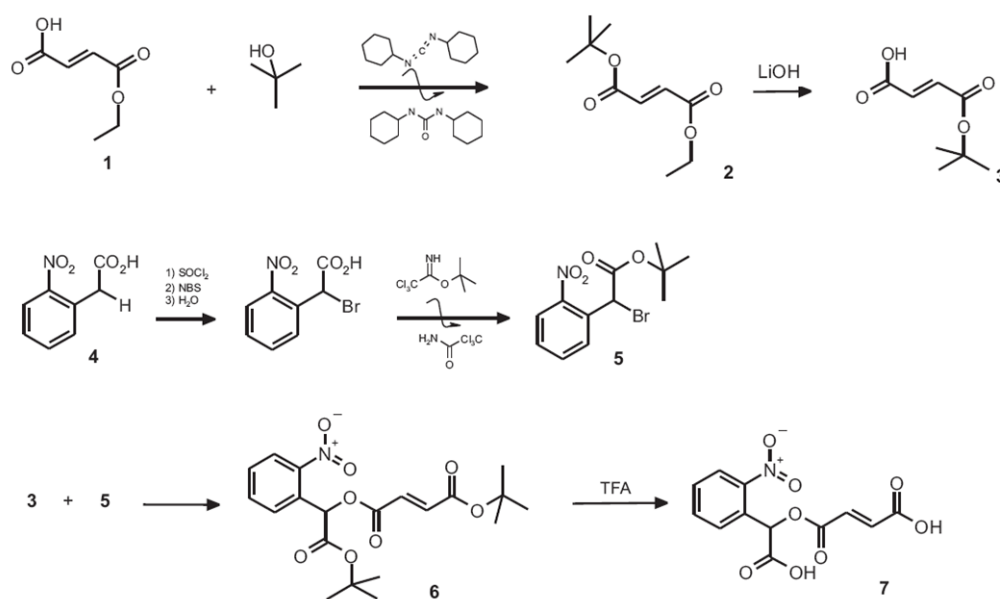


**Figure 12** Reaction scheme for the synthesis of the CNB-fumarate.

Synthesis and initial characterisations of the  $\alpha$ -carboxy- 2-nitrobenzyl (CNB)-caged fumarate were performed by Dr. C. Bamann in the Fendler group (Dept. Biophysical Chemistry, MPIBP, Frankfurt am Main). The reaction sequence starts with the commercially available mono-ethyl fumarate (Fluka) that reacts with t-butanol to the mixed diester of fumarate (60% yield, (Neises and Steglich, 1985)). <sup>1</sup>H-NMR (250 MHz, CD<sub>2</sub>Cl<sub>2</sub>)  $\delta$  6.73 (d, 2H, C<sub>3,4</sub>H); 4.22 (q, 2H, CH<sub>2</sub>); 1.49 (s, 9H, C(CH<sub>3</sub>)<sub>3</sub>); 1.29 (t, 3H, CH<sub>3</sub>). Selective hydrolysis by LiOH (Denmark *et al.*, 1996) leads to t-butyl fumarate (67% yield). <sup>1</sup>H-NMR (250 MHz, DMSO)  $\delta$  6.59 (d, 2H, C<sub>3,4</sub>H); 1.45 (s, 9H, C(CH<sub>3</sub>)<sub>3</sub>). The reaction to the  $\alpha$ -carboxy-*o*-nitrobenzyl (CNB) fumarate (“caged fumarate”) follows a modified two-step procedure from (Gee *et al.*, 2002). Coupling with the activated photolabile group (Bromo-(2-nitro-phenyl)-acetic acid-t-butyl ester, a generous gift from Dr. C. Grewer) provides the product with the t-butyl protecting groups. <sup>1</sup>H-NMR (250 MHz, CD<sub>2</sub>Cl<sub>2</sub>)  $\delta$  8.17 (d, 1H, C<sub>3</sub>H), 7.72-7.53 (m, 3H, ArH); 6.59 (d, 2H, C<sub>9,10</sub>H); 5.83 (s, 1H, CH), 1.50 (s, 9H, C(CH<sub>3</sub>)<sub>3</sub>); 1.39 (s, 9H, C(CH<sub>3</sub>)<sub>3</sub>). The caged fumarate is obtained as an oily compound after hydrolysis of the protecting groups with TFA and separation on a LM-20 sephadex column (45% yield). <sup>1</sup>H-NMR (250 MHz, CD<sub>2</sub>Cl<sub>2</sub>)  $\delta$  8.07 (d, 1H, C<sub>3</sub>H), 7.78-7.52 (m, 3H, ArH), 6.97 (d, 2H, C<sub>3,4</sub>H); 5.32 (s, 1H, CH).

### 2.4.1.2 Synthesis of the caged-MMAN

The 2-step synthesis scheme of the caged-MMAN is shown in Figure 13. The caged-MMAN compound was synthesised and provided by by Dr. H. Nasiri in the Schwalbe group (J. W. G. University, Frankfurt am Main).

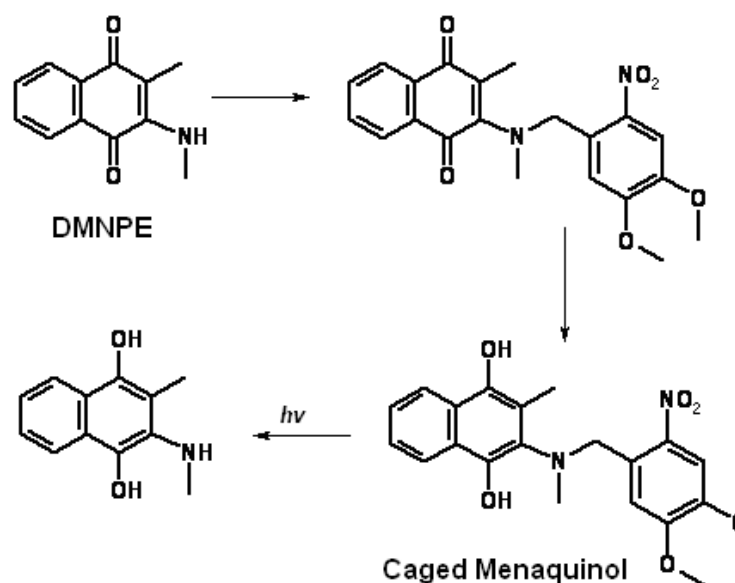


**Figure 13** The two-step reaction required for synthesizing the caged menaquinol from the menaquinone precursor of DMNPE. The first two steps represent the synthesis of the caged substrate and reduction of the quinone to quinol, respectively. The synthesis involves the following conditions: APPH3 (1.1 equiv); DEAD (1.1 equiv); THF, 0°C then room temperature (83%). The final reaction (3<sup>rd</sup>) depicts the release of the substrate upon photolysis.

### 2.4.1.3 Visible spectroscopy and flash-photolysis

UV/VIS spectra were recorded on a double-beam spectrophotometer (U3000, Hitachi, Japan). Flash-photolysis studies were performed on a home-built setup (Bamann *et al.*, 2008). The reaction was started with a 10 ns flash from a XeCl excimer laser (308nm). Absorbance changes were recorded with a Si photodiode with a Xe lamp (75 W) as the perpendicular measuring light. Signals were amplified by a current-voltage converter and further subjected to a low pass filter (1 MHz).

## 2.4.2 Time-resolved FTIR measurements

*W. succinogenes* WT QFR sample preparation for FTIR experiments has been described in detail previously (Haas *et al.*, 2005) Briefly, after concentrating the sample

(in potassium phosphate buffer, pH 7.4) 4-6  $\mu\text{L}$  were put on a  $\text{CaF}_2$  window of a trough of 10  $\mu\text{m}$  depth and 8 mm diameter. The sample was sealed with a second flat  $\text{CaF}_2$  window and was thermostated at 5°C during the whole measurement time. The sample mixing was performed inside an anaerobic AtmosBag<sup>TM</sup> under continuous argon gas purging. The sample mixture was concentrated by drying inside the inert gas chamber and the final volume was around 1-2  $\mu\text{L}$  which was then sandwiched between the two  $\text{CaF}_2$  windows with a fixed sample path length of 10  $\mu\text{m}$ .

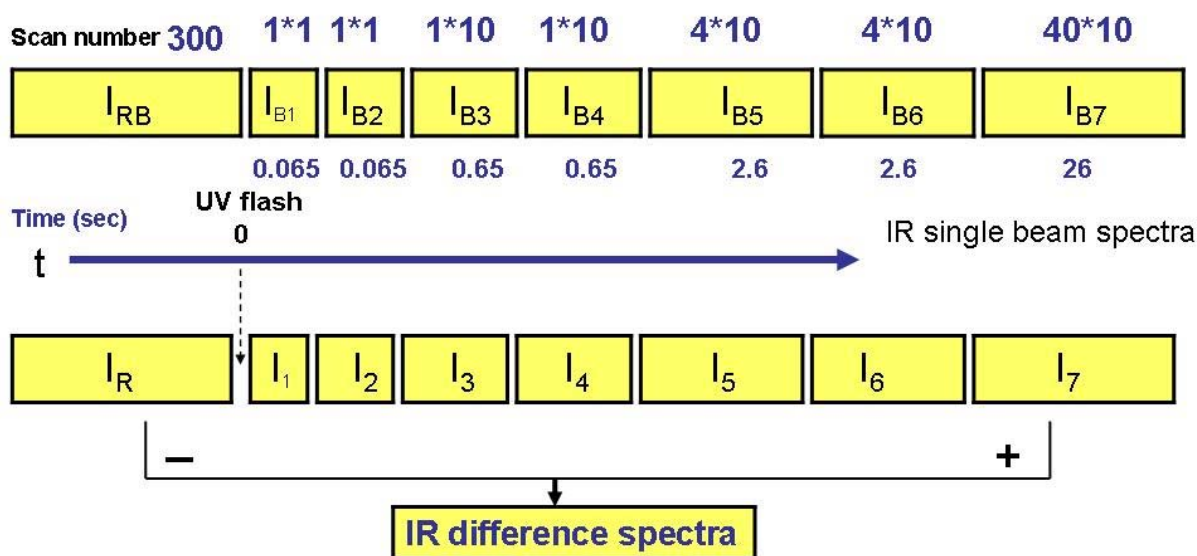


**Figure 14** Scheme describing a typical time-resolved FTIR measurement.

Photolytic release of substrate from caged derivative is triggered by a 20 ns flash (50 mJ/ per area;  $\sim 30$  mJ on sample) from a XeCl excimer laser (HCl/H<sub>2</sub>/Ne/Xe) (RD-EXC-200) from Radiant Dyes Laser Accessories GmbH, Wermelskirchen, Germany. Time-resolved measurements were performed on a modified Bruker (Bruker Optics, Ettlingen, Germany). An IFS 66 spectrometer equipped with a liquid N<sub>2</sub> cooled HgCdTe detector of selected sensitivity. Experimental data were acquired at spectral resolution of 4  $\text{cm}^{-1}$  with the Blackman-Harris 4-term apodization function and a zerofilling factor of two. For an increased sensitivity of FTIR data acquisition, an IR cut off filter of 2000  $\text{cm}^{-1}$  was used. The limiting factors in this technique are the speed of the moving mirror as well as data acquisition and the digitization. The time needed for one interferometer cycle

(double sided, forward-backward mode) is typically 65 ms. A schematic description for a typical time-resolved measurement is shown in Figure 14.

The measurement started with recording of the reference spectrum co-added from 300 scans (baseline spectra) characterising the unperturbed sample. At this point, the time was set to zero and the flash was fired. Subsequently 1 spectrum with 1 scan ( $I_1$ ), 1 spectrum with 1 scan ( $I_2$ ), 10 spectra with 1 scan ( $I_3$ ), 10 spectra with 1 scan ( $I_4$ ), 10 spectra with 4 scans ( $I_5$ ), 10 spectra with 4 scans ( $I_6$ ) and 10 spectra with 40 scans ( $I_7$ ) each were recorded. A kinetic baseline measurement was performed in similar sequence without the photolysis flash before the real measurement. Difference spectra were obtained by subtracting the reference spectrum recorded before the flash from the spectra obtained after photolytic release of substrate (Figure 14). The Bruker OPUS software was used for the rapid acquisition of spectra.

Glutathione, a peptide composed cysteine, glutamic acid and glycine, was used as a radical scavenger for absorbing the photolytic byproducts and as a protectant against oxidative and free radical damage. Dithiothreitol (DTT) can also be used as an alternative to glutathione. In a typical experiment, a reference spectrum coadded from 300 scans was first recorded; then photolysis was induced by applying a single laser flash.

### 2.4.3 ATR-FTIR microdialysis cell

The microdialysis cell has been described in detail previously (Džafic *et al.*, 2009). The instrument involves a microperfusion-cell using a diamond attenuated total reflection (ATR) unit with 7 reflections. The flow ATR unit is divided into two compartments (one for the sample and one for effector molecule) by the dialysis membrane. The membrane is mounted above the diamond. The solution of the target protein in the first compartment with a sample volume of below 5  $\mu\text{L}$  is in contact with the ATR diamond. The second compartment for the flowing effector molecules has a volume of 100  $\mu\text{L}$  which is perfused by a peristaltic pump. One of the major advantages dealing with the microdialysis cell is that the sample volume can be substantially less (below 5  $\mu\text{L}$ ). Equilibration of the protein and effector molecules was reduced by more than a factor of three to four in the presence of an ultrasound head of an ultrasonic scaler (Džafic *et al.*, 2009). The temperature of the ATR-unit is regulated by a circulated water bath. Inside

the ATR perfusion cell an equilibrium spectra of WT QFR in phosphate buffer pH 7.4 was taken and the spectra for fumaric acid and the buffer spectra (taken at identical pH value) was afterwards subtracted in order to obtain the intrinsic effect of fumarate binding to QFR. This difference spectrum arises only due to the secondary structural changes and fumarate binding domain movement of QFR upon fumarate binding to the oxidised protein.

## **2.5 Transient absorption spectroscopy**

### **2.5.1 Sample preparation**

Cells of *W. succinogenes* wild-type enzyme were grown and the QFR enzyme purified by Nicole Hilgendorff according to a protocol described previously (Lancaster *et al.*, 1999). The WT QFR was washed and concentrated in 100 mM potassium phosphate (KPi) buffer at pH 7.4 containing 100 mM KCl as supporting electrolyte and 1 mM *n*-dodecyl- $\beta$ -D-maltoside (cmc = 0.17 mM) (VanAken *et al.*, 1986) as detergent. Samples with protein concentrations of about 1.5 mM were prepared for the spectroscopic experiments. For the necessary washing cycles, Centriscart I filtration tubes with a molecular weight cut-off of 100 kDa and a volume of 2 mL were used.

### **2.5.2 Stationary spectroscopy**

Absorption spectra of WT QFR samples were recorded at room temperature using a Jena-Specord S100 photodiode array spectrometer. Aliquots of the described samples were diluted with adequate buffers by a factor of 10 and measured in 1 mm path length fused silica cuvettes. Absorption spectra were corrected for light scattering.

### **2.5.3 Time-resolved absorption spectroscopy**

The time-resolved measurements were performed using a CLARK CPA 2001 (Dexter, MI, USA) laser/amplifier system operating at a repetition rate of  $\sim$ 1 kHz at a central wavelength of 775 nm (Huber *et al.*, 2001), (Lenz *et al.*, 2006). The QFR samples were excited by pulses generated using a noncollinear optical parametric amplifier (NOPA) with the output tuned to 560 nm for which the maximum excitation energy was kept at 75 nJ. For the probe pulses, a white light continuum was generated by focusing amplified 775 nm light into a 5 mm sapphire window. Femtosecond time delays between

pump and probe were controlled by a translation stage covering delay times up to 1.5 ns (Amarie *et al.*, 2007). To minimize accumulation of photoproducts, the sample was translated continuously both horizontally and vertically in a direction normal to the bisector of the pump and probe beams at ~10 cm/s.

## 2.6 Electrostatic calculations

### 2.6.1 The “Multiconformation Continuum Electrostatics” (MCCE) method

MCCE (Multi-Conformation Continuum Electrostatics), developed by M. R. Gunner and coworkers, is a biophysics simulation program combining continuum electrostatics and molecular mechanics. A detailed description of MCCE can be found in (Alexov and Gunner, 1997) and in (Gunner and Alexov, 2000). The MCCE2.0 includes the "MCCE" main program, the Poisson-Boltzmann equation (Nicholls and Honig, 1991) solver "DelPhi" developed in Barry Honig's Lab (<http://honiglab.cpmc.columbia.edu/delphi>), MCCE tools, and parameter directories. The MCCE method was implemented locally at the MPI of Biophysics by Prof. C. R. D. Lancaster. It allows the determination of the equilibrium conformational and ionization states of all protein side chains, non-solvent exposed water molecules, ions, ligands, cofactors, and prosthetic groups at a given pH and redox potential ( $E_h$ ). It makes use of several pre-selected atomic positions and ionization states for amino acid side chains or heme propionates, cofactors, prosthetic groups, buried waters, and ligands. In the present study, the MCCE method was used to analyze QFR and the enzyme variant in order to determine the ionization changes caused by changes in solution pH or  $E_h$ . Therefore, location and stoichiometry of proton transfers coupled to electron transfer could be well studied. Every individual side-chain conformation and, for practical reasons, also the ionization state of a residue, as well as the reduced or oxidized state of a cofactor (or prosthetic group) is characterized as a “conformer”. In this way, the entirety of conformers represents all allowed states of the protein, which are incorporated into the calculations. Simulated redox titrations are performed by setting a fixed pH value prior to an individual Monte Carlo sampling run (Alexov and Gunner, 1997), (Alexov and Gunner, 1999); (Georgescu *et al.*, 2002) for pH titrations, a fixed potential  $E_h$  is set. In a similar way, possible intermediate steps of electron transfer via the heme groups (see Figure 6) can be simulated by keeping the oxidation state of the hemes and the other cofactors fixed throughout the Monte Carlo

sampling. Subsequently, the protein microstates found can be analyzed with respect to the effect that the fixed charge distribution has on the occupancy of the individual conformers (i.e. the protonation state of an acidic residue in terms of occupancy of the ionized and neutral conformer as well as the side-chain conformation).

## 2.6.2 The individual steps in MCCE calculation

The initialization (program start) reads in control file "run.prm" which must be in the working directory where MCCE program is called. The MCCE program will load parameter files from the parameter directory defined in "run.prm". MCCE program will only read in files with extension ".tpl". The file "new.tpl" is a parameter file similar to those in the parameter directory except no charges are assigned to any atom. This file is for unrecognized residues or cofactors. There is no output file from the program initialization, but the initialization creates a parameter database to hold information from the parameter files and dynamically generated parameters by the program.

There are four major steps in a MCCE calculation. These four steps are connected by a few files. The program is designed to run through without stopping although it is possible to stop the program at each step and edit the files to instruct the next step. Here is the summary of the function of these 4 steps.

### 2.6.2.1 Step1: formatting pdb file

The Step 1 formats the pdb file and thus prepares an extended pdb file suitable to be read into step 2. The input pdb file is in standard pdb format. It can have alternative side chain positions, but MCCE can not process alternative backbone positions. Alternative side chains are treated as side chain conformers. When side chain atoms are missing, MCCE will complete the side chain atoms at the torsion minimum.

### 2.6.2.2 Step2: Making rotamers

Step 2 makes and optimizes rotamers (Dunbrack and Karplus, 1994), (Dunbrack and Cohen, 1997) from the structure in "step1\_out.pdb" (step 1 output file is in MCCE extended pdb format). In this step, the rotatable bonds (defined in parameter files) of each residue are rotated by the steps defined in "run.prm". Then the self van der Waals (VDW) potential (interaction among atoms of the same side chain excluding 1-2 and 1-3 interactions, and interaction between the side chain and backbone atoms) is calculated.



Side chain rotamers with high self VDW potentials are deleted. Then the side chains are optimized with possible hydrogen bond partners. A number of repackings starting from randomized initial structures (one conformer from one residue) are performed to reduce side chain rotamers to those with low energy local packings. Ionization states are then created and protons are placed on side chains. At the end of side chain rotamer optimization, MD simulations are carried out locally to relax the structure.

#### *2.6.2.3 Step3: calculating the energy lookup table*

The Step 3 calls PB equation solver, DelPhi, to calculate reaction field energy and electrostatic pairwise interaction. The result is stored as together with van der Waals interactions as one file per conformer. These files have extension "opp" and are located under directory energies. The self-energy terms (not dependent on side chains of other residues) of conformers are listed in file "head3.lst" The progress is dynamically updated in file "progress.log".

#### *2.6.2.4 Step 4: simulating pH or $E_h$ titration with Monte Carlo sampling*

The step 4 is a titration simulation by Monte Carlo sampling (Alexov and Gunner, 1997), (Alexov and Gunner, 1999). The Monte Carlo sampling is performed at specified set of pH/ $E_h$ . At each titration point, there will be several (predefined in "run.prm") independent samplings. Each sampling goes through annealing, reducing, and equilibration stages. Statistics of conformer occupancy is only done at equilibration stage. The results of step 4 are reported as conformer occupancy in file "fort.38", residue net charge in file "sum\_crg.out" and fitted pKa/ $E_m$  values in file "pK.out".

### **2.6.3 Simulated pH titrations**

Simulated pH titrations were performed by setting a fixed ambient redox potential before an individual Monte Carlo sampling run. In a similar way, possible intermediate states of electron transfer via the heme groups can be simulated by keeping the oxidation state of the hemes and the other cofactors fixed throughout the Monte Carlo sampling. Subsequently, the found protein microstates can be analyzed with respect to the effect that the fixed charge distribution has on the occupancy of the individual conformers (i.e. the protonation state of an acidic residue in terms of occupancy of the ionized and

---

neutral conformer as well as the side-chain conformation). Due to the large size of the QFR protein complex, the calculations were restricted to the coordinates of subunits B and C and the respective prosthetic groups of one QFR monomer without any membrane model. A set of 21 water molecules, which were found in the crystal structure within a radius of 9 Å around the heme propionates of the two heme *b* groups and amino acid residue Glu C180, was included in the QFR model.

## 3 Results

### 3.1 Electrochemically induced static FTIR approaches

#### 3.1.1 pH-dependence of the protonation of Glu C180 with heme redox transition in QFR WT

All presented spectra were normalized to a level that represents the average maximal absorbance difference ( $\Delta$  Abs) in the amide I range of all difference spectra that have been selected for presentation. The pH dependence of electrochemically induced FTIR difference spectra QFR WT enzyme has been reported earlier (Haas *et al.*, 2005). In the oxidised-minus-reduced spectral frequency range of (de)protonated carboxyl groups from pH 5.5 to pH 8.8, there is observed a trend of decreasing band intensity at the  $1740\text{ cm}^{-1}$  band (Haas *et al.*, 2005).

#### 3.1.2 The pH-dependence comparison of E180Q enzyme variant with wild-type enzyme

To find the dependence of Glu C180 signal on the individual heme redox transition, pH dependent redox FTIR measurements of E180Q mutant have been performed. Very similar patterns of spectral features are reflected in the pH dependency (see Figure 15). At a low pH value such as pH 5.5, the observed signals are minimal. Analogous to the wild-type spectra, significant spectral changes occur between pH 7.5 and pH 8.5.

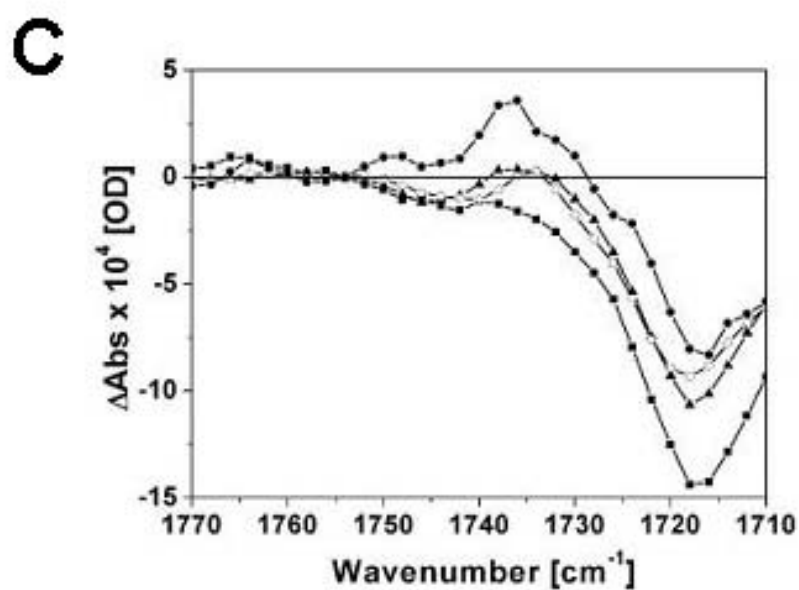
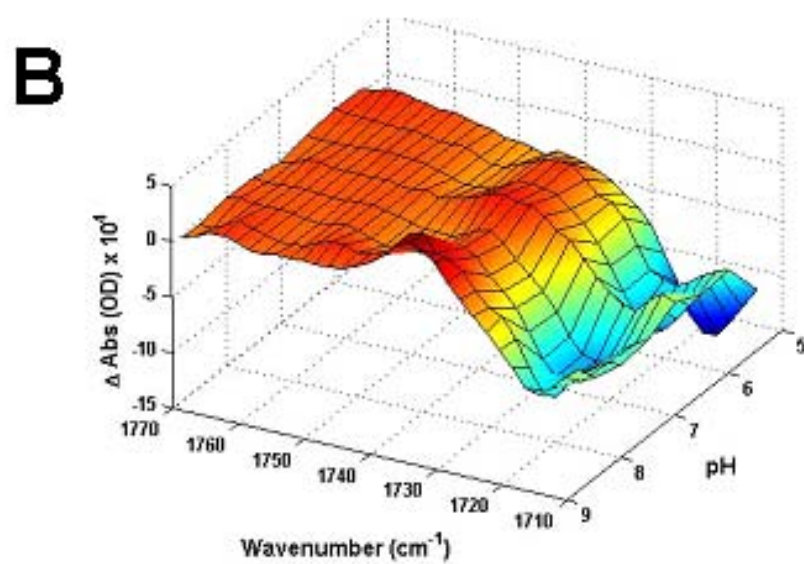
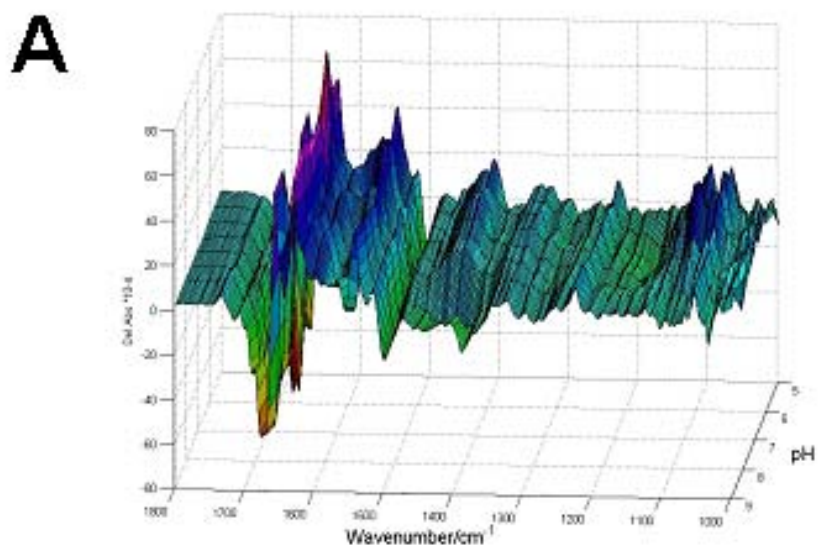


**Figure 15** The pH dependence of electrochemically induced FTIR difference spectra. Overlay of reduced-minus-oxidized difference spectra of QFR E180Q A) 3D view of the full wave number region (from 1800 to 1000  $\text{cm}^{-1}$ ). B) 3D view of the selected wave number region (from 1770 to 1710  $\text{cm}^{-1}$ ). C) view of the selected wave number region (from 1770 to 1710  $\text{cm}^{-1}$ ) at pH 5.5 (squares), pH 6.5 (triangles), pH 7.5 (open circles) and pH 8.5 (filled circles). Reference electrode potentials for the shown FTIR difference spectra were +0.21 V (full oxidative potential) and -0.37 V (full reductive potential) (Paul *et al.*, *manuscript in preparation*), (Haas *et al.*, 2005).

Figure 16 and Figure 17 shows the pH dependence of the electrochemically induced FTIR double difference spectra (WT-minus-E180Q) within a physiological pH range. The subtraction of the single difference spectra of the E180Q variant enzyme from that of the wild-type enzyme results in such complex spectral patterns where only the neat contribution from the Glu C180 residue is reflected. Although similar double difference spectra has previously been calculated and reported only for pH value 7.0 (Haas *et al.*, 2005), the isolated contribution of Glu C180 residue over a broad physiological pH range has been studied here. The protonation (deprotonation) event of that particular amino acid residue can be followed in this study. The double difference spectral pattern, although being complex in nature, can hint the stretching vibration of the carboxylic acid residue at around 1740  $\text{cm}^{-1}$  region.

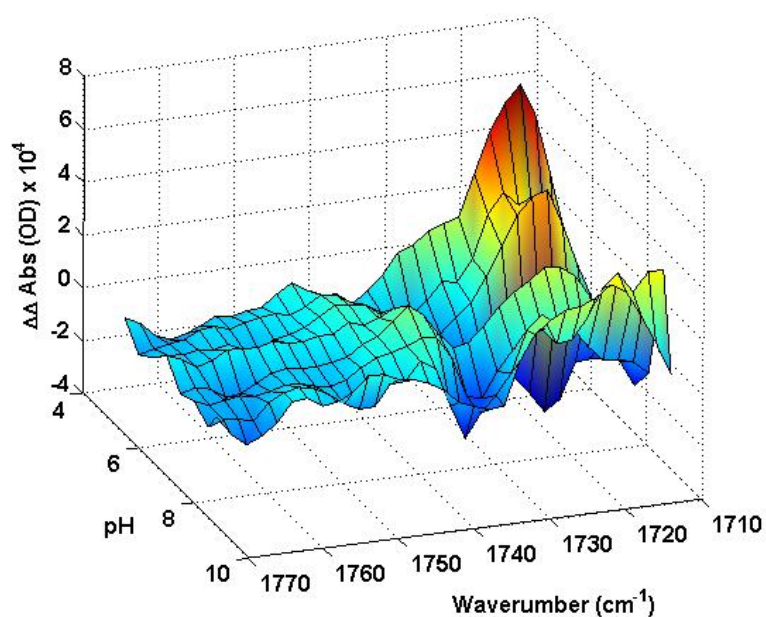


**Figure 16** The pH dependence of electrochemically induced FTIR double difference spectra. Selected (from 1770 to 1710 cm<sup>-1</sup>). 3D view of the overlay of reduced-minus-oxidized difference spectra of QFR WT-minus-E180Q. Reference electrode potentials for the shown FTIR double difference spectra were +0.21 V (full oxidative potential) and -0.37 V (full reductive potential).

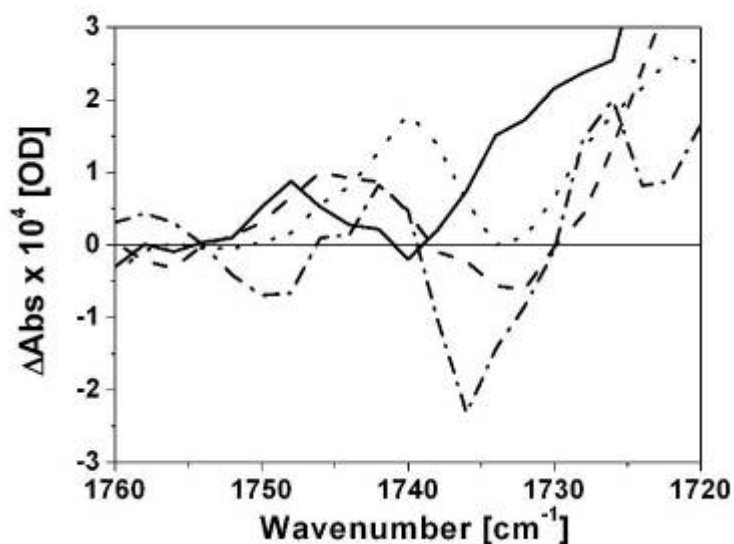


**Figure 17** The pH dependence of the FTIR double difference spectra of QFR WT-minus-E180Q (from 1760 to 1720 cm<sup>-1</sup>). Overlay of reduced-minus-oxidized difference spectra of QFR E180Q at pH 5.5 (solid line), pH 6.5 (dashed line), pH 7.5 (dotted line) and pH 8.5 (dashed-dotted line). Reference electrode potentials for the shown FTIR double difference spectra were +0.21 V (full oxidative potential) and -0.37 V (full reductive potential).

---

Analogous measurements have also been performed involving intermediate heme redox potential. The reduced-minus-intermediate spectra correspond to the “low-potential step” and the intermediate-minus-oxidized spectra correspond to the “high-potential step”. The “full-potential step” is measured to those computed by summation of the spectra of the “low-potential step” and “high-potential step”. By plotting the values of the double difference spectral intensity in Figure 18 A, it is possible to specifically trigger only a single heme redox transition event and its consequence on the protonation (deprotonation) phenomena on Glu C180 residue can be followed. One of the obvious observations that come out from this experiment was that the maximal contribution in the double-difference spectra in the full potential range originates from the redox transition of the high potential proximal heme  $b_P$ . In addition, the double difference signals arising from the full redox potential step and those computed from the addition of those arising from the two individual redox steps exhibit a reasonable match.

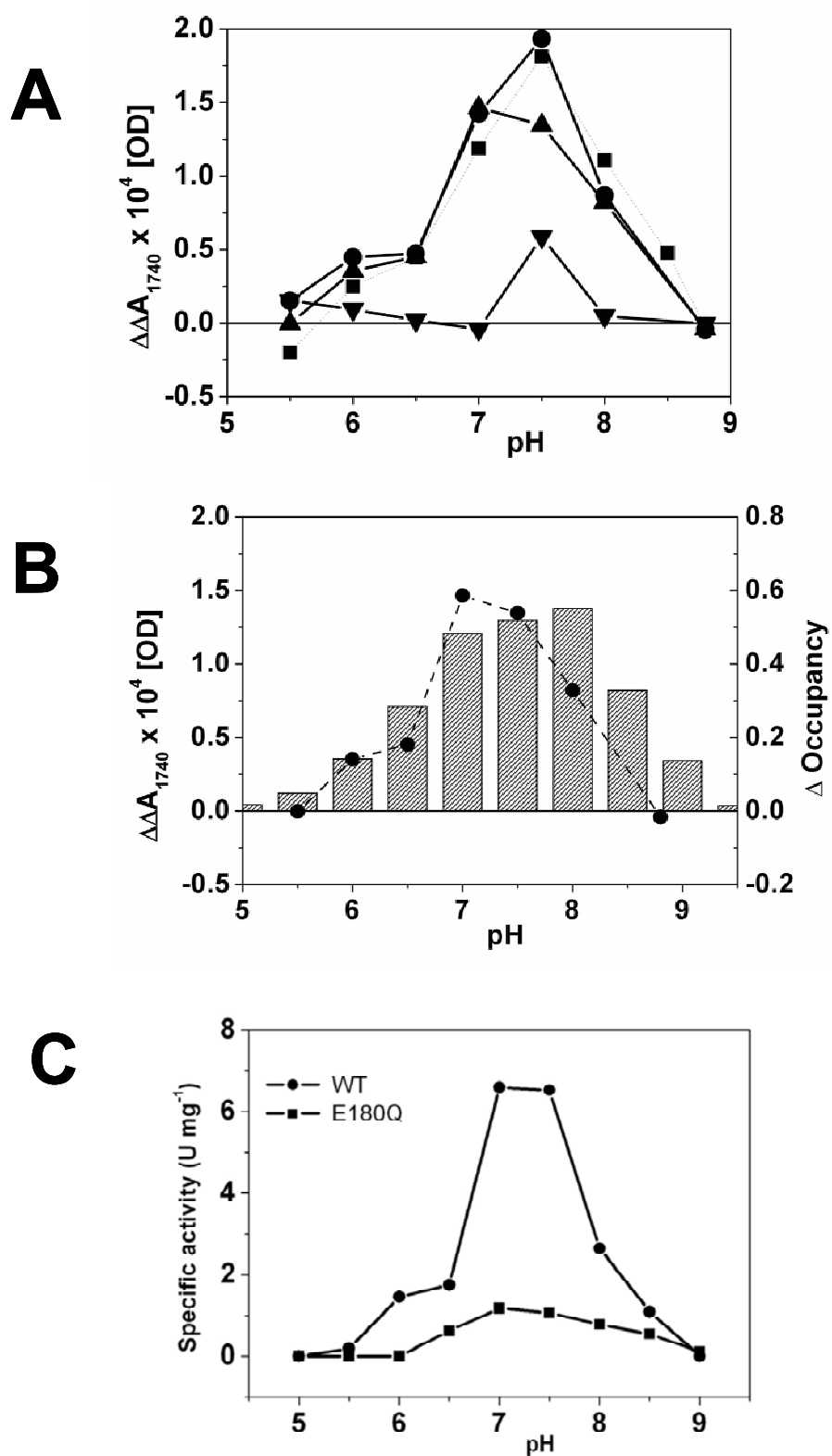




**Figure 18 A)** The pH dependence of the FTIR double difference spectra of QFR WT-minus-E180Q at  $1740\text{ cm}^{-1}$ . Superposition of “reduced-minus-intermediate” potential step (inverse triangles), “intermediate-minus-oxidized” potential step (triangles), “reduced-minus-oxidized” full potential step (squares), and computed spectra (sum of “reduced-minus-intermediate” and “intermediate-minus-oxidized”) (circles). **B)** The pH dependence of the FTIR double difference spectra of QFR WT-minus-E180Q at  $1740\text{ cm}^{-1}$ . Superposition of “intermediate-minus-oxidized” potential step (circles), simulated pH titration of Glu C180  $b_D^{\text{ox}} b_P^{\text{red}}$ -minus- $b_D^{\text{ox}} b_P^{\text{ox}}$  (shaded columns) (Haas and Lancaster, 2004). Reference electrode potentials for the shown FTIR double difference spectra were +0.21 V (full oxidative potential) and -0.37 V (full reductive potential). (A constant of the order of the noise level was subtracted to guarantee zero-crossings of the pairs of double difference spectra at the same wavenumber. This procedure is identical with setting the spectra to zero at wave number around  $1760\text{ cm}^{-1}$  and above where no further signals were observed). **C)** Specific activities for  $\text{DMNH}_2$  oxidation by fumarate of wild-type (circles) and Glu C180  $\rightarrow$  Gln variant (squares) QFR from *Wolinella succinogenes* as a function of pH (Paul *et al.*, manuscript in preparation). The activities were measured as described by Uden *et al.* (Uden *et al.*, 1980) with the following modifications: the temperature was  $36^\circ\text{C}$  and the buffer used was a mixture of 50 mM citrate, 50 mM potassium phosphate, 50 mM tris, 50 mM glycine and 50mM glycyglycine. The pH values were adjusted with NaOH.

### 3.1.3 Individual heme porphyrin signal with heme redox transition

#### 3.1.3.1 Spectral contribution from protein backbone and side chain residues

The full spectral region  $2000\text{-}600\text{ cm}^{-1}$  shows a large number of well-pronounced positive and negative bands. The vibrational contribution of the IR active side chains in the  $1800\text{-}1400\text{ cm}^{-1}$  region has been thoroughly investigated earlier (Haas *et al.*, 2005) and is hence important in explanation of the cases in which the residues undergo protonational/deprotonation events (Haas *et al.*, 2005), (Venyaminov and Kalnin, 1990a), (Venyaminov and Kalnin, 1990b). The positive and negative difference peaks arise due to the change in contribution upon oxidation and reduction of the protein, respectively. In Figure 19, trace “t” depicts the oxidised–minus–reduced FTIR difference spectrum of QFR wild-type in the  $1000\text{--}650\text{ cm}^{-1}$  range. Traces “l” and “h” in Figure 19 show the spectral contribution from the low- and high- potential heme, respectively. Their individual spectral contribution is obtained by applying a selected redox step to the sample.

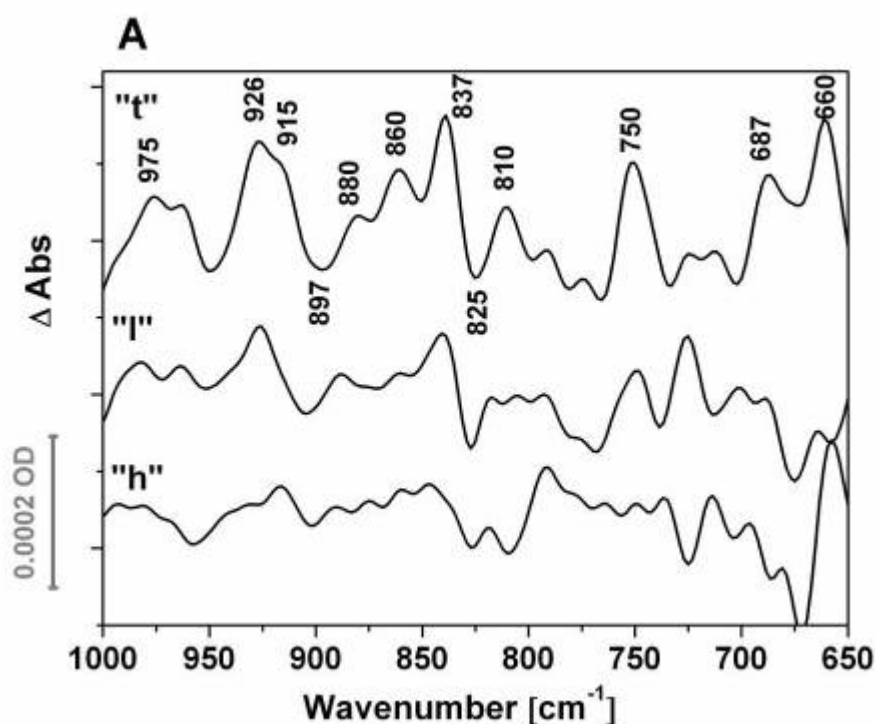


**Figure 19** Oxidised-minus-reduced FTIR difference spectra of *W. succinogenes* QFR at pH 7.4; The reference electrode potentials (vs. SHE) for the spectra displayed here were +0.21 V (full oxidative potential) and -0.37 V (full reductive potential), -0.13 V (intermediate potential) trace "t": Contribution of both hemes transition, (oxidised-minus-reduced) trace "l": Contribution of low potential heme  $b_D$  transition, (intermediate-minus-reduced) trace "h": Contribution of high potential heme  $b_P$  transition, (oxidised-minus-intermediate) (The wavenumbers of the bands as assigned in the text and Table 5).

The particular heme redox difference signal in the full spectra can now be depicted. The sum the respective spectra of "l" and "h" is shown in Figure 20 (red line) and compared with the full spectral range spectra at pH 7.4 (solid line). The spectral discrepancy in the measurements can arise due to the differences in equilibrium time and differences in the number of redox cycles performed during sample measurements. A detailed description of the experimental parameters has been provided in spectroelectrochemistry part in section 2.3.4.2. It is evident that the FTIR difference spectral combination of individual heme  $b_H$  and heme  $b_L$  redox transitions correlates reasonably with that of full potential redox difference spectra (Figure 20). Interestingly, the FTIR difference signals arising due to the redox transition of heme  $b_L$  apparently have a higher absorption coefficient than those of heme  $b_D$  to the full potential FTIR difference spectra (in the spectral range 1000-500  $\text{cm}^{-1}$ ).

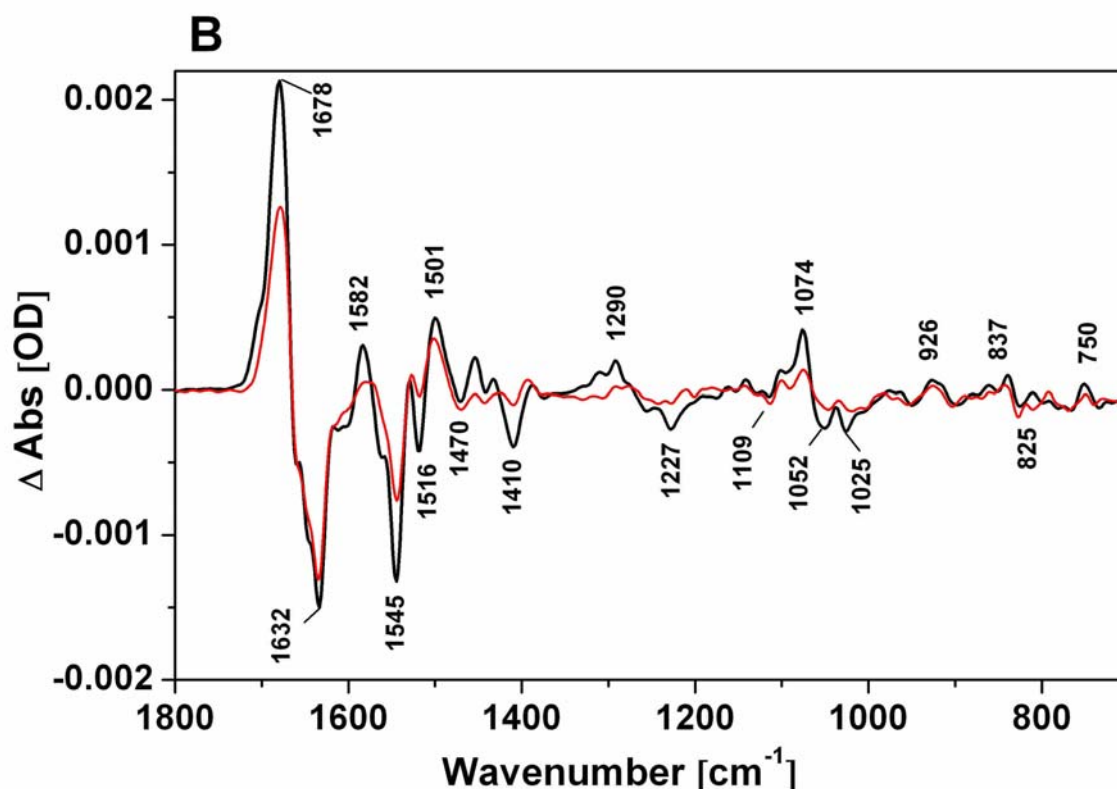


**Figure 20** Spectral summation (red line) of trace “l” (contribution of low potential distal heme  $b_D$  transition) and trace “h” (contribution of high potential proximal heme  $b_P$  transition) and its comparison with full potential range spectra (black line, i.e. trace “t”).

The superposition of the difference spectra at pH 7.4 (solid line) and pH 8.5 (gray line) in Figure 21, in the spectral range from 1000-600  $\text{cm}^{-1}$  demonstrates reproducible data that can be obtained with two different pH values. The variation of the pH above pH 7.4 does not significantly influence the low infrared spectral range. Specific spectral differences arise within the spectral range of 1300-1000  $\text{cm}^{-1}$  due to the use of different buffers for measurements at two different pH values. Below 700  $\text{cm}^{-1}$ , the signal to noise ratio is too high in the redox difference spectra at pH 8.5 (Figure 21) and this spectral region is not shown.

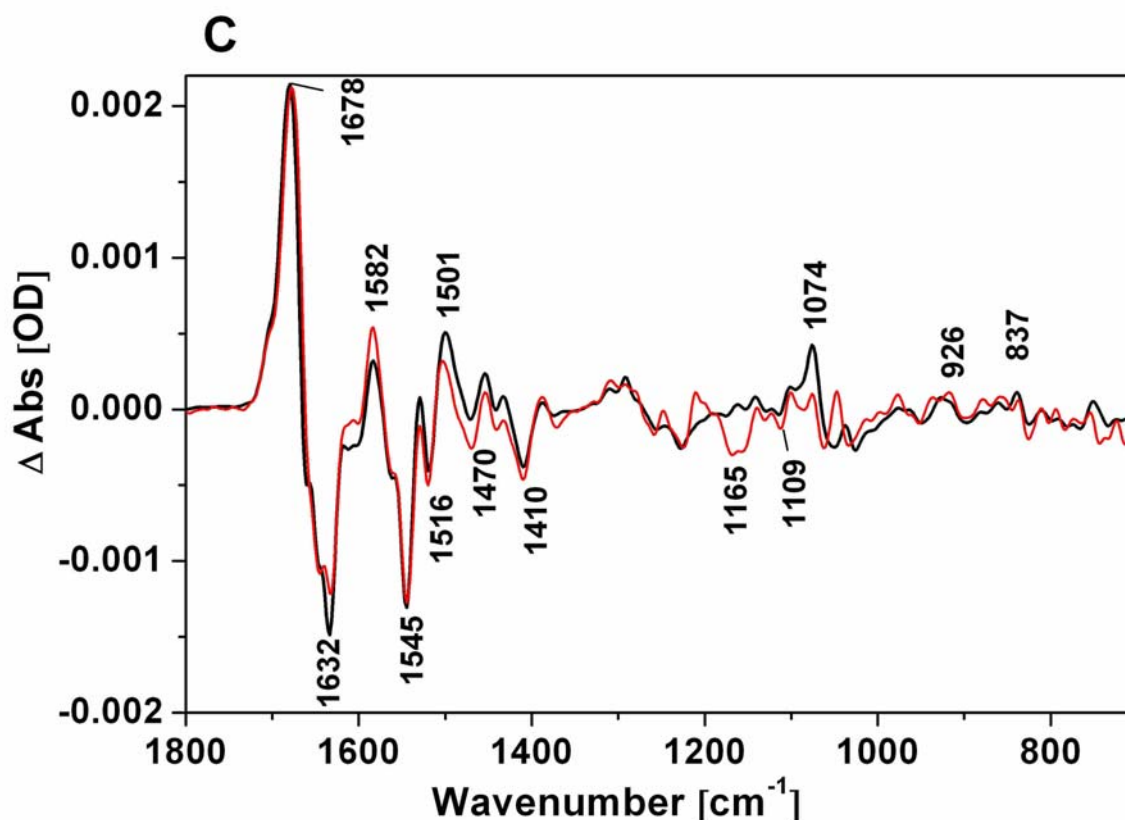


**Figure 21** Superimposition of full potential range spectra at pH 7.4 (black line, i.e. trace “t”) and full potential range spectra at pH 8.5 (red line). (For a more detailed assignment of IR bands above 1000  $\text{cm}^{-1}$ , see (Haas *et al.*, 2005))

In the low pH range (pH 5.6), a stronger contribution in FTIR difference spectral features due to heme  $b_L$  redox transition is found (Figure 22). There are a number of interesting features observable in low pH difference spectra. At low pH, the difference spectra at  $915 \text{ cm}^{-1}$  shows a negative peak (Figure 22, trace 2A); whereas at high pH values this peak is shoulder at a positive peak (Figure 19, trace “t”). Secondly, the major difference at low pH are two positive peaks at  $875 \text{ cm}^{-1}$  and  $837 \text{ cm}^{-1}$  and a strong negative peak at  $864 \text{ cm}^{-1}$  (Figure 22, trace 2A). Furthermore, a shift of  $9 \text{ cm}^{-1}$  is found for the signal at  $750 \text{ cm}^{-1}$  to  $741 \text{ cm}^{-1}$ .

Strong FTIR difference bands at the mid IR range (amide I and amide II) suggested a redox-triggered local structural reorganisation, which has been previously described in detail by Haas *et al.* (Haas *et al.*, 2005). In the amide I range ( $1690\text{-}1610 \text{ cm}^{-1}$ ), strong FTIR difference bands at  $1678 \text{ cm}^{-1}$  (turns &  $\beta$ -sheets) and  $1632 \text{ cm}^{-1}$  ( $\beta$ -

sheets) signifies the absorption changes of C=O stretching vibrations from the polypeptide backbone (Haas *et al.*, 2005), (Mäntele, 1993). In the amide II range (1580-1510  $\text{cm}^{-1}$ ), coupled C-N stretching and N-H bending modes contribute with strong bands at 1545  $\text{cm}^{-1}$  and 1530  $\text{cm}^{-1}$ .

In the following discussion the spectral contributions of heme propionates, porphyrin ring and metal-ligand vibrations are presented in detail.

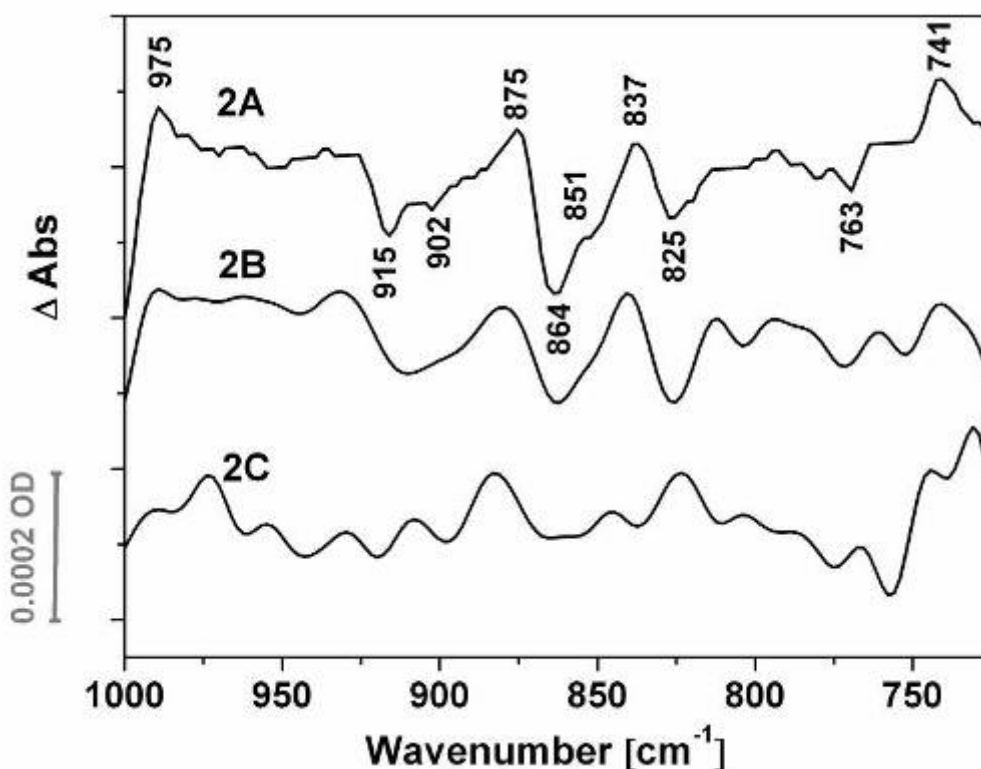


**Figure 22** Oxidised-minus-reduced FTIR difference spectra of *W. succinogenes* QFR at pH 5.6; The reference electrode potentials (vs. SHE) for the spectra displayed here were +0.21 V (full oxidative potential) and -0.37 V (full reductive potential), -0.18 V (intermediate potential); trace 2A: Contribution of both hemes transition, (oxidised-minus-reduced); trace 2B: Contribution of low potential heme  $b_D$  transition, (intermediate-minus-reduced); trace 2C: Contribution of high potential heme  $b_P$  transition, (oxidised-minus-intermediate), (The wavenumbers of the bands as assigned in the text and Table 5).

### 3.1.3.2 Spectral contribution from heme propionates

In the mid IR range the carbonyl stretching modes of protonated heme propionates contribute at 1702  $\text{cm}^{-1}$ , 1692  $\text{cm}^{-1}$  and 1560  $\text{cm}^{-1}$  (Behr *et al.*, 1998). They were previously assigned for QFR by Haas *et al.* (Haas *et al.*, 2005). Symmetric and antisymmetric  $\nu(\text{COO}^-)$  vibrations were observed for the deprotonated form of heme

propionate. Signals were overlapped as the strong amide I mode dominates due to the protein backbone contribution. In the lower frequency range no significant contributions from the heme propionates are expected.

### 3.1.3.3 Spectral contribution from porphyrin ring vibrations

To probe the nature of the redox dependent changes in the heme porphyrin ring system in QFR, specific vibrational modes were monitored. The  $\nu(\text{C}_m\text{H})$  out-of-plane heme porphyrin mode is attributed to the signal at  $837\text{ cm}^{-1}$  in the oxidised state and to the  $825\text{ cm}^{-1}$  peak in the reduced state of the enzyme (Figure 19, trace “t”) (Berthomieu *et al.*, 2006). This spectral feature at  $837/825\text{ cm}^{-1}$  shows no significant pH dependence as the signals are comparable in the different pH values studied (see Figure 19 and Figure 22) although at low pH value the  $\nu(\text{C}_m\text{H})$  mode displays a broader feature with a prominent difference peak at  $864\text{ cm}^{-1}$  (red) and a shoulder peak at  $851\text{ cm}^{-1}$  (reduced) (Figure 22, trace 2A). Protonation of the heme propionate at low pH can influence the  $\nu(\text{C}_m\text{H})$  mode and therefore lead to the two latter peaks. Alternatively, other spectral features can be involved. The  $864\text{ cm}^{-1}$  peak is arising also due to histidine residues in the reduced state of the enzyme. In previous studies by Dörr *et al.* (Dörr *et al.*, 2006) on hematin and protoporphyrin-IX, the  $\nu(\text{C}_m\text{H})$  vibrational mode of the porphyrin ring was reported to depend on the protonation state of the heme propionate side chain and hence a pH dependent behaviour was observed. The band at  $750\text{ cm}^{-1}$  (ox) may arise due to the breathing of the porphyrin ring (Dörr *et al.*, 2006) which shifted at  $741\text{ cm}^{-1}$  (ox) at low pH value. This may be a result of protonation of the propionate side chain upon reduction. Other far-infrared difference spectroscopic studies on heme model compounds reported difference bands at  $839(\text{ox})/830(\text{red})\text{ cm}^{-1}$  (Berthomieu *et al.*, 2006). The internal modes of the axial histidine and imidazole ligands ( $670\text{-}580\text{ cm}^{-1}$ ) and deformation modes of the heme pyrroles ( $420\text{-}370\text{ cm}^{-1}$ ) are sensitive to the iron coordination and redox state of the heme iron (Marboutin *et al.*, 2006), (Xerri *et al.*, 2009).

### 3.1.3.4 Spectral contribution from metal-ligand vibrations

Based on sequence alignment (Körtner *et al.*, 1990), site-directed mutagenesis (Simon *et al.*, 1998) and the three-dimensional structure of *W. succinogenes* QFR (Lancaster *et*

*al.*, 1999), it was found that four histidine residues are the ligands to the heme *b* groups. The axial ligands of the distal heme *b<sub>D</sub>* are His C44 of the transmembrane segment I and His C143 of the transmembrane segment IV. In the case of the proximal heme, the ligands are His C93 and His C182. Histidines are well recognised as heme-ligating residues and can act as proton acceptors (or donors) in hemoproteins (Martin *et al.*, 1985). The imidazole ring of the histidine ligand possesses two protonable (deprotonable) nitrogen atoms. Therefore depending on the protonation of nitrogen, it can generate four distinct forms (Hasegawa *et al.*, 2000). The  $pK_a$  of the imidazolium ion in water is 7.0 (Frey *et al.*, 1994). In the microenvironment of a protein (in the active site, for example) this value can be lowered and is usually close to 6.0 (Hasegawa *et al.*, 2000). Therefore, histidine can serve as hydrogen-bond donor and acceptor within physiological pH range playing crucial role as a proton transfer mediator in various proton-transfer reactions (Frey *et al.*, 1994), (Hays *et al.*, 1998). As FTIR difference spectroscopy can detect subtle changes at molecular level, even the contribution of a single amino acid within the active site of a protein, conformational changes and heme-histidine interactions can be well studied using this technique. In a far infrared spectroscopic study by Dörr *et al.* (Dörr *et al.*, 2007) on Fe-Im vibrations involving bis(imidazole)-iron protoporphyrin compound showed imidazole-iron-imidazole vibrations at 396/386/378/317  $\text{cm}^{-1}$  for hemin with imidazole.

In the oxidised-minus-reduced difference spectra of *W. succinogenes* QFR, signals at 975, 926, 915, 860 and 624  $\text{cm}^{-1}$  (Figure 19, trace “t”; and Table 5 and the references therein) include possible contributions from histidines (Hasegawa *et al.*, 2000), (Mesu *et al.*, 2005). The band positions around 926  $\text{cm}^{-1}$  and 915  $\text{cm}^{-1}$  form a broadened spectral feature. Two distinct bands are assigned to histidine vibrations. One of these bands (at 926  $\text{cm}^{-1}$ ) appears upon redox transition of the heme *b<sub>L</sub>* and the other one at (915  $\text{cm}^{-1}$ ) appears upon redox transition of the heme *b<sub>H</sub>* (Figure 19, trace “l” and “h”). At low pH values, the spectral characteristics are substantially changed due to a negative difference peak at 915  $\text{cm}^{-1}$  (red) and a small shoulder peak at 902  $\text{cm}^{-1}$  (red) (Figure 22, trace 2A). The following bands assignments that are typical for histidine are based on work reported by Hasegawa *et al.* (Hasegawa *et al.*, 2000) and Mesu *et al.* (Mesu *et al.*, 2005). Our data suggests that the reduced form of the enzyme favours the protonation of histidine at low pH value. The essential part of the contribution seems to

originate from heme  $b_L$  (Figure 19, trace “t” for total contribution and trace “l” for heme  $b_D$  contribution). This supports that the redox transition of the low potential distal heme is crucial for the histidine protonation/deprotonation event to occur. A very similar signal pattern has been observed at  $860\text{ cm}^{-1}$  (ox) (Figure 19, trace “t”) which changes to a strong negative peak at  $864\text{ cm}^{-1}$  (red) (Figure 22, trace 2A) accompanied by the positive peak shift to  $875\text{ cm}^{-1}$  (ox) (Figure 22, trace 2A) at low pH value. (Hasegawa *et al.*, 2000), (Mesu *et al.*, 2005). The low IR spectra below  $700\text{ cm}^{-1}$  was rather noisy and therefore wavenumber region lower than  $700\text{ cm}^{-1}$  has not been shown.

Table 5 Summary of tentative IR band assignments (from  $1000\text{ cm}^{-1}$  to  $600\text{ cm}^{-1}$ ) for *W. succinogenes* QFR. (For a more detailed assignment of IR bands above  $1000\text{ cm}^{-1}$ , see (Haas *et al.*, 2005)).

Wavenumber ( $\text{cm}^{-1}$ )	redox state	tentative assignments	references
1109	red	protonated histidine	(Mesu <i>et al.</i> , 2005)
975	ox	histidine, porphyrin ring	(Hasegawa <i>et al.</i> , 2000), (Wolpert and Hellwig, 2006)
926	ox	histidine, porphyrin ring C-N	(Hasegawa <i>et al.</i> , 2000), (Wolpert and Hellwig, 2006)
915	ox	histidine	(Hasegawa <i>et al.</i> , 2000), (Mesu <i>et al.</i> , 2005), (Wolpert and Hellwig, 2006)
915	red	histidine pH dependent shift	(Hasegawa <i>et al.</i> , 2000), (Mesu <i>et al.</i> , 2005)
897	red	porphyrin ring	(Dörr <i>et al.</i> , 2008)
875	ox	histidine pH dependent shift	this thesis
860	ox	histidine, porphyrin ring (pH dependent)	(Dörr <i>et al.</i> , 2006), (Mesu <i>et al.</i> , 2005)
864	red	protonated histidine	(Hasegawa <i>et al.</i> , 2000), (Mesu <i>et al.</i> , 2005)
837	ox	$\nu(\text{C}_m\text{H})$ out-of-plane porphyrin	(Berthomieu <i>et al.</i> , 2006)
825	red	$\nu(\text{C}_m\text{H})$ out-of-plane porphyrin	(Berthomieu <i>et al.</i> , 2006)
750	ox	methionine, porphyrin breathing mode	(Dörr <i>et al.</i> , 2006), (Wolpert <i>et al.</i> , 2004)
741	ox	porphyrin breathing mode pH dep. shift	this thesis
687	ox	$\nu(\text{CS})$ & $\nu(\text{CSC})$ methionine, porphyrin	(Wolpert <i>et al.</i> , 2004)



Notes:

(i)  $687\text{ cm}^{-1}$  band may also originate from a pH dependent heme porphyrin ring vibration (with a possible involvement of COO heme propionate movement) (Boucher and Katz, 1967), (Lancaster *et al.*, 2005).

(ii)  $750\text{ cm}^{-1}$  mode can be due to S-CH<sub>2</sub>/CH<sub>3</sub> vibration in methionine (Venyaminov and Kalnin, 1990a).

(iii) Broad spectral feature around  $966$  and  $975\text{ cm}^{-1}$  are due to a histidine residue overlapped with C-N and C-C stretching vibration of backbone.

(iv) The broad  $897\text{ cm}^{-1}$  (red) signal is from from the deprotonated heme porphyrin ring. This indicates that the heme porphyrin becomes deprotonated upon heme reduction.

## 3.2 Time-resolved FTIR approaches

In section 3.2.1, a detailed description of the initial characterisation results of the caged fumarate and time-resolved approaches to characterise the released fumarate binding to QFR is presented. In section 3.2.2, spectroscopic characterisation of the caged quinol is shown. FTIR difference spectra of the released quinol analog in presence of QFR enzyme is presented in detail.

### 3.2.1 Caged fumarate

Synthesis and NMR spectroscopic characterisations of the caged fumarate are described in the material and method part (see section 2.4.1.1). In section 3.2.1.1 to section 3.2.1.11, results from the the UV/VIS and FTIR spectroscopic characterisation of the caged fumarate is shown. The substrate fumarate releases only after implying the laser flash. The release occurs on a submillisecond time scale. Initiation of the enzymatic reaction upon release of fumarate is described. Interaction of fumarate with QFR is shown from the time-dependent evolution of the FTIR difference spectra.

#### 3.2.1.1 UV VIS spectra of caged fumarate

Optical absorbance measurements of CNB-caged fumarate in ethanol solvent were performed with the help of a diode-array UV/VIS spectrophotometer (Agilent 4853). The wavelength range from 200 nm to 700 nm was studied. Caged fumarate showed a stronger absorption peak at 212 nm and a smaller broad peak at 266 nm (Figure 23).

The difference spectra of caged fumarate after several laser flashes compared to the unphotolysed sample showed differences with positive peaks at 237 nm and 315 nm and a strong negative peak at 266 nm (data not shown), the isobestic point being located at 254 nm.

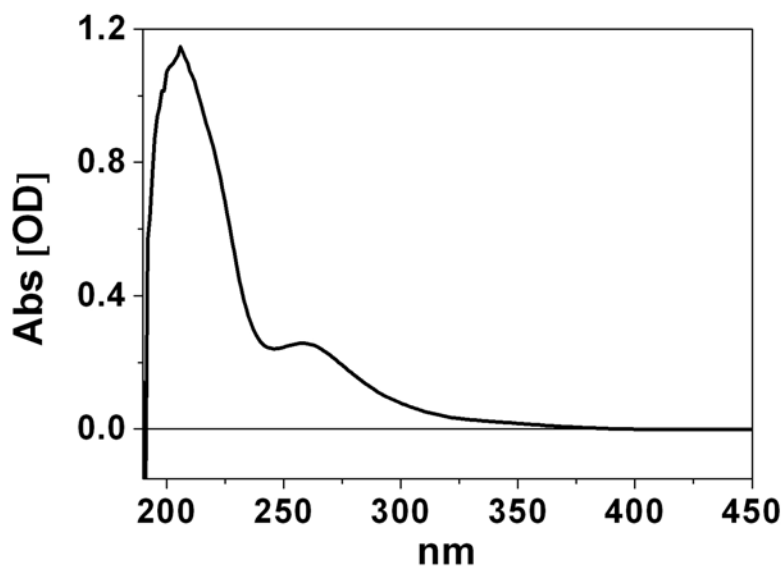


**Figure 23** Absorption spectra of caged fumarate (100 mM caged was diluted in ethanol solvent to a final measurement volume of 200  $\mu$ L; the cuvette pathlength was 1 mm).

These data are very similar to the CNB-glutamate data (Figure 24) with a slightly shifted isobestic point that can be a result of baseline drift and/or additional photoproducts (Gee *et al.*, 2002).

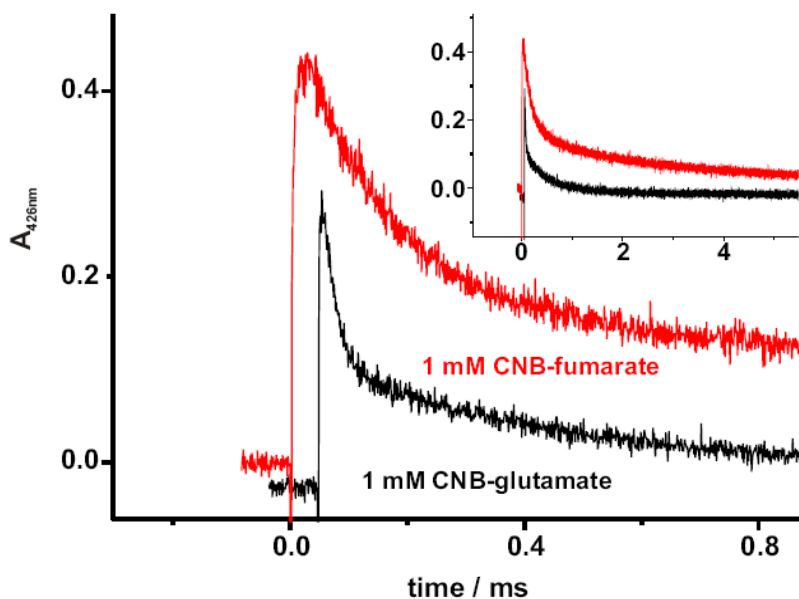


**Figure 24** Photolysis of CNB-fumarate and CNB-glutamate in 50 mM K-phosphate, pH 7.4. The reaction was started by a laser flash from a XeCl excimer laser (308 nm, 60 mJ) and absorbance changes were followed by a home-built single-wavelength spectrometer.

### 3.2.1.2 IR absorption spectra of caged fumarate

The infrared absorption spectrum of caged fumarate (a) and caged fumarate with WT QFR (b) is illustrated in Figure 25. Both IR spectra presented here are dominated by the intense water absorption at  $1648\text{ cm}^{-1}$ . Amide II band at  $1550\text{ cm}^{-1}$  is present in the cage with QFR spectra (solid line). However, minute spectra feature at  $1530\text{ cm}^{-1}$  can be observed (more prominent in the difference IR spectra) due to the antisymmetric vibration of the nitro group present in the cage.

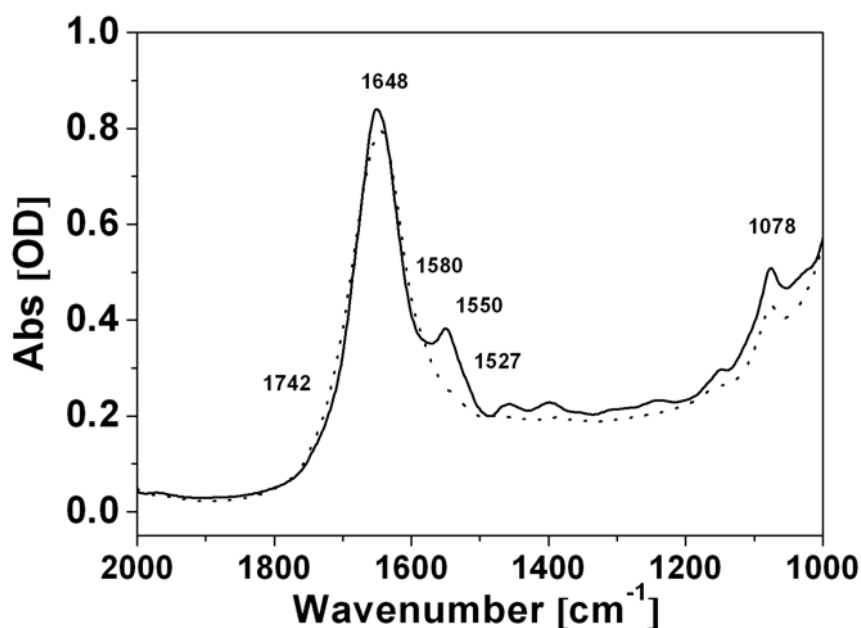


**Figure 25** IR absorption spectra of caged fumarate only (dotted line) and caged fumarate with WT QFR (solid line). (20 mM caged fumarate, 1 mM WT QFR, 10 micrometer pathlength in the IR cuvette, 5°C, 100 mM potassium phosphate buffer at pH 7.4 was used in each case).

### 3.2.1.3 Mechanism of photolysis of caged fumarate

Upon application of two consecutive laser flashes, a considerable proportion of the cage could be photolysed. The flash numbers and the excimer laser energy were optimised by subsequent experiments to ensure that the amount of released substrate was sufficient for binding-induced signals. The reaction represented in Figure 26 shows the photolysis mechanism of caged fumarate. Central to the photolysis mechanism is the formation of the *aci*-nitro intermediate (Barth *et al.*, 1995), (Barth *et al.*, 1997), (Gee *et al.*, 2002).

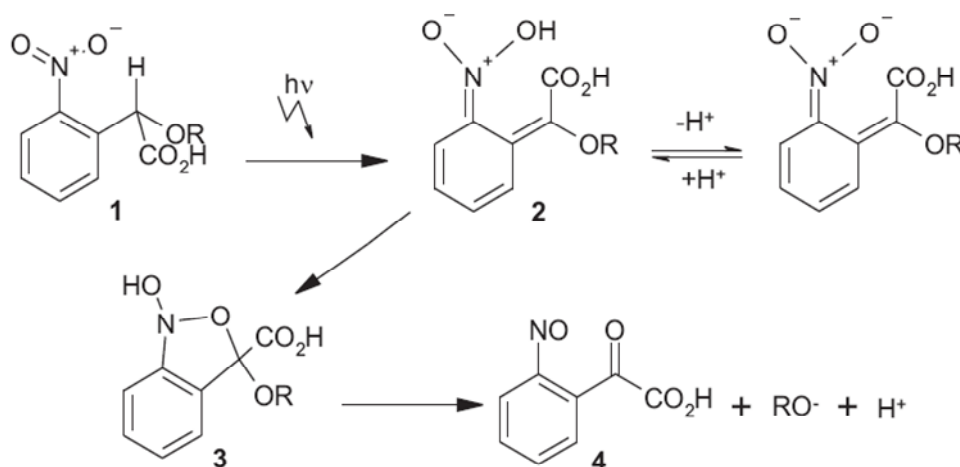


**Figure 26** Photolysis mechanism of CNB-caged compounds.

#### 3.2.1.4 Fumarate release only after laser flash:

The subsequent release of substrate (fumarate) is concomitant to the decay of the *aci*-nitro intermediate. Therefore the release rate of fumarate can be determined by measuring and following the absorbance transient of the *aci*-nitro form (Figure 24). The solid black baseline in Figure 28 represents the control spectra without any laser flash, signifying the fact that no cage dissociation and subsequent fumarate release occurs without the flash. The bold solid trace in Figure 28 shows the infrared difference spectrum of CNB caged fumarate generated by its photolysis, with the initial formation of the *aci*-nitro intermediate and eventually the formation of final products. Flash-induced difference spectra of CNB-caged fumarate exhibit characteristic and highly reproducible changes of IR absorbance. Negative bands in the difference spectra arises from photolytic groups that are modified during the process and positive bands are from groups formed upon photolysis in the *aci*-nitro intermediate or the final products (Barth *et al.*, 1995). In order to trace the decay of the intermediate, the temperature was essentially fixed at 5°C and the medium pH value was set to 7.4 using phosphate buffer. The FTIR difference band positions are summarised in Table 6. The nitro-group of the CNB compound is converted to a nitroso-group and a carboxylate side chain is generated together with the released substrate fumarate in the final product. Therefore, most prominent feature in caged fumarate dissociation is the conversion of the NO<sub>2</sub> group to a NO group upon photolysis of the cage leading to distinct band patterns in

difference spectra. This band pattern remains the same in both cases with or without the presence of QFR. Although detailed assignment of the *aci*-nitro intermediate was not possible within the limitation of experimental time scale, the negative marker band positions assigned at  $1529\text{ cm}^{-1}$  and  $1390\text{ cm}^{-1}$  arising immediately after the flash are assigned to the  $\text{NO}_2$  antisymmetric and symmetric stretching vibrations, respectively (Figure 28). The broad positive signal around  $1298\text{ cm}^{-1}$  is due to NO-stretching vibration. The immediate photolysis product 4 (see dissociation mechanism in Figure 26) leads to a relatively strong keto (C=O) mode contributing around  $1680\text{ cm}^{-1}$  (Görne-Tschelnokow *et al.*, 1992), (Walker *et al.*, 2002). Two other prominent bands at  $(+)$  $1557\text{ cm}^{-1}$  and  $(+)$  $1372\text{ cm}^{-1}$  correspond to C=O antisymmetric and symmetric vibrations, respectively. These two difference bands are in very good agreement with the characteristic band of fumaric acid (Figure 27).

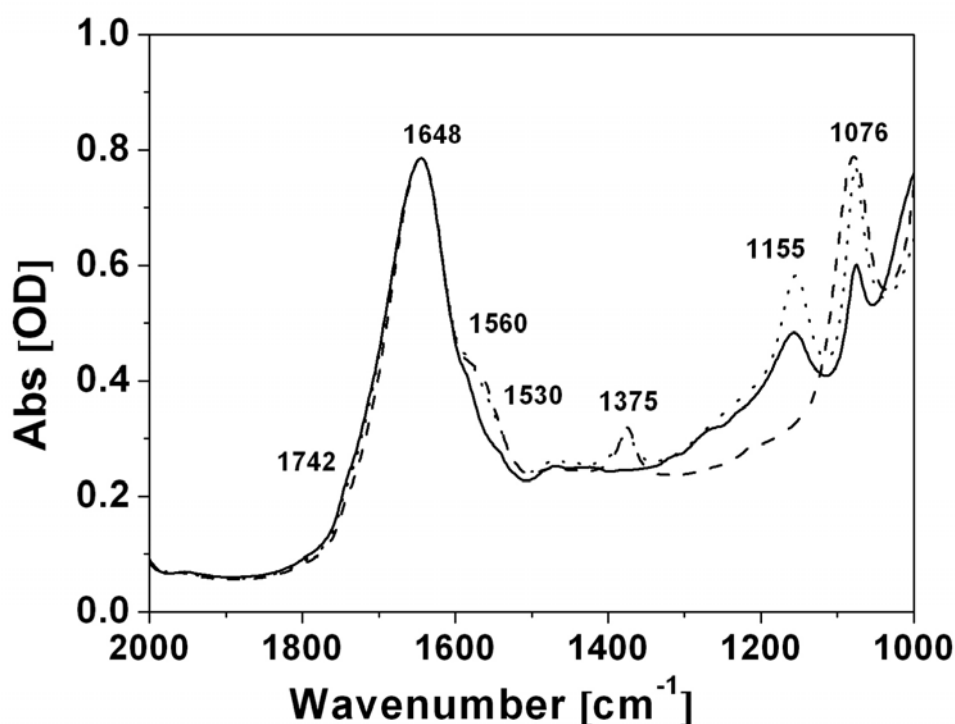


**Figure 27** IR absorption spectra of fumaric acid at pH 2 (solid line), pH 4 (dotted line) and pH 8 (dashed line). (20 mM fumaric acid concentration, 10  $\mu\text{m}$  IR pathlength, 5°C in 100 mM potassium phosphate buffer was used in each case).

Two negative bands at  $(-)$  $1307\text{ cm}^{-1}$  and  $(-)$  $1177\text{ cm}^{-1}$  are attributed to the ester C-O-C antisymmetric and symmetric vibrational modes of the *aci*-nitro intermediate,

respectively. In the region corresponding to  $\nu(\text{C}=\text{O})$  for esters and ketones, a strong negative peak is observed at  $1730\text{ cm}^{-1}$ . This is due to the diminishing effect of the C-O-R group (R=fumarate) from the cage to the end-products (Figure 26).

**Table 6** Summary of tentative IR band assignments (from  $1800\text{ cm}^{-1}$  to  $1000\text{ cm}^{-1}$ ) for CNB-fumarate dissociation.

wavenumber ( $\text{cm}^{-1}$ )	signal sign (+/-)	tentative assignments	references
1730	negative (-)	$\nu\text{C}=\text{O}$ (easter & ketone)	(Haas <i>et al.</i> , 2005)
1674	positive (+)	$\nu(\text{C}=\text{O})$	(Barth, 2000)
1529	negative (-)	$\text{NO}_2$ As	(Barth, 2000)
1390	negative (-)	$\text{NO}_2$ Sym	(Barth, 2000)
1354	negative (-)	$\nu(\text{NO}_2)$ Sym	(Barth, 2000)
1307	negative (-)	$\nu(\text{C}-\text{O}-\text{C})$ , Ester	(Barth, 2000)
1298	positive (+)	$\nu(\text{NO})$	(Barth, 2000)
1177	negative (-)	$\nu(\text{C}-\text{O}-\text{C})$ , Ester	(Barth, 2000)

**Table 7** Summary of tentative IR band assignments (from  $1800\text{ cm}^{-1}$  to  $1000\text{ cm}^{-1}$ ) for *W. succinogenes* QFR.

wavenumber ( $\text{cm}^{-1}$ )	signal sign (+/-)	tentative assignments	references
1730	negative (-)	Glu $\nu(\text{C}=\text{O})_{\text{ox}}$ ; $\nu\text{C}=\text{O}$ (easter & ketone)	(Haas <i>et al.</i> , 2005)
1721	negative (-)	Asp/Glu $\nu(\text{C}=\text{O})_{\text{red}}$	(Barth and Zscherp, 2002)
1692	positive (+)	Arg; $\nu_{\text{as}}(\text{CN}_3\text{H}_5^+)$ , heme prop.	(Chirgadze <i>et al.</i> , 1975), (Haas <i>et al.</i> , 2005)
1674	positive (+)	$\nu(\text{C}=\text{O})$ ; Asp/Glu $\nu(\text{C}=\text{O})$ ; Amide I; turns and $\beta$ -sheets	(Barth and Zscherp, 2002)
1650	positive (+)	Arg; $\nu_{\text{sym}}(\text{CN}_3\text{H}_5^+)$	(Chirgadze <i>et al.</i> , 1975), (Haas <i>et al.</i> , 2005)
1612	negative (-)	Gln $\delta(\text{NH}_2)$ ; Tyr-OH; $\nu(\text{CC})$ ; Tyr-O <sup>-</sup> , $\nu(\text{CC})$	(Barth and Zscherp, 2002), (Rahmelow <i>et al.</i> , 1998)
1598	negative (-)	Gln $\delta(\text{NH}_2)$ ; Tyr-OH; $\nu(\text{CC})$ ; Tyr-O <sup>-</sup> , $\nu(\text{CC})$	(Haas <i>et al.</i> , 2005), (Rahmelow <i>et al.</i> , 1998)
1558	positive (+)	heme prop.; Asp/Glu; $\nu_{\text{as}}(\text{COO}^-)$	(Haas <i>et al.</i> , 2005)
1462	positive (+)	heme porph; $\nu_{\text{sym}}(\text{C}_a\text{C}_m)$	(Haas <i>et al.</i> , 2005)
1426	positive (+)	Trp $\delta(\text{NH})$ , $i(\text{CC})$ , $\delta(\text{CH})$	(Haas <i>et al.</i> , 2005)
1410	positive (+)	Gln; $\nu(\text{CN})$ ; Trp; $\delta(\text{NH})$ , $\nu(\text{CC})$ , $\nu(\text{CH})$	(Barth and Zscherp, 2002), (Rahmelow <i>et al.</i> , 1998)
1404	positive (+)	Glu; $\nu_{\text{sym}}(\text{COO}^-)$	(Venjaminov and Kalnin, 1990a)
1402	positive (+)	Asp; $\nu_{\text{sym}}(\text{COO}^-)$	(Venjaminov and Kalnin, 1990a)
1372	positive (+)	heme prop.; Asp/Glu; $\nu_{\text{sym}}(\text{COO}^-)$	(Haas <i>et al.</i> , 2005)
1272	negative (-)	Trp; $\delta(\text{NH})$ , $\nu(\text{CN})$ , $\delta(\text{CH})$ Tyr-O; $\nu(\text{C}-\text{O})$ , $\nu(\text{CC})$	(Barth, 2000), (Chirgadze <i>et al.</i> , 1975)
1267	negative (-)	Tyr-O; $i(\text{C}-\text{O})$ and $i(\text{CC})$	(Haas <i>et al.</i> , 2005),

			(Rothschild, 1992)
1224	positive (+)	His; $\nu(\text{CN})$ , $\delta(\text{CH})$ , $\delta(\text{NH})$	(Barth and Zscherp, 2002)
1088	negative (-)	Trp; $\nu(\text{NC})$ , $\delta(\text{CH})$	(Barth and Zscherp, 2002), (Haas <i>et al.</i> , 2005)

Note: Multiple assignments are given for several vibrations, which represents possible alternatives or additional contributions at the same wavenumber. “ $\nu$ ” and “ $\delta$ ” symbol indicate stretching vibration and in-plane bending vibration, respectively. The subscripts “as” and “sym” indicate antisymmetric and symmetric vibrations, respectively. Heme propionates are abbreviated as “prop.” See text for references and details of the assignments.

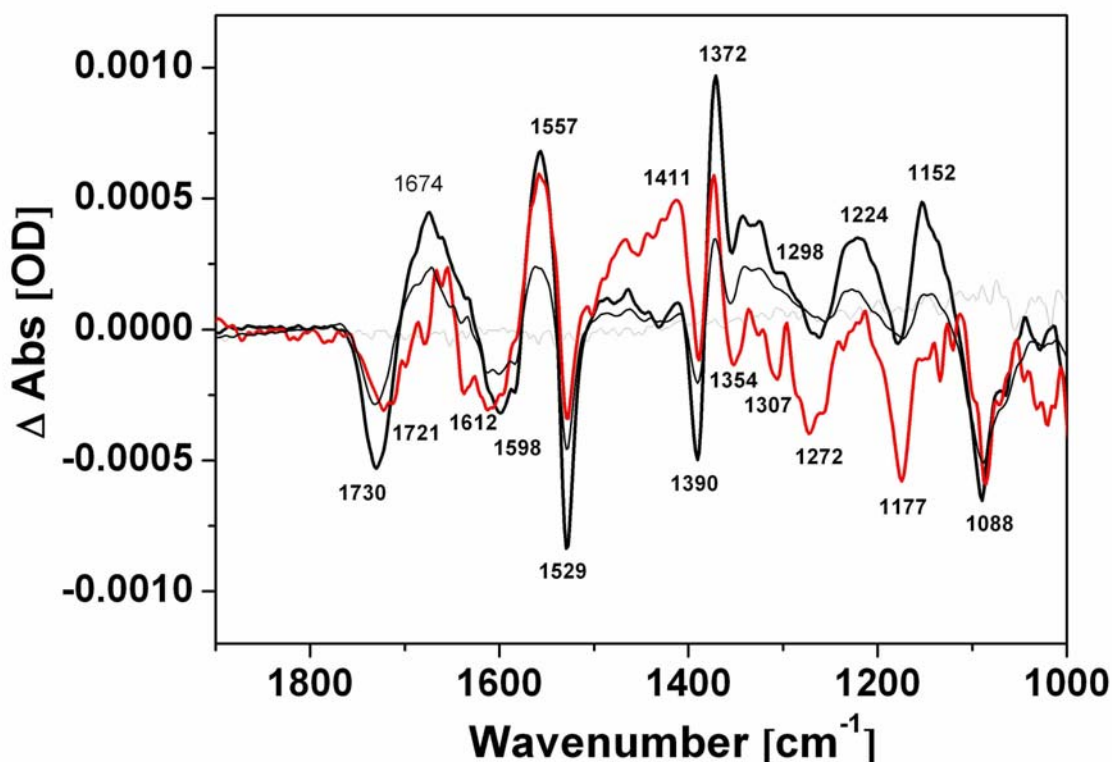


**Figure 28** Kinetic FTIR difference bands assignment in caged fumarate with and without the presence of QFR WT: difference spectra for photolysis of 30 mM Caged Fumarate (bold black line); 30 mM caged fumarate with 1 mM WT QFR oxidised (thin black line); 30 mM caged fumarate with 20 mM DMN( $\text{H}_2$ ) and 1 mM WT QFR reduced (red line) at pH 7.4, 5°C in 100 mM potassium phosphate buffer. In all cases 10 mM glutathione was used. The traces represent stationary difference spectra after two consecutive flashes. The grey line shows the baseline control spectra without any laser flash.



### 3.2.1.5 Release on a submillisecond time scale

Caged fumarate can be photolysed by a 308 nm laser flash from the XeCl laser as introduced earlier. Figure 26 shows the photolysis mechanism of the caged fumarate. As a positive control, the measurements are compared to CNB-glutamate. From the transient signal, the time constants of the decay of the *aci*-nitro intermediate are determined to 0.1 ms and 3 ms (Figure 26). The CNB-glutamate shows a similar behaviour with a double exponential time course (0.03 ms and 0.6 ms). For all the measurements the amplitude of the slow phase is not exceeding 33%. It is assumed that fumarate release is correlated to the fast phase of the relaxation process. From the analysis of the time course of the absorption transients, a release of fumarate after light triggering in the lower submillisecond time domain can be determined.

### 3.2.1.6 Initiation of enzymatic reaction by photolysis of caged fumarate

Caged fumarate is stable against hydrolysis under the conditions used in the enzymatic assay (50 mM K-phosphate or HEPES, pH 7.4). The ester-linkage between the fumarate and the CNB-group is not hydrolysed to a higher extent than 15% after 60 min. In the enzyme assay of QFR the oxidation of menaquinol is followed at 254 nm, a wavelength that is isosbestic to the unphotolysed/photolysed caged fumarate. The reaction is started by the addition of QFR-proteoliposomes. In the presence of unphotolysed caged fumarate a basal activity of the enzyme can be observed (Figure 24). A similar result is obtained in the absence of caged fumarate, but to a slightly lesser extent. However, most of the basal activity is assigned to residual fumarate from the enzyme preparation and oxygen that may be infiltrated during the addition of the QFR-proteoliposomes. The dependence of the enzymatic activity on the number of laser flashes that release the fumarate used for the turnover is a crucial factor to note. As an internal control fumarate is added at the end of the kinetic traces (Figure 24). It is inferred that the photolysis products inhibit the QFR only after a high number of flashes (500). Therefore the caged fumarate appears to be a suitable compound in kinetic studies of QFR.

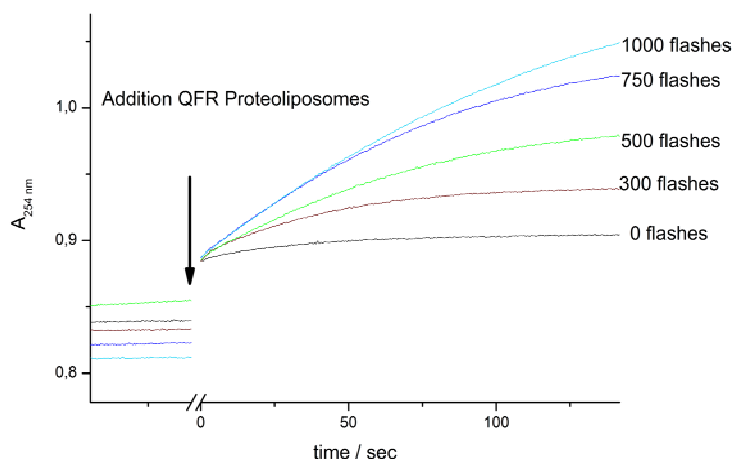


**Figure 29** Enzymatic activity of QFR. A 1 mM solution of caged fumarate was separately photolysed with a known area illuminated by laser flashes ( $17 \text{ mJ/cm}^2$ ) and afterwards added to the reaction sample. Conditions are 50 mM HEPES (pH 7.4), 80 mM dimethylmenaquinone, reduced with excess  $\text{KBH}_4$ , and 100 mM of caged fumarate after an increasing number of laser flashes. The sample was made anaerobic by flushing it with nitrogen in a sealed cuvette. After recording a stable baseline, the reaction was started by the addition of QFR-proteoliposomes.

### 3.2.1.7 pH dependence of photolysis reaction

Both the photolysis reaction and the enzymatic activity are pH dependent (Figure 30). For the decay of the *aci*-nitro intermediate, the relaxation rate of the fast process is decreasing with higher pH values, while the one of the slow process and the relative amplitudes of the two phases remain constant. For the QFR-activity, a maximum is seen at pH 7.4. This is a crucial feature in optimising kinetic measurements where both the amplitude of the signal and the release rate of fumarate have to be regarded.

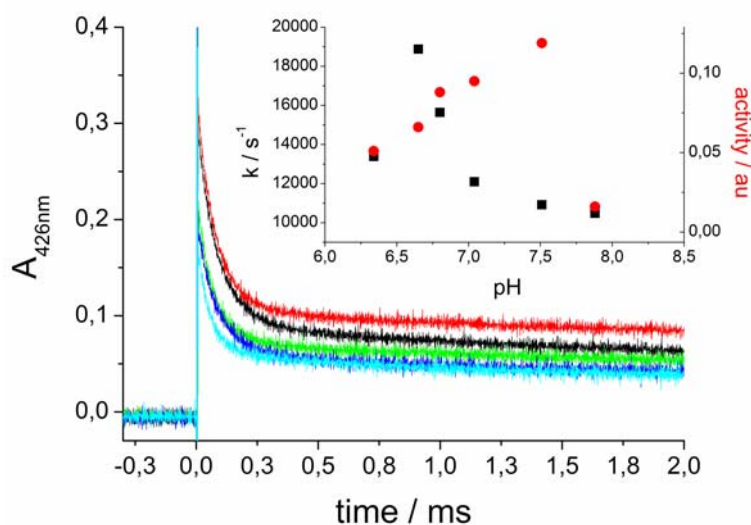


**Figure 30** Flash photolysis of caged fumarate at different pH values. Applied experimental conditions are same as in Figure 24. HEPES and BISTRIS are used as buffers in the selected pH range. Inset: Relaxation rates of the fumarate release and enzymatic activity (conditions as in Figure 24).

### 3.2.1.8 Estimation of percentage photorelease of caged fumarate per flash

Many photo-reactions proceed via a cascade of reactive intermediates and the release of the desired substrate may occur with considerable delay after excitation by a short laser pulse (Pelliccioli and Wirz, 2002). The substrate release rate and the efficiency may strongly depend on the solvent, pH and buffer concentration and thereby can initiate a proton transfer reaction (Pelliccioli and Wirz, 2002). Under physiological conditions, the knowledge of the actual release rate is an important prerequisite for studying biological response times and the rate can vary depending upon designing of protecting groups. The photolysis yield of substrate fumarate from its CNB-caged derivative was determined after quantification of the FTIR absorption difference band peak intensity per flash. 30 mM caged fumarate (in 100 mM potassium phosphate buffer) was irradiated with 308 nm monochromatic light from the XeCl laser within defined time intervals. Figure 31 shows the difference in IR absorption intensity monitored at  $1527 \text{ cm}^{-1}$  with increasing number of laser flashes. At a fixed cage concentration, the caged fumarate (only) shows higher amplitude of absorption differences compared to the cage with QFR sample (Figure 28). This hints to spectral shading of the cage generated by the QFR sample. The decay curves could be fitted in an exponential manner and the average percentage yield per laser flash is estimated to

be approximately 12% per flash. After 8-9 flashes, almost complete (~100%) cage occurred. This should not be misinterpreted as the exact quantum yield; rather it demonstrates that it is practically possible to release fumarate by approximately 12% from the caged fumarate under these conditions.

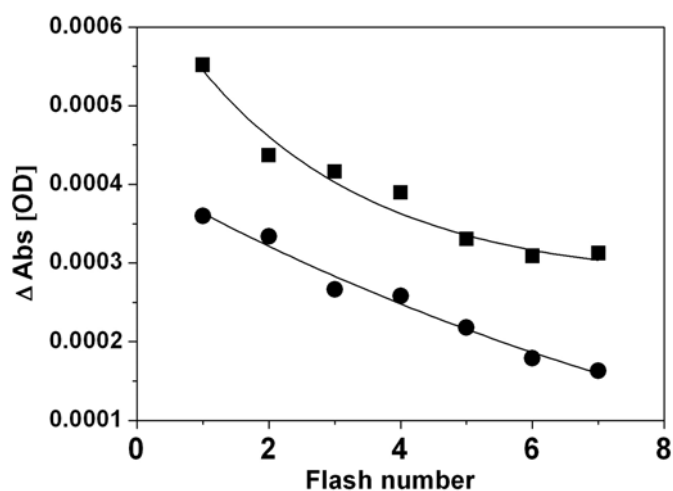


**Figure 31** Plot of exponential decay of IR difference spectral absorption intensity monitored at  $1527\text{ cm}^{-1}$ . (In circles, caged fumarate with WT QFR; in squares, cage fumarate only).

### 3.2.1.9 Interaction / binding of fumarate on WT QFR:

In many cases of enzymatic protein biomechanics, structural changes in the ligand-binding domain correlate to the functional consequences of enzymatic activity. ATR FTIR experiments were carried out in order to probe the nature of possible conformational changes in the ligand binding domain. The structural changes associated with docking of fumarate can be traced and thereby a detailed insight about the substrate binding can be investigated.

The FTIR difference spectra of substrate binding to QFR compared to the unbound state shows a characteristic pattern in the amide I region of the protein backbone absorbance (Figure 32 c). These differences can monitor conformational changes arising due to the fumarate binding. The band positions at  $(+)1706\text{ cm}^{-1}$  and  $(-)1589\text{ cm}^{-1}$  may indicate protonation of Glu. The FTIR difference spectra appearing at band positions of  $1655\text{-}1615\text{ cm}^{-1}$  region is of particular interest where  $\alpha$ -helix and  $\beta$ -sheets absorb. Bands around  $1654\text{ cm}^{-1}$  are usually assigned to  $\alpha$ -helical structures, while bands around  $1630\text{ cm}^{-1}$  are assigned to  $\beta$ -sheets (Nevskaya and Chirgadze,

---

1976). In the difference spectra (Figure 32 c), these two bands are with opposite signs; positive (+) and negative (-), suggesting that upon substrate binding  $\alpha$ -helical structural characteristics within the QFR tend to increase where as the  $\beta$ -sheet structural characteristics tend to decrease. Furthermore, a sharp negative difference band around  $1680\text{ cm}^{-1}$ , which is also characteristic of amide I turns and  $\beta$ -sheet structure in the oxidised state of the protein (Haas *et al.*, 2005), confirms diminishing of turns and  $\beta$ -sheet structural parts.

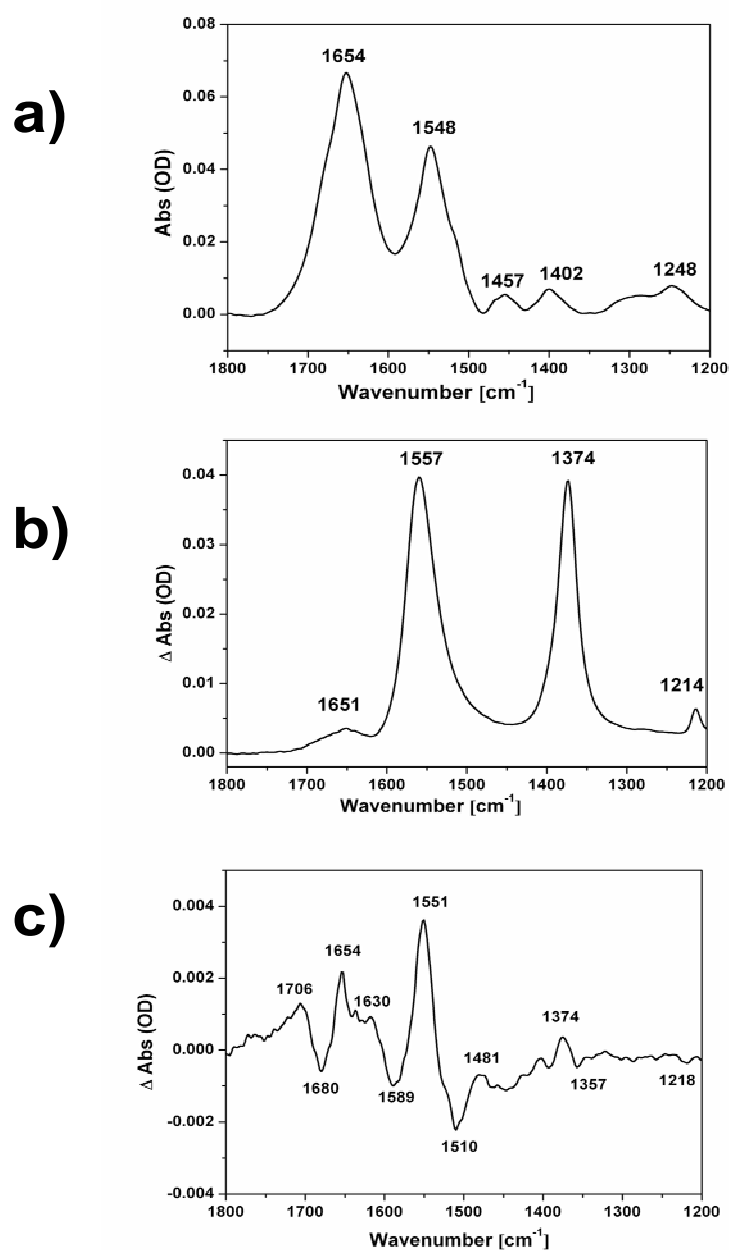


**Figure 32** Binding of fumarate with QFR WT (in 50 mM phosphate buffer at pH 7.4) by ATR FTIR method: a) Spectrum of QFR with 50 mM fumaric acid; b) Absorption spectrum of buffer with 50 mM fumaric acid minus buffer without fumaric acid; c) Difference spectrum of QFR with 50 mM fumaric acid minus QFR without fumaric acid.

Fumaric acid has its two major characteristic infrared absorption bands at 1560 and 1374 cm<sup>-1</sup> (Figure 32 b) Although the difference bands are closely positioned (Figure 32 c), the (+)1551 cm<sup>-1</sup> band possibly does not arise due from fumarate absorption. The original absorption band of fumaric acid positioned at 1557 cm<sup>-1</sup> (Figure 32 b) a

comparatively much broader band. Therefore, it can be concluded that the  $1551\text{ cm}^{-1}$  band in the difference spectra corresponds to changes in the amide I region. In fact, the  $1551\text{ cm}^{-1}$  band is typical for helix absorption (Goormaghtigh *et al.*, 1994). Difference bands at  $(-)$  $1510\text{ cm}^{-1}$  and  $(+)$  $1481\text{ cm}^{-1}$  could arise due to the change in properties of Tyr or/and Trp side chains and may involve the FAD (Haas *et al.*, 2005). Furthermore, difference bands at  $(+)$  $1374\text{ cm}^{-1}$  and  $(-)$  $1357\text{ cm}^{-1}$  indicate possible changes in properties of Trp. However, contribution of small artefacts of subtraction of fumaric acid spectra appearing at around  $(+)$  $1374\text{ cm}^{-1}$  can not be ruled out. The band at  $(-)$  $1218\text{ cm}^{-1}$  changes in properties of His upon binding of fumarate. The negative band at  $(-)$  $1680\text{ cm}^{-1}$  arises probably due to alterations in turns and the  $(+)$  $1654\text{ cm}^{-1}$  band due to absorbance of helix and /or disordered structure, as mentioned earlier. However, it is not possible to distinguish between these two structures by measuring only in buffer containing  $\text{H}_2\text{O}$ . The difference band at  $(+)$  $1630\text{ cm}^{-1}$  indicates absorbance of  $\beta$ - or extended structure. Overall, possible explanation could be that secondary structure changes occur from turns to helix/disordered and extended structural elements upon fumarate binding to QFR.

#### 3.2.1.10 Comparison of FTIR difference spectra of caged fumarate with/without WT QFR

FTIR difference spectra of caged fumarate with WT QFR shows specific differences from that of the cage (only) spectra within a time window of  $\sim 200$  milliseconds after the release (data not shown). Minor conformational changes can be concluded from the amplitude (and intensity) of the difference bands. The FTIR difference band positions are summarised in Table 7. The  $1674\text{ cm}^{-1}$  band (spectrum of only cage; Figure 28, bold solid line) corresponds to the C=O stretching vibration together with a possible contribution from C=C stretching vibrations in fumarate (Figure 28). Of special interest is the absorbance of the amide I mode of the polypeptide backbone, which is sensitive to secondary structure. An overall conformational change in the polypeptide backbone is evident from the broad characteristic of FTIR difference signals in the  $(+)$  $1650\text{ cm}^{-1}$  region. The  $(-)$  $1730\text{ cm}^{-1}$  band is shifted to  $(-)$  $1721\text{ cm}^{-1}$  when the cage is present with QFR and the negative effect is somehow hindered with the contradicting effect generated by possible protonation of the Glu/Asp side chains. With a clear effect of the

shifted negative peak at  $(-)$ 1721  $\text{cm}^{-1}$ , a band appears at  $(+)$ 1411  $\text{cm}^{-1}$  (Figure 28, red line) in the difference spectra; the later being ascribed to deprotonated carboxylate (McMahon *et al.*, 2004). The overall scenario indicates that fumarate binding has a specific effect on the QFR backbone structure.

Symmetric and antisymmetric vibrational frequencies of arginine residues at 1650  $\text{cm}^{-1}$  and 1692  $\text{cm}^{-1}$ , respectively (Barth and Zscherp, 2002) may be subdued in the broad overlapping positive difference signals. Reactions at fumarate reaction site may involve the Arg A301 and Arg A404 (Lancaster *et al.*, 2001). Redox difference spectra originating due to protonation/deprotonation (reduced and oxidised form, respectively) of arginine residue is although very unlikely. This is probably due to the fact that a deprotonation reaction of Arg (having a pK of  $\sim$ 11) is not feasible. Non-definitive indications of involvement of protonation of arginines have been reported in FTIR studies of internal proton transfer reactions linked to inter-heme electron transfer in bovine cytochrome *c* oxidase (McMahon *et al.*, 2004) which are special in case of COX.

One of the obvious observations regarding caged fumarate dissociation in presence of QFR is the spectral shading effect. The two heme *b* groups in QFR render the sample to be highly reddish-brown in colour at a substantial protein concentration of  $\sim$ 1mM. This high absorbance characteristic of QFR can shade the caged fumarate to catch sufficient flash energy, thereby lowering the amount of released fumarate for flash efficiency to be lower. Spectral trace from the cage (only) has almost double intensity of absorption difference signals compared to that when QFR is present with the cage, the sample layer thickness and the other experimental conditions being identical (Figure 28).

#### 3.2.1.11 *Time-dependent evolution of FTIR difference spectra of caged fumarate with WT QFR*

Significant differences in the spectral positions of specific absorbance bands have been observed between the kinetic difference traces of caged fumarate in the absence and presence of QFR (Figure 33). The IR difference spectra in specific amino acids may vary with a time dependent manner that could hint that specific amino acid side chain are involved in the protein's molecular reaction mechanisms. Changes at protonable and other residues that are sensitive to the electron distribution in the enzyme are



obvious in the FTIR difference spectra as discussed later. The first difference spectrum after 65 ms time window depicts spectral differences when every binding reaction should have taken place. Difference spectra recorded after this time window represent similar characteristics in band positions and band signs (positive or negative) as the first spectrum with some subtle changes related to sample integrity and stability. Although the current stage of the results does not allow us to interpret and represent a complete molecular description for the difference spectra, the FTIR difference bands (Figure 33) can indicate the following outcomes that are crucial to understand the binding of fumarate to the QFR.

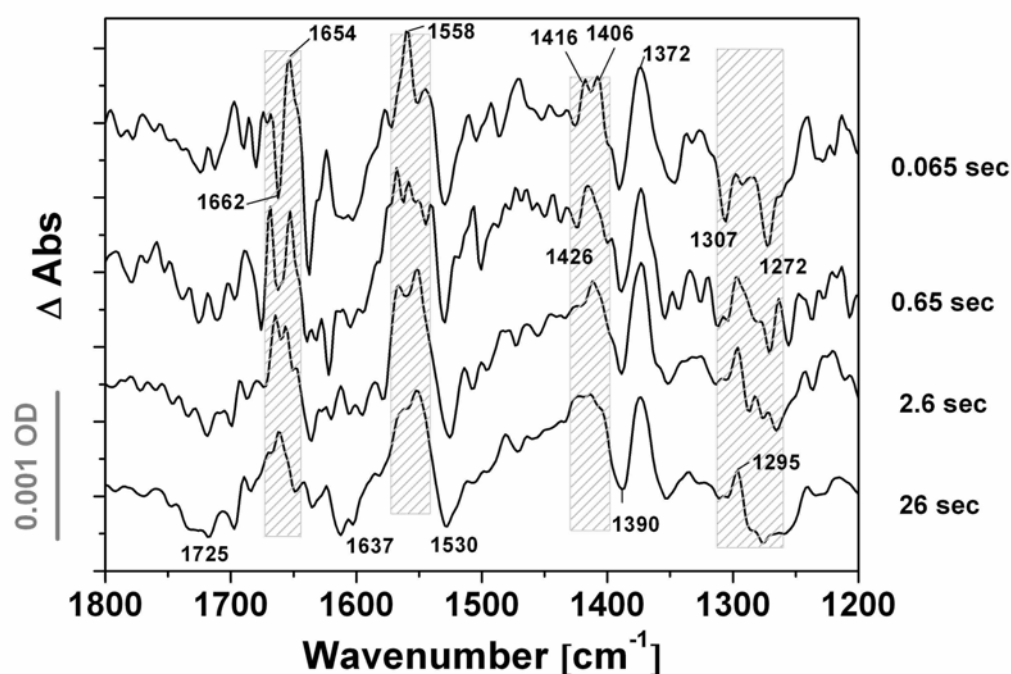


**Figure 33** Time dependence of FTIR difference spectra for photolysis of 50 mM caged fumarate with 1 mM WT QFR (solid line) in presence of DMN(H<sub>2</sub>) and glutathione at pH 7.4, 5 °C in 100 mM potassium phosphate buffer. The traces represent spectra averaged in 65 ms, 0.65 sec, 2.6 sec, and 26 sec time window after two consecutive flashes each with 23 kV energy per flash. The specific shaded areas in the kinetic difference traces indicate the wavenumber regions with major spectral changes as a function of time.

(1) The initial 0.65 second spectral characteristic around 1650-1680 cm<sup>-1</sup> region resembles the spectral characteristic of the reduced-minus-oxidized spectra of QFR obtained previously by electrochemically induced FTIR difference spectroscopy (Haas

*et al.*, 2005). This may hint that with subsequent reduction of hemes in QFR, a rapid release and binding of fumarate in the presence of the menaquinol analog can actually start the catalytic cycle of QFR. However the heme reduction was difficult to monitor by the respective IR absorption bands due to the relatively low intensity of the porphyrin ring signal and also the fact that signals arising from heme porphyrin ring vibration appear in rather low-IR range (below  $1000\text{ cm}^{-1}$ ). Changes in the  $1678\text{ cm}^{-1}$  (ox) region in case of QFR may correspond to alteration in secondary structure elements such as amide I turns and  $\beta$ -sheet. Two distinct peaks are positioned at  $1654\text{ cm}^{-1}$  and  $1662\text{ cm}^{-1}$  regions. Up to 2.6 sec duration after the release of the substrate, the (+) $1654\text{ cm}^{-1}$  and (-) $1662\text{ cm}^{-1}$  peaks are very prominent and decays gradually with the appearance of a single broad band around (+) $1662\text{ cm}^{-1}$  spectral region for a relatively longer time duration (during the concomitant 26 sec). The appearance of the (+) $1654\text{ cm}^{-1}$  band (which could correspond to an Asn  $\nu(\text{C}=\text{O})$  stretching) suggest the possible protonation of an Asn residue (Chirgadze *et al.*, 1975), (Rahmelow *et al.*, 1998), (Venyaminov and Kalnin, 1990a), (Venyaminov and Kalnin, 1990b). The peak positioned at  $1660\text{-}1662\text{ cm}^{-1}$  may correspond to reduced Gln.

(2) A slight shift of the signal at (+) $1558\text{ cm}^{-1}$  to a lower wavenumber is observed with increasing time (Figure 33). At a relatively larger time delay, the  $1558\text{ cm}^{-1}$  peak eventually shifts to  $1552\text{ cm}^{-1}$ . The  $1558\text{ cm}^{-1}$  peak position can be assigned to several important groups, namely, the heme propionate and the  $\nu_{\text{as}}(\text{COO}^-)$  of Asp/Glu residues. A possible explanation for that can be the following. As an important environmental factor, the hydrogen bonding related to these two particular acidic residues (upon protonation) lowers the frequency of stretching vibration. Analogous results of H-bonding induced shift have been previously characterized and reported for His and Tyr residues of photosystem II (Hienerwadel *et al.*, 1997), (Noguchi *et al.*, 1999) and bacteriorhodopsin (Dollinger *et al.*, 1986), (Roepe *et al.*, 2002), (Rothschild, 1992).

(3) The spectral feature around  $1420\text{-}1405\text{ cm}^{-1}$  consists of two distinct band peaks at the initial time block (0.065 sec), showing decreased band intensity and a spectral broadening. The small band around (+) $1462\text{ cm}^{-1}$  in the initial time block is probably due to the heme porphyrin ring  $\nu_{\text{s}}(\text{C}_a\text{C}_m)$  signal. The (+) $1416\text{ cm}^{-1}$  band may arise as a result

of reduced Trp  $\delta(\text{NH})$ ,  $\nu(\text{CC})$ ,  $\delta(\text{CH})$  vibrational modes. A reduced Gln  $\nu(\text{CN})$  vibrational mode could be proposed based on the (+)1410  $\text{cm}^{-1}$  band. However, the reduction of these two amino acid chains is transitory and rapid enough. On a relatively longer time scale, the broad spectral peak covers the spectral region of 1400-1410  $\text{cm}^{-1}$ , which in turns reflects possible involvement of Glu and Asp (both assigned to  $\nu_s(\text{COO}^-)$  vibration) in their reduced state. From earlier studies of Venyaminov and Kalnin (Venyaminov and Kalnin, 1990a), it has been established that Glu and Asp bands could be assigned to 1404  $\text{cm}^{-1}$  and 1402  $\text{cm}^{-1}$ , respectively. However these band positions may shift +60/-90  $\text{cm}^{-1}$  upon cation chelation (Tackett, 1989) and in extreme cases the band position for  $\nu(\text{C-O})$  of COOH group may alter (Barth and Zscherp, 2000), (Deacon and Phillips, 1980).

(4) A prominent band peak at (-)1272  $\text{cm}^{-1}$  appears in the difference spectra and with time this peak shifts slightly to a lower wavenumber region, around 1267  $\text{cm}^{-1}$ . This band at 1272  $\text{cm}^{-1}$  has been assigned to the oxidized state in Tyr-O<sup>-</sup>,  $\nu(\text{C-O})$  and  $\nu(\text{CC})$  vibrations (Dollinger *et al.*, 1986), (Hienerwadel *et al.*, 1997). A smaller wavenumber shift in band position may occur as the Tyr band is sensitive to H-bonding.

### **3.2.2 Caged 2-Methyl-3-methylamino-1,4-naphthoquinone(ol) (MMAN(H<sub>2</sub>))**

#### *3.2.2.1 UV-VIS absorption spectra of caged-MMAN*

The UV-VIS absorption spectrum of caged-MMAN is shown in Figure 34.

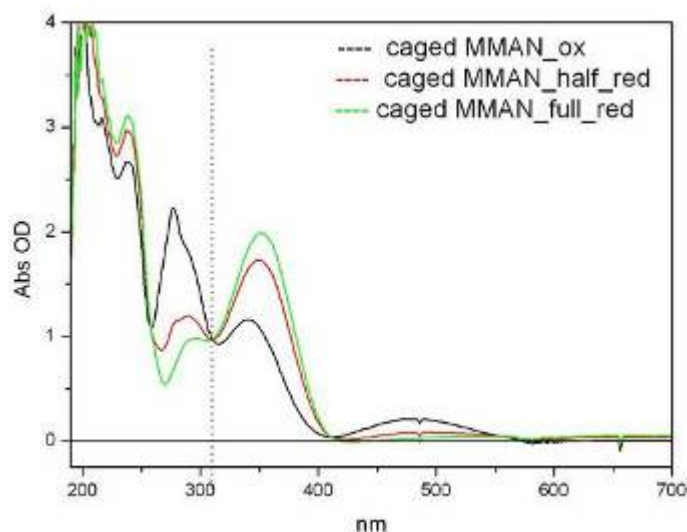


**Figure 34** Absorption spectra of caged-MMAN in 100 mM Na-phosphate buffer of pH 7.4. (Black: caged-MMAN in its fully oxidised state, red: caged-MMAN in its half-reduced state, green: caged-MMAN in its fully reduced state); the dashed line points out the 308 nm wavelength where the laser flash was applied during flash-induced FTIR studies.

UV-visible absorption spectra of oxidised and reduced solution of quinone have been studied extensively in many earlier studies (Bauscher and Mäntele, 1992), (Breton, 1997), (Hellwig *et al.*, 1999). The two positive bands at around 240 nm and 270 nm region are due to the  $\pi \rightarrow \pi^*$  transition in the Q species. There is another significant band peak at 380 nm arising due to the  $n \rightarrow \pi^*$  transition (Meganathan and Coffell, 1985). The quinone solution in the experimental compartment can be reduced with  $\text{KBH}_4$  and hence the resulting spectra can be recorded with negative peak maxima at around 280 nm. Electron transfer reaction in quinone species occurs in a two step mechanism, first generating  $\text{Q}^-$  and then  $\text{Q}^{2-}$  with the respective incorporation of two successive electrons. In kinetic studies of quinone containing enzymes the absorbance difference  $A_{280} - A_{320}$  was monitored as a function of time (Madej *et al.*, 2006a). With an addition of a calculated amount of borohydride it could be ideally possible to obtain the spectra of the half reduced species. However, from the spectral feature it can not be speculated whether the singly reduced species is either  $\text{MMAN}^-$  or  $\text{MMANH}$  and whether the doubly reduced species is either  $\text{MMANH}^-$  or  $\text{MMANH}_2$ . A diode-array UV/VIS spectrophotometer (Agilent 4853) was used for recording different wavelengths simultaneously. Therefore, no further scaling was needed (Madej *et al.*, 2006a).

### 3.2.2.2 FTIR absorption spectra of MMAN and caged-MMAN

Figure 35 depicts the FTIR absorption spectra of the MMAN and caged-MMAN.

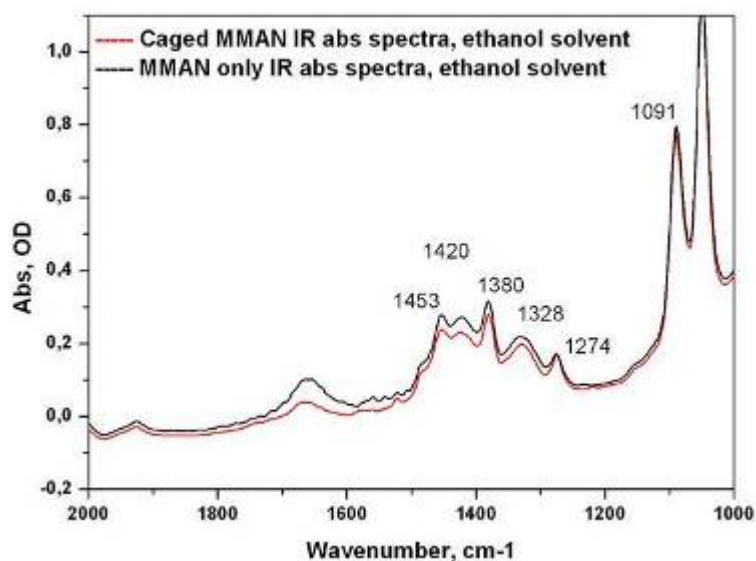


**Figure 35** FTIR absorption spectra of the MMAN and caged-MMAN.

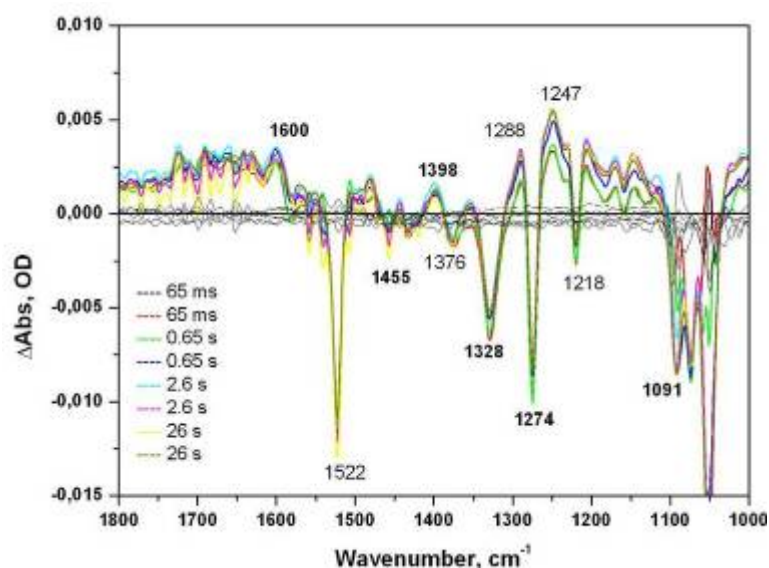
The infrared absorption spectra of MMAN and caged-MMAN do not significantly differ. Only specific and minor differences arise in case of the cage due to the presence of the caging moiety. The  $1453\text{ cm}^{-1}$  band is representative of the  $\text{CH}_2$  deformation in the linker position. The  $1420\text{ cm}^{-1}$  and a prominent  $1380\text{ cm}^{-1}$  band are representative of  $\text{CH}_3$  deformation of the aromatic methyl group and/or in-plane O-H bending, respectively. The  $1328\text{ cm}^{-1}$  and  $1274\text{ cm}^{-1}$  bands arise from the tertiary amine vibrations (C-N stretching). The  $1328\text{ cm}^{-1}$  band may also be contributed from the  $\text{NO}_2$  symmetrical stretching vibration.  $1091\text{ cm}^{-1}$  band generally appears due to the presence of phosphate group in the medium buffer (P=O stretching).  $1040\text{ cm}^{-1}$  band possibly arise due to the  $\text{CH}_3\text{-O}$  stretching (As saturated C-O stretching appears in  $1050\text{-}1010\text{ cm}^{-1}$  range). A less intense signal at  $1660\text{ cm}^{-1}$  might originate from the C=O group from quinone in solution (Bauscher and Mäntele, 1992). An overall conclusion can be that these assigned characteristic absorption bands are particular to the caged substrate containing corresponding functional groups. The FTIR difference band positions here discussed are summarised in Table 8.

**Table 8** Summary of tentative IR band assignments (from 1800  $\text{cm}^{-1}$  to 1000  $\text{cm}^{-1}$ ) for caged MMAN( $\text{H}_2$ ) dissociation.

wavenumber ( $\text{cm}^{-1}$ )	signal sign (+/-)	tentative assignments	references
1600	positive (+)	secondary amine, C-N str., C-N-C sym.str.	this thesis
1522	negative (-)	$\text{NO}_2$ antisym. str.	this thesis
1455	negative (-)	$\text{CH}_2$ deformation	this thesis
1398	positive (+)	$\text{CH}_3$ deformation	this thesis
1376	negative (-)	$\text{NO}_2$ sym. str.	this thesis
1328	negative (-)	tertiary amine, C-N str., $\text{NO}_2$ sym.str.	this thesis
1288	positive (+)	C-O- $\text{CH}_3$	(Mezzetti <i>et al.</i> , 2003)
1274	negative (-)	tertiary amine, C-N str.,	this thesis
1247	positive (+)	aromatic C-O str. this manuscript	this thesis
1218	negative (-)	C-N str.	this thesis
1091	negative (-)	phosphate buffer; P=O	(Haas <i>et al.</i> , 2005)

### 3.2.2.3 FTIR analysis of the caged MMAN( $\text{H}_2$ ) dissociation

The vibrational difference spectra before and after the flash is reported in Figure 36. The different colour codes represents difference spectra calculated from respective spectra acquired at distance time intervals after triggering release of the caged substrate minus the spectrum acquired before applying the flash to the caged sample. Flash-induced difference spectra exhibit characteristic and highly reproducible changes of IR absorbance. In the difference spectra, several positive (+) and negative (-) difference bands arise at specific wavenumbers.

**Figure 36** Characterisation of FTIR bands after caged MMAN photolysis.

Negative bands in the difference spectra arise from photolytic groups that are modified during the process and positive bands arise from groups that are formed upon photolysis of the cage (or the final products) (Barth *et al.*, 1995). The experimental temperature was essentially fixed at 5 °C and the medium pH was set at 7.4 using phosphate buffer. The FTIR difference band positions are summarised in Table 8. Positive and negative natures of these bands and the band positions are in accordance as expected from literature (see also Figure 35). The caged MMAN(H<sub>2</sub>) was dissolved and stored in ethanol solvent in the dark. Here with the caged MMAN(H<sub>2</sub>) it was possible to record the spectrum instantly after the laser flash up to the first 65 ms. Reaction could be monitored in a time dependent manner up to an order of several minutes.

Concomitant with the spectral changes observed is the formation of the desired menaquinol analog substrate and the expected dimethoxy nitrophenyl caging moiety (Figure 13). During the flash photolysis, the tertiary amine (3° amine) group in the cage is eventually converts to a secondary amine (3° amine) and the CH<sub>2</sub> group (linked to the tertiary amine nitrogen) converts to a CH<sub>3</sub> group. Therefore, the positive (+) FTIR difference bands at 1600 cm<sup>-1</sup> and 1398 cm<sup>-1</sup> are characteristics of the secondary amine and CH<sub>3</sub> deformational vibrations (see Table 8). The negative (-) FTIR difference band positions represent the disappearance of the tertiary amine (1328 cm<sup>-1</sup> & 1274 cm<sup>-1</sup>), the CH<sub>2</sub> group (1455 cm<sup>-1</sup>) and the C-N bond (1218 cm<sup>-1</sup>) (see Table 8). The background control measurement before every trace shows no detectable signal (Figure 36). Taken together, these FTIR difference bands characteristically represent the cage dissociation, and the subsequent release of quinol analog. However, the dissociation phenomenon is fast enough and almost instantaneous to detect susceptible changes within the limited lime resolution of the system. These specific difference bands are also in accordance with the cage IR absorption spectra (Figure 35) in their respective wave number positions.

#### 3.2.2.4 FTIR absorption difference spectra of caged-MMAN with QFR

The FTIR difference spectrum of the released quinol analog and fumarate in presence of QFR is shown in Figure 37.

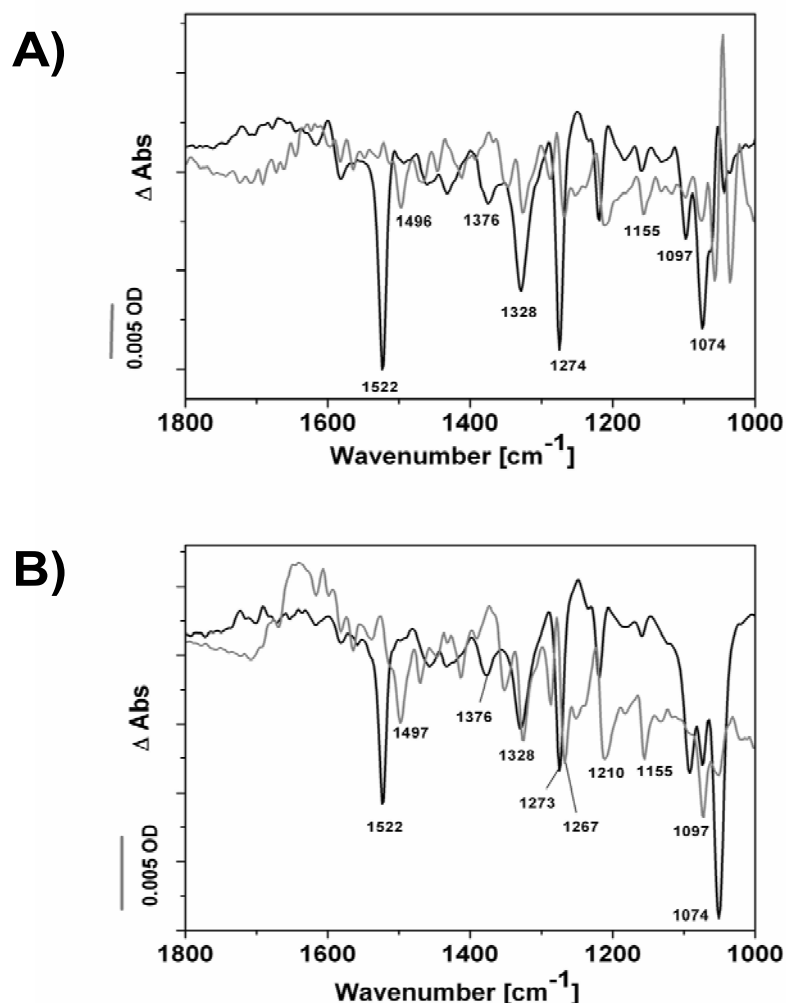


**Figure 37** Kinetic FTIR difference bands assignment in caged MMAN with and without the presence of QFR WT: (in black trace) 100 mM caged MMAN only; (in grey trace) 100 mM caged MMAN with 0.5 mM QFR WT, 30 mM caged fumarate; a): spectra of 65 nm after the flash, b): spectra of 26 sec after the flash.

Few aspects of caged-MMAN results partially resemble the spectral features of the redox-induced (reduced-minus-oxidised) QFR WT data. Small changes in the difference spectra around  $1650\text{ cm}^{-1}$  suggests that changes in the protein amide I modes are likely to take place. One of the most obvious observations is that the  $1523\text{ cm}^{-1}$  marker band (relevant to  $\text{NO}_2$  antisymmetric stretching) in the MMAN spectra shifts its band position to  $1499\text{ cm}^{-1}$ , indicating possible reduction of the nitro group in the cage moiety. The negative peaks in the difference spectra (gray trace in Figure 37) at positions  $(-)\text{1498 cm}^{-1}$  and  $(-)\text{1468 cm}^{-1}$  possibly hints the protonation of tyrosine and heme porphyrin in QFR, respectively. In case of *Rb. sphaeroides* the frequency of the C-O stretch of the



UQ<sub>0</sub> semiquinone anion *in situ* has been found to be around 1500 cm<sup>-1</sup> which is close to *in vitro* values in methanol (Breton *et al.*, 1991). This suggests established polar character of the Q<sub>B</sub> pocket and the H-bonding of the two quinonic oxygens with amino acid residues (Deisenhofer and Michel, 1989). A more detailed analysis of the position of the 1460-1400 cm<sup>-1</sup> semiquinone anion band would require spectroelectrochemistry of quinone in various solvents and a better knowledge of the other factors, such as the distortion from a planar conformation of the quinone ring and C=O groups or the influence of the polarity of the microenvironment, which contribute to the energy of this vibration. One of the remarkable observations is appearance of a negative band at (-)1376 cm<sup>-1</sup> which suggests the possible protonation of Asp and/or Glu residues (Figure 37). The negative band at (-)1326 cm<sup>-1</sup> (previously detected in the cage only spectra at (-)1328 cm<sup>-1</sup>) is unchanged in both the cases and represents the disappearance of the tertiary amine group in caged MMAN dissociation (Figure 37). The similar phenomenon of disappearance of tertiary amine together with a possible protonation of tryptophan and tyrosine residues (Table 7) leads to a band shift of 1273 cm<sup>-1</sup> band to a new position at 1267 cm<sup>-1</sup> in the QFR bound state of the released substrate (Figure 37 B). Overall, the different state of ionization and/or protonation is expected to shed light on the geometrical and energetic factors (hydrogen bonding, dipolar interactions), distortion of the ring and substituents, microconformational changes, and electrostatic relaxation of QFR. With the evolution of time, there are no remarkable changes in the band positions and patterns of the two spectra represented in Figure 37 (A & B), suggesting that the release of the caged substrate and its subsequent binding to the enzyme is relatively faster enough to detect any kind of events such as further protonation/conformational changes, even after hundreds of millisecond of its release.

### 3.3 Transient absorption spectroscopy

Towards an understanding of the catalytic mechanism of this enzyme, the aim of the present work was to investigate the processes associated with inter-heme electron transfer in QFR. In this present study, picosecond transient absorption spectroscopy has been employed to resolve the actual time-scale of the inter-heme electron transfer. Previous studies by Champion and co-workers (Wang *et al.*, 2000), (Zhu *et al.*, 1994)

involved coherent reaction of the heme upon impulsive excitation of cytochrome *c* (Vos and Martin, 1999) using excitation and probing in the Soret band region.

### 3.3.1 Steady state absorption study of WT QFR

The heme Soret band absorption maximum shifts from 416 nm (oxidised, shown in black) to 428 nm (reduced, shown in red). The reduced spectrum (in green) was taken after 8 hours of continuous illumination of the QFR sample (Figure 38). Reduced-minus-oxidised difference spectra of WT QFR show the largest contribution in the Soret region, whereas the contribution from the  $\alpha$ -region is  $\sim 10\%$  of the total absorption change in Soret band. Similarly, the sample was semi-reduced using DMNH<sub>2</sub> (2, 3-dimethyl-1, 4-naphthoquinol) as it has the midpoint potential which is well in between the two heme midpoint potential values. Therefore, DMNH<sub>2</sub> ( $E_m = -75$  mV) specifically reduces the high potential heme  $b_P$  ( $E_m = -9$  mV) and the low potential heme  $b_D$  ( $E_m = -152$  mV) still remains in its oxidised state. The QFR sample then finally ends up in a mixed-valance state. The calibration and optimisation of the exact amount for DMN (2, 3-dimethyl-1, 4-naphthoquinone) and DMNH<sub>2</sub> needed for a certain amount of QFR was calculated previously (data not shown). Chemical reductions of QFR were performed under anaerobic conditions. In (Madej *et al.*, 2006a), UV/VIS spectra of oxidised and reduced quinones and an *in situ* redox titration of DMN has been shown. Followed by the single heme reduction, reduction of both the hemes occurred during overnight excitation (Figure 38).

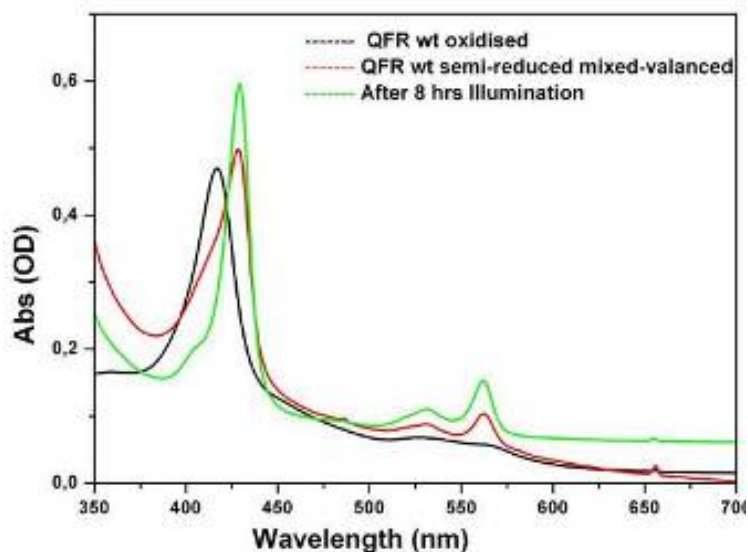


**Figure 38** Absorption spectra of QFR WT at pH 7.4 in two different redox states. The heme Soret band absorption maximum shifted from 416 nm (oxidised, shown in black) to 428 nm (reduced, shown in red and green). In red, shown is the QFR WT “mixed-valance” state and in green shown the double heme reduction after 8 hours of illumination in visible light.

### 3.3.2 Cryo temperature static VIS redox difference spectra of WT QFR

Absorption spectra of various oxidation states of WT QFR preparations were measured in the visible region over a wide range of temperatures from  $-185^{\circ}\text{C}$  (88K) to room temperature (300K), employing a liquid nitrogen cryostat system. A carbon resistor was used, the resistance of which shows the temperature dependence as a semiconductor and as a function of inverse absolute temperature. The sample preparations of WT QFR oxidised state (Figure 41) and WT QFR dithionite reduced state (Figure 39) were used respectively. The general features from low temperature spectra were the following. First of all, there was a sharpening of each peak in the spectra of the reduced hemes, especially in  $\alpha$ - peak (Figure 39) with gradual lowering of the temperature.

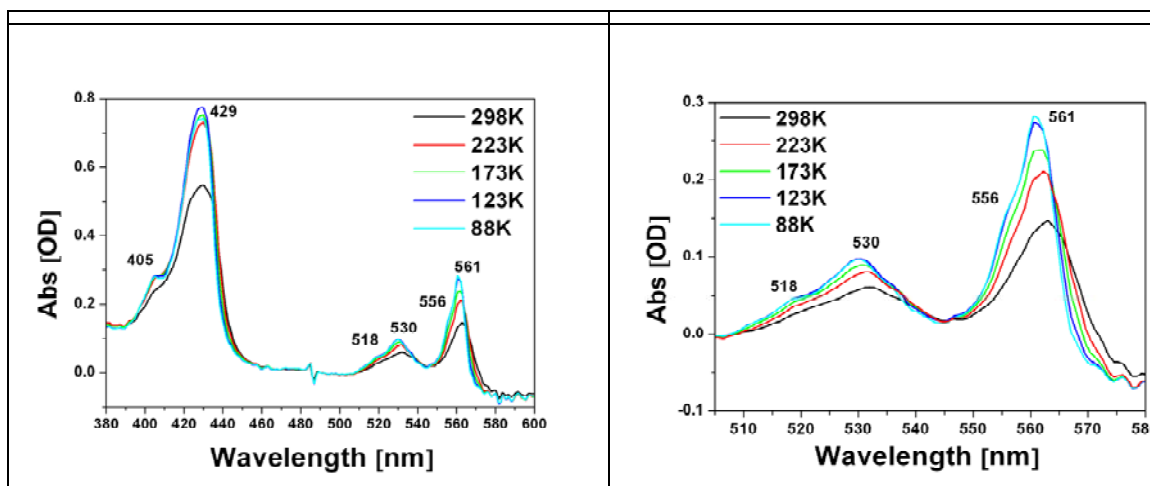


**Figure 39** Changes in absorption spectra of fully reduced QFR measured at a temperature range from 298K to 88K. Spectra in the left side is the zoomed version ( $\alpha$ - and  $\beta$ - bands are enlarged) of the full spectra in the left side (Experimental conditions and other details are mentioned in the materials and methods part).

The sharpening effect is thought to be induced by the restriction of molecular oscillation at low temperatures. In addition, there was a tendency of the  $\alpha$ - band peak to separate into two distinct peaks ( $\alpha_1$  and  $\alpha_2$ ) at low temperatures. The same kind of spectral features also appeared in case of the  $\beta$ - band. The maximum absorbance was plotted versus the wavelength (Figure 40).

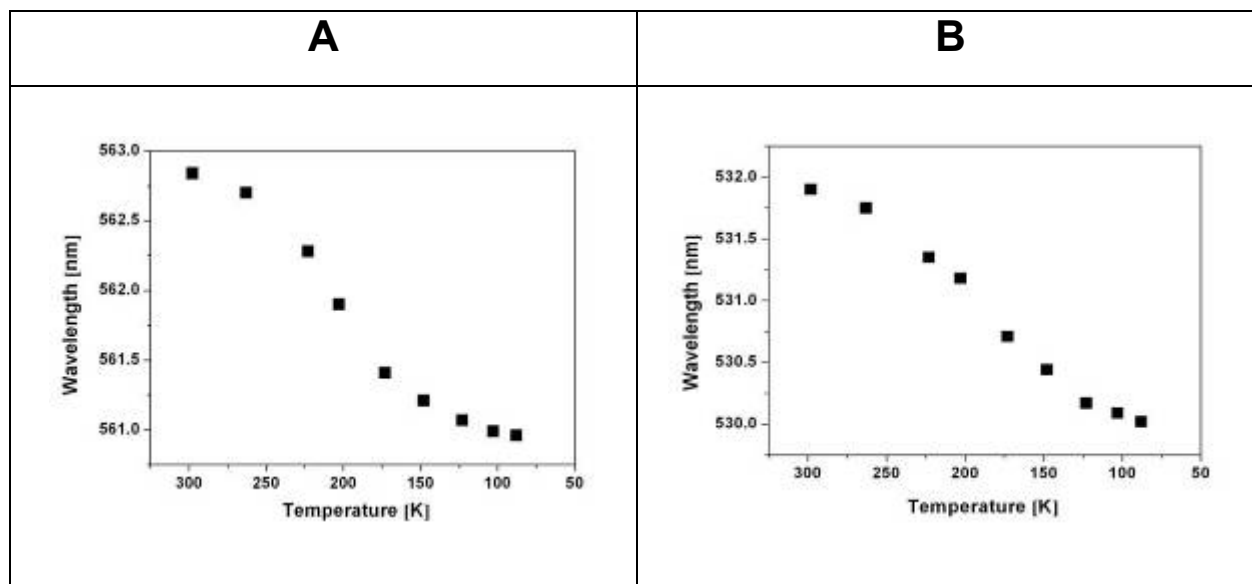


**Figure 40** Plot of the absorption maxima for the  $\alpha$ - band (shown in A) and  $\beta$ - band (shown in B) with the variation of temperatures. Values are taken from the absorption spectra of fully reduced state of QFR represented in Figure 39.

From the absorption spectra it is obvious that with temperature variation (from 300K to 88K), a wavelength shift of the  $\alpha$ - peak (shown in Figure 40 A) as well as the  $\beta$ - peak (shown in Figure 40 B) occurred towards the blue end by 2-3 nm. Remarkable intensification of extinction was observed with lowering temperature. This increase in extinction was induced mainly by multiple reflections from the micro crystals in the frozen samples, and also apparently, in part, by the above sharpening effect of the absorption bands. In contrast, no such effects were observed in the oxidised form of WT QFR (Figure 41).

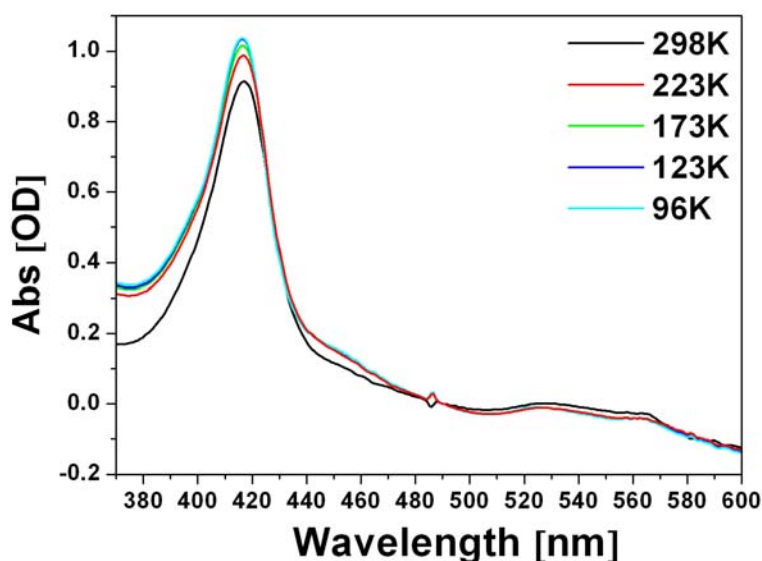


**Figure 41** Changes in absorption spectra of fully oxidised QFR measured at a range of temperatures ranging 298K to 96K. (Experimental conditions and other details are mentioned in the material and method section).

Hagihara and co-workers (Hagihara and Iizuka, 1971), (Hagihara *et al.*, 1974) previously demonstrated the low temperature heme VIS spectra from purified beef-heart cytochromes *a* ( $a_3$ ), *b*, and  $c_1$ , crystalline pigeon breast-muscle cytochrome *c* and crystalline yeast cytochrome *c*, all in the reduced form. In all the cases, prominent peak sharpening (especially of the  $\alpha$ -peak) of the reduced cytochromes was observed when the temperature of the samples was lowered. Separation of the  $\alpha$ -peak into two distinct peaks and a wavelength shift of the  $\alpha$ -peak toward the blue end (by 3-5 nm) were observed when the temperature was lowered from 300K to about 10K. Similar results were obtained in studies on neutrophil *b*-type cytochrome in situ by low temperature absorption spectroscopy (Iizuka *et al.*, 1985). In another study, Low temperature

resonance Raman spectroscopy has been employed to characterize the stabilized intermediate redox states of cytochrome *c* generated by radiolytic reduction of initially oxidized enzyme at liquid nitrogen temperature (Cartling, 1983). It has been shown that the heme group is reduced by hydrated electrons, whereas the protein conformation is restrained close to its oxidized form

### **3.3.3 Time-resolved absorption changes of WT QFR**

The major goal in performing the ultrafast transient absorption experiments was to investigate the process (es) associated with the inter-heme electron transfer within QFR. During electron transfer, an “out-of-equilibrium” excited state configuration can be generated upon absorption of the photon. This can be represented by a “wave-packet” which then evolves towards the equilibrium position. As a prerequisite for the transient absorption experiment, low temperature static VIS redox difference spectra are obtained (section 3.2.2) in order to ensure if there are any distinguishable features between the two hemes in QFR at cryogenic temperatures. Starting with single-heme reduced species, after exciting at 560 nm, it is possible to observe the transient heme absorption bleaching with a time constant of 6.2 picoseconds. In contrast, the heme-oxidised state of the WT QFR sample shows no such bleaching. A control experiment performed with the fully reduced QFR does not show any significant bleaching.

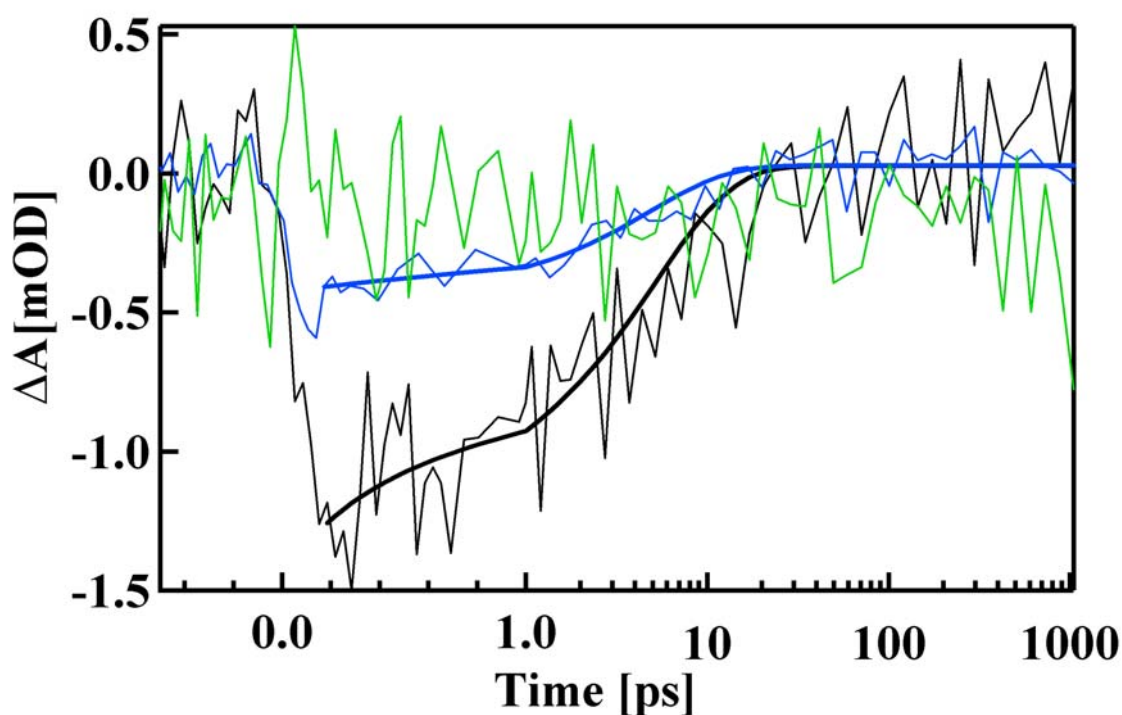


**Figure 42** Comparison of transient absorbance changes of QFR WT sample probed at 558 nm for fully-reduced QFR (shown in blue; time constant of 4.8 ps), semi-reduced (shown in black; time constant of 6.2 ps) and fully-oxidized (shown in green) redox states. Thick lines represent results from the global fit amplitude.

Excitation of semi-reduced QFR at 560 nm results in an instantaneous bleaching of the  $\alpha$ -band (around 560 nm) and the production of an excited state absorption band around 450 nm (Figure 43). Thus, monitoring the bleach band at 560 nm it is possible to obtain information on the lifetime of the selectively excited heme. Figure 42 shows the kinetics measured at 558 nm for fully reduced (shown in blue); semi-reduced (shown in black); and oxidized QFR (shown in green). The experimental data can be satisfactorily fitted using one time constant: 4.8 ps for the fully reduced sample and 6.2 for the semi-reduced sample.

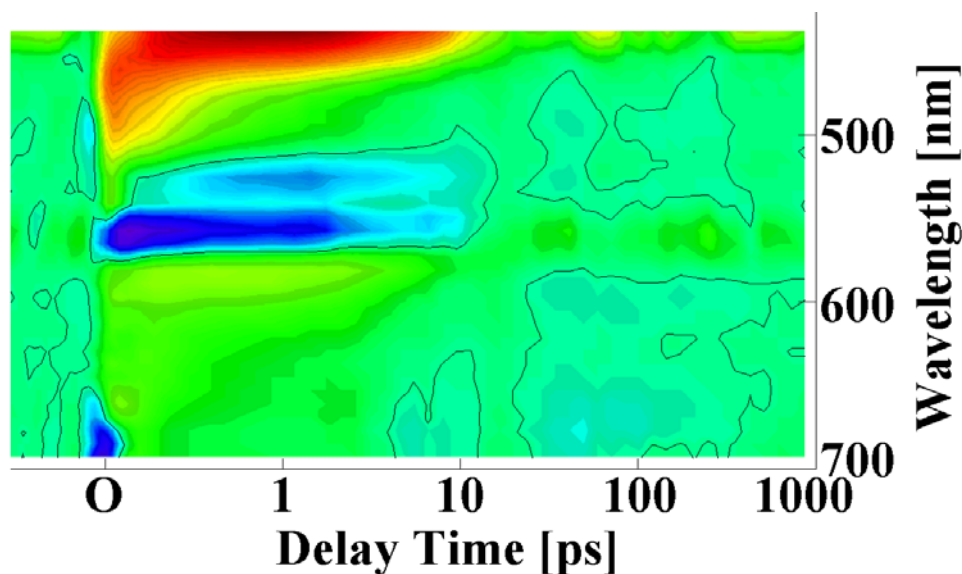


**Figure 43** Temporal evolution of difference absorption spectra of semi-reduced QFR at pH 7.4 after excitation with a 560 nm pulse. Signal amplitudes are colour coded: red indicates positive, and blue negative absorbance change.

Figure 43 represents the 2D contour plot of the transient absorption spectra as described in Figure 42. An indication of product absorption at 690 nm around 100 ps time (Figure 43) could imply that the product of the photo excitation showed spectrum with broad single peak. This could allow reconstruction of the product spectrum.

The extent of heme *b* reduction during the 6 ps phase is indeed far from the full extent of electron transfer in equilibrium. At longer time scales (and at neutral or physiological pH value of 7.4) the 6 ps reaction is followed by a slower electron transfer from the heme *b<sub>p</sub>* to Fe-S clusters and eventually to the FAD (data not shown). The results of the present study may also be compared with the previous work on ferrous cytochrome *c* by Wang *et al* (Wang *et al.*, 2000).

In a control experiment with fully reduced QFR, no bleaching signal was observed (Figure 42). This can be expected result because of existence of rapid electron-transfer equilibrium between the two heme redox centers in the fully reduced state of the enzyme. Nevertheless, transfer of electron from the high potential heme *b<sub>p</sub>* to its nearby cofactor [3Fe-4S] cluster can not be ruled out as the Fe-S cluster is situated within the range of physiological electron transfer distance.



### 3.3.4 Absorption anisotropy and heme reorientation dynamics in QFR

Being a planar chromophore, heme is less sensitive to the mutual orientation of pump- and probe-beam polarization. Theoretically, the limiting values of anisotropy are 0.1 and 0.4 for planar and linear chromophores, respectively (Wang *et al.*, 2000). In the present case involving QFR, heme anisotropy value of approximately 0.06 is obtained at a delay time of 1 ps (Figure 44). This value is well within the theoretical limit. In case of cytochrome *c*, the rotational depolarisation can be neglected because cytochrome *c* is a protein with the heme embedded in it and such a large object can not rotate significantly on the time scale of tens of picoseconds (Ansari *et al.*, 1993).

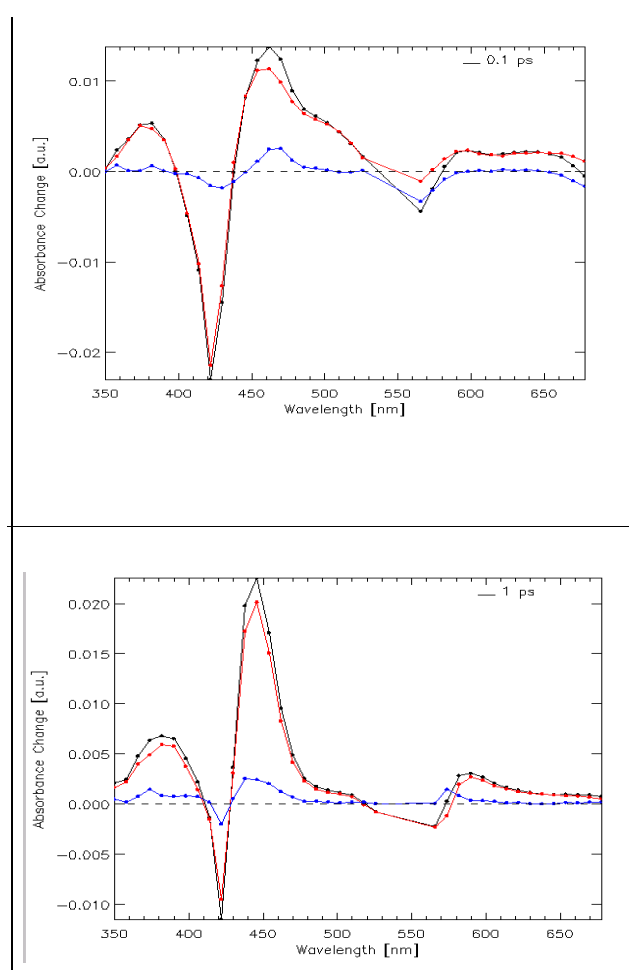


**Figure 44** Transient bleach VIS absorption spectra of QFR semi-reduced redox state under 0.1 ps (upper panel) and 1 ps (lower panel) time delay. The colour coding shown in black represents parallel detection; colour coding shown in red represents perpendicular detection; and blue colour represents the difference between the parallel and perpendicular detection.

## 4 Discussion

In the following sections, the outcomes from the different spectroscopic approaches to study the electron coupled proton transfer mechanism have been discussed.

### 4.1 Electrochemically induced static FTIR spectroscopic approaches

In section 4.1.1, the redox-dependent protonation change of the residue Glu C180 in wild type enzyme as a function of pH are discussed in detail. In section 4.1.2, vibrational contributions from the heme porphyrin groups and the histidine ligand are discussed in detail.

#### 4.1.1 pH dependence of FTIR difference spectra of enzyme variant E180Q and QFR WT

For *W. succinogenes* wild-type QFR, employing electrochemically induced static FTIR difference spectroscopy (in the mid-infrared region from 1800 to 1000  $\text{cm}^{-1}$ ) it has been demonstrated that the redox-dependent protonation change of the conserved residue Glu C180 is a function of pH. Such a pH-dependence of the oxidation-reduction midpoint potentials of the heme groups has been measured previously (unpublished data). Comparisons of the results obtained for the E180Q variant enzyme indicate a key role of Glu C180 in establishing this pH-dependence in the wild-type enzyme. As indicated by FTIR double difference spectroscopy, single heme reduction is sufficient for significant protonation of Glu C180 to occur and there is very little additional protonation of this residue in the fully reduced enzyme in the physiological pH range. The pH dependence of the protonation of Glu C180 upon single reduction is also predicted by the corresponding multiconformation continuum electrostatics (MCCE) calculations.

Reduced-minus-oxidized QFR WT-minus-E180Q mutant FTIR double-difference spectra shows pH dependence with redox triggering of the heme groups (Figure 18). In order to normalise distinct spectra, the absorbance difference bands of QFR WT and E180Q mutant at 1678  $\text{cm}^{-1}$  and 1501  $\text{cm}^{-1}$  are normalised for all pH values. The double difference spectra at 1740-1742  $\text{cm}^{-1}$  show maximum absorption around pH 7.5 and pH 8. This is in line with the fact that FTIR double-difference spectra of QFR WT and

E180Q variant show maximum absorption intensity around 1740-1742  $\text{cm}^{-1}$  region (previous study at pH 7, (Haas *et al.*, 2005) and reflects perfect agreement with the assignment for the  $\nu(\text{C}=\text{O})$  stretching vibrations of the protonated carboxyl groups. The reduction of a single heme, namely the high potential proximal heme  $b_P$ , is already sufficient for the significant protonation of Glu C180 residue. The additional protonation of this Glu C180 minimally depends on the reduction of the low potential distal heme  $b_D$  within the physiological pH range. This pH dependence also correlates perfectly with the pH dependence of the quinol oxidation activity of the enzyme. Furthermore, as inferred from the E-pathway, the redox-switch for coupled transmembrane electron and proton transfer, namely the Glu C180, is not functional in the variant. This agrees with the above-mentioned results from FTIR spectroscopy and electrostatic calculations.

The pronounced differences found for WT and E180Q point out that Glu C180 is unequivocally involved in the pH-dependence of the heme midpoint potentials due to redox-coupled (de)protonation and/or an environmental change of this residue. The discrepancy between  $pK_{\text{ox}}$  and  $pK_{\text{red}}$  for WT and E180Q, respectively, is considerably stronger for the high potential “proximal” heme ( $b_P$ ) than for the low potential “distal” heme ( $b_D$ ). In the variant E180Q, the high potential heme is much harder to oxidize at pH values above pH 5.5. This indicates that the invariably neutral charge on the side chain of the Gln C180 in the variant, which mimics the Glu C180 in its neutral protonated state, stabilizes the reduced state of the proximal heme. The asymmetry of the impact of the mutation E180Q on the heme redox behavior may be related to the observed conformational change of Glu C180, which occurs in a concerted manner with respect to proton uptake upon reduction of the hemes. Most probably, the Gln C180 side chain in the variant is locked in an orientation that is similar to the one of Glu C180 in the protonated state. In addition, the proximal heme is inevitably harder to re-oxidize in the variant since the Gln C180 can not be deprotonated to electrostatically ease the re-oxidation of heme  $b_P$  as it is conceivable for the Glu C180 in the WT enzyme. Consequently, as observed experimentally, the activity of the enzyme variant E180Q is substantially reduced compared to the WT.

The observation of a redox Bohr effect in the variant E180Q also proves that Glu C180 is not the only protolytic group responsible for the pH-dependence of both heme groups of QFR. For the low potential heme the differences in the variant might be less

pronounced because the ring C propionate of this heme could be the dominating protolytic site for  $b_D$ . The redox Bohr effect of the high potential heme in the variant yields evidence for the presence of further protolytic groups which, in addition to Glu C180 in the WT, interact with heme  $b_P$ . Thus, this conclusion from the obtained data represents an essential prerequisite for the existence of a functional “E-pathway”, since Glu C180 alone does not suffice for efficient proton transfer across the bacterial membrane.

#### 4.1.2 pH and redox dependence of the individual heme porphyrin signal and other relevant residues in QFR WT

Although considerable efforts have been devoted and significant details are already known regarding the catalytic mechanism and enzymatic function of QFR, only little is known to date about the low infrared contribution of the heme porphyrin modes and the heme-ligating groups. This work demonstrates the first redox and pH dependent FTIR characterisation study on *W. succinogenes* QFR in the low frequency range below  $1000\text{ cm}^{-1}$ . Prominent and reversible band patterns arise upon redox induced reactions suggesting that the redox induced FTIR difference spectroscopy of QFR is redox-tunable, fully reversible and sensitive in the  $2000\text{-}500\text{ cm}^{-1}$  range. Spectral features are in agreement with previous studies (Haas *et al.*, 2005) within  $2000\text{-}1000\text{ cm}^{-1}$  region suggesting that spectral data are reproducible. Minor differences may arise due to use of different buffers and applied experimental conditions. It is observed that specific bands arising in the redox difference spectra of *W. succinogenes* QFR are responsive to the contribution of particular heme groups, pH, iron-ligated histidine and  $\nu(\text{C}_m\text{H})$  vibration of the heme porphyrin ring system. For instance, the  $\nu(\text{C}_m\text{H})$  mode is found to be conserved in all pH cases and may serve as a marker band in further studies as established previously for *c*-type hemes (Dörr *et al.*, 2006).

Redox-linked protonation behaviour of histidine has been well discussed previously in Iwaki *et al.* (Iwaki *et al.*, 2005). FTIR measurements of model compounds of the histidine side chain showed that the C5-N1 stretching band around  $1100\text{ cm}^{-1}$  can be a useful IR marker of the N $\delta$  protonated histidine imidazole ring (Noguchi *et al.*, 1999), (Mesu *et al.*, 2005). In the present case, the histidine signal at  $1109\text{ cm}^{-1}$  can be observed (Figure 20 and Figure 21). The corresponding  $\nu(\text{C}_5\text{N}_\tau)$  ring mode of histidine was assigned at  $1113\text{-}1104\text{ cm}^{-1}$  in the Fe, Cu, or Zn -bound complexes, especially

$\nu(\text{C}_5\text{N}_\tau)$  ring mode of the proximal histidine ligand of Fe(III) was detected at 1105-1100  $\text{cm}^{-1}$  (Marboutin *et al.*, 2009). Presence of hydrogen bond between histidine fifth axial ligand and a peptide carbonyl group can also be concluded from the previous study (Marboutin *et al.*, 2009).

Histidine shows a prominent and sharp peak at 624  $\text{cm}^{-1}$  (Dörr *et al.*, 2008), (Wolpert and Hellwig, 2006), (Hasegawa *et al.*, 2000), (Marboutin *et al.*, 2009) which can be observed better with a Hg-light source equipped with changed beam splitter and other optical detection parameters. The frequency shift in case of axial histidine ligands has been attributed to anharmonic coupling (Franzen *et al.*, 2000) and change of molecular symmetry in the coordination of iron center with histidines (Dörr *et al.*, 2006). In general, frequency of the out-of-plane mode of the axial ligand vibration is dependent on the metal-ligand bond stretching strength as well as the motion of the iron with respect to the porphyrin ring (Franzen *et al.*, 2000). The electronegative character and bending of the imidazole ring of the ligand with respect to the porphyrin ring plane is also a determining factor of the vibrational frequency (Berthomieu *et al.*, 2006), (Hasegawa *et al.*, 2000), (Iwaki *et al.*, 2005).

The present work demonstrates the coupling between protonation and electron transfer (ET) reactions in transmembrane redox protein QFR, which includes axially coordinated bis-histidine-ligated heme iron along with several other redox active cofactors. In the oxidation-reduction process of the QFR, the distal heme-ligated histidines possibly undergo protonation-deprotonation. Most likely, a conformational change of a histidine ligand occurs upon reduction of the enzyme. This apply either to only one or both of the axial histidine ligands of the distal heme. Histidine should show displacement from heme or conformational differences in rather low pH than high pH because protonation of histidine occurs in the low pH range. Reduction of distal heme facilitates the protonation of one of the axial histidine ligands. In other words, the uptake of an electron causes the protonation of axial histidine of the distal heme in particular. Previous studies by FTIR difference spectroscopy revealed that upon redox changes of the distal heme, there is an involvement of that heme propionate in the electron-coupled proton transfer in QFR (Mileni *et al.*, 2005).

Our data suggest that the coupling mechanism between proton and electron transfer may involve a change in the heme environment. The position and orientation of

the histidine backbone relative to the heme plane and relative to the second histidine can be altered. Furthermore, this could influence the hydrogen bonding pattern of imidazoles axially coordinated to heme by means of electrostatic interactions. The local environment of ring C propionate of distal heme  $b_L$  is hydrophobic enough not to be involved in any hydrogen bonding (Mileni *et al.*, 2005), (Lancaster *et al.*, 1999). Although the FTIR signals within the presented experimental range does not yield any information regarding the protonation of the Glu C180 residue, it is most likely the candidate for next protonation to be transferred after histidine coupled to the heme reduction, as established by previous studies (Haas *et al.*, 2005), (Lancaster *et al.*, 2005), (Madej *et al.*, 2006a). Costa *et al.* (1992) reported that upon reduction, one of the axial histidines in cytochrome  $c''$  is detached and left free to take up a proton in the physiological pH range, with no change in the total charge around the heme on going from the oxidised to the reduced state. Analogously, the present mechanism in QFR suggests that one of the distal heme faces is fairly accessible to solvent protons in order to allow histidine protonation.

Future studies, addressing the assignment of signals to specific histidine residues, should involve suitable heme-retaining replacements of the histidine ligands by site-directed mutagenesis. However replacement of the histidine side chain can possibly result in loss of the heme group. Simon *et al.* (Simon *et al.*, 1998) observed that replacement of any of the four histidine ligands with alanine prevents the formation of functional *W. succinogenes* QFR. On a related, but different diheme-containing succinate:quinone oxidoreductase, Hägerhäll *et al.* (Hägerhäll *et al.*, 1995) reported that mutation of the axial histidine ligands (His28 and His113) by tyrosine in the isolated mutant in Cyt  $b558$  resulted in loss of heme  $b_L$ . A significant structural change in the local environment of the heme  $b_H$  was a result of the His13 mutation, as was evident from EPR spectroscopy. For more detailed assignments of histidines, isotope labeling experiments (Kimura *et al.*, 2003) are necessary. Several studies have been performed replacing the axial heme ligating histidine by exogenous small ligands and thereby monitoring the protein's functionality and mechanistic pathways in the changed heme coordination environment (Barrick, 2002), (Hirst *et al.*, 2001).

## 4.2 Time-resolved FTIR spectroscopic approaches

In section 4.1.2, characterisation of caged fumarate and FTIR spectroscopic studies on the on the interaction of the released fumarate with QFR have been discussed. A different and alternative approach by using caged-quinol, subsequent release of quinol, thereby of initiating and probing the enzymatic reaction are discussed in section 4.2.2.

### 4.2.1 Comparison of the kinetic FTIR difference spectra of fumarate substrate

The novel CNB-caged fumarate compound is suitable for kinetic measurements with *W. succinogenes* QFR and is generally applicable for all studies involving fumarate reactions. In the context of the present work, it has been shown that this newly synthesised CNB-caged fumarate has been physico-chemically characterized and FTIR difference band positions (after photolysis) have been assigned accordingly. The release of fumarate occurs in the submillisecond time range and the enzyme is active only when fumarate is released. As the nitrobenzyl moiety of the  $\alpha$ -CNB group is hydrophobic, it may interact and thereby associate with the hydrophobic part of proteins. Hydrophilicity of  $\alpha$ -CNB group can be increased with possible inclusion of additional carboxylate protecting group. For instance, 4-dicarboxy-2-nitrobenzyl (4-DCNB) resulted in an improved distribution of the compound in aqueous and hydrophobic phase, with an inclination to be more in the aqueous phase (Schaper *et al.*, 2002). The strong absorbance of the solvent water is an obstacle inherent to infrared techniques. Therefore, experiments had to be carried out with highly concentrated sample layer with very thin aqueous films. This need is indeed a conflicting factor in the present study because efficient mixing of reactant may not be guaranteed due to high sample concentration and enzymatic reactions could be diffusion controlled. A similar phenomenon was reported earlier (Ludovici *et al.*, 2002) on a related study of the reaction of cytochrome *bo*<sub>3</sub> oxidase with photochemically released dioxygen from a cobalt peroxo complex.

In the context of the reaction of *Escherichia coli* cytochrome *bo*<sub>3</sub> and mitochondrial cytochrome *bc*<sub>1</sub> complexes, Hansen *et al* (Hansen *et al.*, 2000) explored the possibility of using the 3',5'-dimethoxybenzoin (DMB) moiety as a protecting group. The rapid photolysis rate and a facile synthesis of the DMB group made its use desirable. However, poor solubility of the caged ubiquinol in aqueous media prevented

full characterisation of the compound and hence led to the use of another new protecting group, namely the 3',5'-bis(carboxymethoxy)benzoin (BCMB) where the methoxy group is replaced with carboxymethoxy group (Hansen *et al.*, 2000). This decylubiquinol based on BCMB is water-soluble. In the present context our preferred caging group is 1-(4, 5-dimethoxy-2-nitrophenyl)ethyl (DMNPE).

A considerable masking effect is observed in the spectra when WT QFR is present with the caged fumarate. Nevertheless, the presently detected signals indicate small but specific conformational changes in spite of the fact that the relatively strong band characteristics from the cage release may still mask the protein signals. The observed subtle changes probably involve only a few amino acids upon binding with QFR. As mentioned in Lancaster *et al.* (2001), the capping domain of the hydrophilic subunit A in *Wolinella succinogenes* QFR is the most susceptible candidate for a larger conformational movement. The fumarate binding site is located close to this domain. As evident from the preliminary results from ATR difference spectra, the secondary structural changes are consistent with a major contribution from this capping domain movement. Together with the protein secondary structural changes mainly speculated to be centred at the capping domain of QFR, the consideration of the possibility of an internal proton movement with substrate binding can not be ruled out. The bands from deprotonated carboxylate and protonation of a possible Glu (and/or Asp) residue(s) may invoke to draw such conclusion.

The alterations in different secondary structural elements proposed here can involve not more than five amino acid residues which can be centred in the capping domain movement in fumarate binding region in QFR. In case of redox induced conformational changes in amide I band in heme-copper oxidases cytochrome *aa*<sub>3</sub> from *R. sphaerodes* and ubiquinol oxidase from cytochrome *bo*<sub>3</sub> from *E. coli*, 3 to 5 peptide bonds were involved (Lübben and Gerwert, 1996). In case of QFR, redox induced conformational changes can also involve such a comparable number of peptide bonds (Haas and Lancaster, 2004). Therefore, it can be concluded that only a few peptide bonds which serve as a hinge for the rigid domain movement are involved in the structural changes of QFR. The fumarate-binding site is localised in the flavoprotein subunit A of the enzyme (Lancaster *et al.*, 1999) between the FAD-binding domain and the capping domain next to the plane of the FAD isoalloxazine ring. As reported earlier,



a third crystal form “C” of QFR revealed domain closure at the site of fumarate reduction (Lancaster *et al.*, 2001). In other words, binding of substrate fumarate induces movement of the capping domain to close the active site to solvent. In ATR-FTIR studies the molecular mechanisms involving conformational changes of QFR can be studied at conditions close to the native reactions, even for detergent solubilised protein. The data obtained from the spectroscopic studies, therefore, complements and supplements the structural information obtained from the crystalline state (Lancaster *et al.*, 1999), (Lancaster *et al.*, 2001).

This work presents characterisation of a novel cage substrate and FTIR spectroscopic studies on the interaction of the released substrate with a redox enzyme. Further investigations for a deeper time-resolved understanding of the redox mechanisms would require studies on QFR enzyme variant with substrate and the use of appropriate photo labile caged substrate analogs. Motivations to design modified cages may include isotopically labelled ( $^{13}\text{C}$ ,  $^{18}\text{O}$  or both) cages.

#### **4.2.2 Comparison of the kinetic FTIR difference spectra of the caged MMAN with the absence and presence of QFR WT**

The photosynthetic RCs are generally regarded as a model system to study quinone reaction (Lancaster *et al.*, 1995), (Lancaster, 1998) because short laser pulses (or continuous illumination) can induce the reaction of quinones. Therefore, a detailed understanding of the kinetics and energetics of quinone redox chemistry is possible. Information regarding the conformation of the ring and the substituents as well as the hydrogen-bonding details can be well investigated with the help of FTIR difference spectroscopy (Gerwert, 1993). Flash (reaction)-induced FTIR difference spectroscopy (Mezzetti *et al.*, 2003), (Mezzetti and Leibl, 2005) help to understand changes in the active sites or in the quinone binding site in QFR with selected sensitivity.

Here in the context of the present work a novel caged compound is introduced, namely the caged quinol analogue of the naturally occurring menaquinol in QFR. QFR catalyzes the oxidation of menaquinol to promote the reduction of fumarate to succinate. Thus, the electron-coupled transmembrane proton transfer can essentially reduce specific residues and cofactor in its path, thereby reflecting the subsequent changes in the FTIR difference spectra.

A major limitation in difference FTIR method is that vibrational modes from all the bonds from both the cofactor and the protein that have been perturbed lead to crowded difference spectra. Therefore, it is hard to assign the quinone vibrations (Buchanan *et al.*, 1992) and to distinguish them from the overlapping protein modes. Future directions could employ chemically modified cofactors or isotopically labeled compounds. The geometry of the methoxy groups in ubiquinone in the Q<sub>A</sub> and Q<sub>B</sub> sites was probed with ubiquinones selectively labeled at C-2 or at C-3 (Breton *et al.*, 1996). Approaches could combine site-directed mutagenesis (Breton *et al.*, 1996), (Hienerwadel *et al.*, 1995), (Nabedryk *et al.*, 1995), <sup>1</sup>H/<sup>2</sup>H exchange (Breton *et al.*, 1996), (Hienerwadel *et al.*, 1995), (Nabedryk *et al.*, 1995) and selective labeling of a single type of amino-acid residue.

Although experiences have indicated that it is not necessary to rigorously protect the caged reagent and the reaction products from normal ambient light, it is advised that these caged materials should not be exposed to direct sunlight or other strong sources of UV radiation. As simple and worthwhile precaution, wrapping reaction vessels and chromatography columns with aluminium foils are suggested. Caged materials appear to be less stable in solution and on silica gel than in solid form. DMNPE caged probes are recommended to store at -20°C with desiccant without any light exposure.

One of the obvious observations regarding caged MMAN(H<sub>2</sub>) dissociation in presence of QFR is the shading effect. The two heme *b* groups in QFR render the sample to be highly reddish-brown coloured at a substantial protein concentration of ~1 mM. This can shield the cage to get flashed, thereby lowering down the quantum yield for flash efficiency to be smaller. The caged MMAN is intensely reddish coloured at the experimental concentration due to the presence of the two methoxy- and nitro- group's side chains. In the FTIR spectra, spectral trace from the cage (only) has almost double intensity of absorption difference signals compared to that when QFR is present with the cage, the sample layer thickness and the other experimental conditions being identical.

### 4.3 Interheme electron transfer in the semi-reduced state of QFR WT

In many key mechanisms of biological energy conversion, the long range electron-transfer reactions are rapid and thus can not be resolved using conventional techniques. Figure 45 shows the experimentally deduced midpoint potentials of the substrates, prosthetic groups, and cofactors (as well as the corresponding electron transfer rates) of

*Wolinella succinogenes* WT QFR, which are involved in the catalytic mechanism of the enzyme. The scheme shows that some of the involved electron transfer steps are endergonic and some are exergonic (Figure 45). Efficient tunnelling of electrons is ensured due to the spatial proximity of the prosthetic groups and cofactors. The electron transfer step from MKH<sub>2</sub> to heme *b<sub>P</sub>* actually consists of two individual steps, being rate limited by the MKH<sub>2</sub> to *b<sub>D</sub>* step. It is obvious that, being energetically favoured, the electron transfer from *b<sub>D</sub>* to *b<sub>P</sub>* has to be much faster than the MKH<sub>2</sub> to *b<sub>D</sub>* rate. In case of the QFR, upon rapid excitation, the electron can have two possibilities/destinations to transfer: (i) it can be transferred to the low potential heme *b* or (ii) it may itself show relaxations to its own ground state.

Depending on the structure of biomolecules, the nature of the electron transfer shows pathway specificity (Gray and Winkler, 1996), (Verkhovsky *et al.*, 2001) which allows structural control over the electron transfer rate. Empirical theory of non-adiabatic electron transfer states that electron tunnelling rate between the biological cofactors is determined by the “edge-to-edge” distance between them and the atomic packing density of the intervening structure. Over distances greater than 14 Å, a high directional specificity often exists to transfer electrons in natural systems (Page *et al.*, 1999). Multistep tunneling accompanying several endergonic steps through chains of redox centres individually spaced within the 14 Å limit may occur. The specificity of the molecular interactions and the molecular cofactor electrostatics suggest that crystallographic structure (Lancaster *et al.*, 1999) as well as the established E-pathway (Madej *et al.*, 2006a) represents a highly probable conformational state of an electron transfer complex between the two hemes in QFR during its catalytic mechanism.

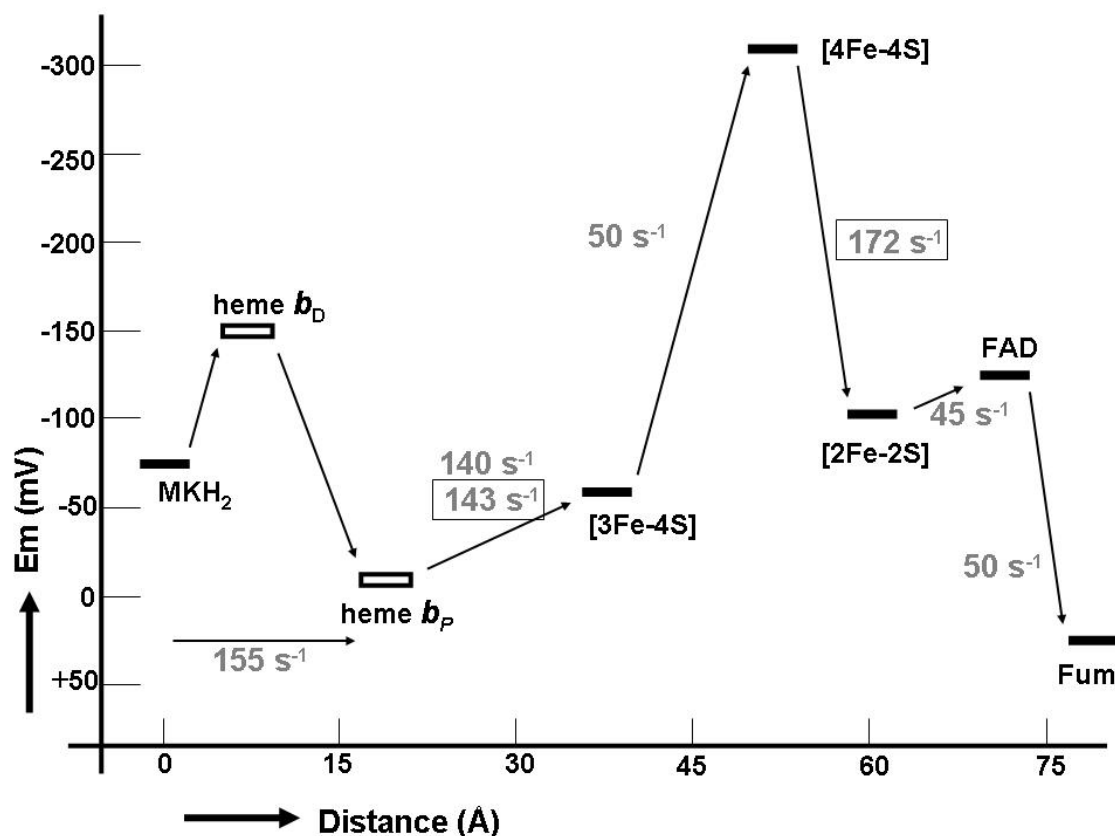


**Figure 45** Oxidation-reduction (midpoint) potentials (in mV) of the constituents of the electron transport chain of the *W. succinogenes* QFR. The distances are given in Å and refer to inter-cofactor distances. Electron transfer rate constants between cofactors; reduction rates of components of the fully oxidized enzyme upon addition of DMNH<sub>2</sub>; in box are reoxidation rates of the fully reduced enzyme by fumarate (Haas and Lancaster, 2004) and  $E_m$  values for Fe-S clusters are updated from (Mileni *et al.*, 2006).

In summary, it has been demonstrated that picosecond pump-probe transient absorption can be employed to study the intramolecular rapid heme-heme electron transfer as a part of the catalytic mechanism of the redox active protein QFR in its detergent solubilised state and at room temperature condition. Although no definite estimation of the percentage of photoexcitation of the total heme and the photolysis quantum yield can be made, a possibility of ligand photodissociation after photoexcitation (Abbruzzetti *et al.*, 2006) can not be ruled out. Photodissociation of ligand occurs in less than 50 fs time using femtosecond pulses with a quantum yield of approximately unity. The ground state unligated heme species appears in 300 fs. Two distinct excited heme species was shown to be formed upon ligand photodissociation (Martin and Vos, 1992). Previous work on cytochrome *c* and cytochrome *b<sub>5</sub>* also suggested ligand photodissociation after excitation (Jongeward *et al.*, 1986), (Jongeward *et al.*, 1988).

Although the question of which particular bond (Fe-His or Fe-Met) is photolyzed remained open, Jongeward *et al.* (Jongeward *et al.*, 1986), (Jongeward *et al.*, 1988) suggested that the Fe-His bond breaks upon photoexcitation. Detailed investigation involving line shape and evolution of the isosbestic point of the reported spectra suggested that photolysis might not take place in cytochrome  $b_5$  and that the assignment of histidine ligand photolysis in cyt  $c$  might be inconclusive though (Jongeward *et al.*, 1986). In the oxidation-reduction process of the QFR, heme-ligated bis-histidine possibly undergoes protonation-deprotonation and most likely a displacement from heme or conformational differences of this histidine ligand occurs upon reduction of the enzyme (Paul, R., Hellwig, P., Khoury Y., and Lancaster, C.R.D. (2011) *manuscript under preparation*) at a relatively lower pH value. This could either apply to only one histidine or both the axial histidine ligands. Reduction of distal heme facilitates the protonation of axial histidine of the distal heme in particular. Previous studies by FTIR difference spectroscopy reveal that upon redox changes of the distal heme, there is an involvement of that heme propionate in the proton coupled electron transfer in QFR (Mileni *et al.*, 2005).

## 5 Concluding remarks and perspectives

The main aim of the project was to obtain, by employing a combination of static difference and time-resolved spectroscopic approaches, a detail insight of the transmembrane electron coupled proton transfer mechanism in *W. succinogenes* QFR. On the basis of the results obtained from individual sub-projects, the following conclusions can be drawn.

1.) pH-dependence of the oxidation-reduction midpoint potentials of the heme groups has been previously measured for *W. succinogenes* QFR. Comparison of the results to those obtained for the E180Q variant enzyme indicates a key role of Glu C180 in establishing this pH-dependence in the wild-type enzyme (Paul, R., Haas, A.H., Madej, M.G., Mäntele, W., and Lancaster, C.R.D., *manuscript in preparation*). As indicated by electrochemically induced FTIR double difference spectroscopy, single heme reduction is sufficient for significant protonation of Glu C180 to occur and there is considerably less extent of additional protonation of this residue in the fully reduced enzyme in the physiological pH range. The pH dependence of the protonation of Glu C180 upon single reduction is supported by the complementary electrostatics calculations. This nature of pH dependence correlates very well with the pH dependence of the quinol oxidation activity of the enzyme.

2.) The data from redox-induced low-IR experiments are compatible with the coupling mechanism between proton and electron transfer involving a change in the heme environment. The  $\gamma(\text{CH})$  vibration of the heme porphyrin ring depends on oxidation state of heme propionates. The position and orientation of the histidine backbone relative to the second histidine can be altered. Reduction of the distal heme, in particular, facilitates the protonation of one of the axial histidine ligands (Paul, R., Hellwig, P., Khoury Y., and Lancaster, C.R.D., *manuscript in preparation*).

3.) Synthesis and broad physico-chemical characterisation of a CNB-caged fumarate is presented. This novel caged substrate is found to be suitable for kinetic measurements with *W. succinogenes* QFR and is generally applicable for all studies involving fumarate reactions. The release of fumarate occurs in the submillisecond time range and the

enzyme is active only when fumarate is released. The detected FTIR difference signals indicate small but specific conformational changes in WT QFR upon fumarate binding. The secondary structural changes are consistent with a major contribution from the capping domain movement of the hydrophilic subunit A, located close to the fumarate binding site (Paul, R., Bamann C., Enela Džafić, E., Mileni, M., Fendler, K., Mäntele, W., and Lancaster, C.R.D., *manuscript in preparation*).

In a complementary approach to study the catalytic mechanism, a novel caged quinol analog is introduced. Kinetic FTIR differences characteristically represent the cage dissociation, but the dissociation event is fast enough to detect susceptible protein conformational changes with the limited time resolution of the methodology.

4.) It has been demonstrated that ultrafast transient absorption spectroscopy can be employed to study the intramolecular rapid heme-heme electron transfer as a part of the QFR catalytic mechanism. Generation of mixed valenced QFR state is possible by selective chemical reduction of heme by using  $\text{DMNH}_2$ . Resulting in a time constant of 6.2 ps, excitation of the semi-reduced QFR allows probing the life time of the selectively excited heme (In collaboration with S. Amarie and J. Wachtveitl). This finding means that the excitation state of the high potential heme is significantly unstable and inter-heme electron transfer is in the time-scale of pico seconds. The oxidised state of the enzyme, serving as a control, demonstrates the absence of any heme bleaching signal.

In summary, recent advances in understanding the trans-membrane electron coupled proton transfer (ECPT) mechanism in QFR have been discussed. Most of the results discussed in this thesis have been obtained by employing time-resolved as well as static spectroscopic approaches. From the static FTIR spectroscopic studies, the redox-dependent protonation changes of the “key” residue Glu C180 has been discussed in the context of E-pathway. Only a single heme reduction act as a protonation triggering switch for Glu C180 and one of the heme-ligated axial histidine ligands. The redox dependent protonation and conformational change of the heme-ligated histidine has been discussed. The time-resolved FTIR spectroscopic studies indicated small but specific conformational changes in QFR upon substrate (fumarate/quinol) binding. Excited state life-time and an electron transfer equilibration rate between the low- and high- potential heme were possible to probe by employing

transient absorption spectroscopy. Taken together, the outcomes of the studies help in-depth understating of the molecular processes associated during catalytic activity of QFR.

Future studies, addressing the assignment of signals to specific histidine residues, should involve suitable heme-retaining replacements of the histidine ligands by site-directed mutagenesis. For more detailed assignments of histidines, isotope labeling experiments (Kimura *et al.*, 2003) are necessary. Several studies have been performed replacing the axial heme ligating histidine by exogenous small ligands and thereby monitoring the protein's functionality and mechanistic pathways in the changed heme coordination environment (Barrick, 2002), (Hirst *et al.*, 2001). Further investigations for a deeper time-resolved understanding of the redox mechanisms would require studies on QFR enzyme variant with substrate and the use of appropriate photo labile caged substrate analogs. Motivations to design modified cages may include isotopically labelled ( $^{13}\text{C}$ ,  $^{18}\text{O}$  or both) cages. Approaches could combine site-directed mutagenesis (Breton *et al.*, 1996), (Hienerwadel *et al.*, 1995), (Nabedryk *et al.*, 1995),  $^1\text{H}/^2\text{H}$  exchange (Breton *et al.*, 1996), (Hienerwadel *et al.*, 1995), (Nabedryk *et al.*, 1995) and selective labeling of a single type of amino-acid residue. A spectroelectrochemical cell compatible with the femtosecond transient absorption setup with 1 mm pathlength can be used in future. With this kind of cell, the chemical single-heme reduction issue can be avoided because an accurate control of the redox potential will be possible from the externally installed potentiostat. The use of E180Q variant for similar kind of measurements would be of course the next evident control experiments.



## 6 References

- Abbruzzetti, S., Bruno, S., Faggiano, S., Grandi, E., Mozzarelli, A. and Viappiani, C. (2006) Monitoring haem proteins at work with nanosecond laser flash photolysis. *Photochem. Photobiol. Sci.*, **5**, 1109-1112.
- Alexov, E.G. and Gunner, M.R. (1997) Incorporating protein conformational flexibility into the calculation of pH-dependent protein properties. *Biophysical Journal*, **72**, 2075-2093.
- Alexov, E.G. and Gunner, M.R. (1999) Calculated Protein and Proton Motions Coupled to Electron Transfer: Electron Transfer from QA<sup>-</sup> to QB in Bacterial Photosynthetic Reaction Centers. *Biochemistry*, **38**, 8253-8270.
- Amarie, S., Standfuss, J.r., Barros, T., Kühlbrandt, W., Dreuw, A. and Wachtveitl, J. (2007) Carotenoid Radical Cations as a Probe for the Molecular Mechanism of Nonphotochemical Quenching in Oxygenic Photosynthesis. *The Journal of Physical Chemistry B*, **111**, 3481-3487.
- Ansari, A., Jones, C.M., Henry, E.R., Hofrichter, J. and Eaton, W.A. (1993) Photoselection in polarized photolysis experiments on heme proteins. *Biophys. J.*, **64**, 852-868.
- Bamann, C., Kirsch, T., Nagel, G. and Bamberg, E. (2008) Spectral Characteristics of the Photocycle of Channelrhodopsin-2 and Its Implication for Channel Function. *Journal of Molecular Biology*, **375**, 686-694.
- Barrick, D. (2002) Replacement of the Proximal Ligand of Sperm Whale Myoglobin with Free Imidazole in the Mutant His-93-->Gly. *Biochemistry*, **33**, 6546-6554.
- Barth, A. (2000) The infrared absorption of amino acid side chains. *Progress in Biophysics and Molecular Biology*, **74**, 141-173.
- Barth, A., Corrie, J.E.T., Gradwell, M.J., Maeda, Y., Mantele, W., Meier, T. and Trentham, D.R. (1997) Time-Resolved Infrared Spectroscopy of Intermediates and Products from Photolysis of 1-(2-Nitrophenyl)ethyl Phosphates: Reaction of the 2-Nitrosoacetophenone Byproduct with Thiols. *Journal of the American Chemical Society*, **119**, 4149-4159.
- Barth, A., Germar, F.v., Kreutz, W. and Mantele, W. (1996) Time-resolved Infrared Spectroscopy of the Ca<sup>2+</sup>-ATPase. *Journal of Biological Chemistry*, **271**, 30637-30646.
- Barth, A., Hauser, K., Maentele, W., Corrie, J.E.T. and Trentham, D.R. (1995) Photochemical Release of ATP from "Caged ATP" Studied by Time-Resolved Infrared Spectroscopy. *Journal of the American Chemical Society*, **117**, 10311-10316.

- Barth, A. and Zscherp, C. (2000) Substrate binding and enzyme function investigated by infrared spectroscopy. *FEBS Letters*, **477**, 151-156.
- Barth, A. and Zscherp, C. (2002) What vibrations tell us about proteins. *Quart. Rev. Biophys*, **35**, 369-430.
- Bauscher, M. and Mäntele, W. (1992) Electrochemical and infrared-spectroscopic characterization of redox reactions of p-quinones. *The Journal of Physical Chemistry*, **96**, 11101-11108.
- Baymann, F., Moss, D. and Mäntele, W. (1991) An electrochemical assay for the characterization of redox proteins from biological electron transfer chains. *Anal Biochem.*, **199**, 269-274.
- Baymann, F., Robertson, D.E., Dutton, P.L. and Mäntele, W. (1999) Electrochemical and Spectroscopic Investigations of the Cytochrome *bc1* Complex from *Rhodobacter capsulatus*. *Biochemistry*, **38**, 13188-13199.
- Behr, J., Hellwig, P., Mantele, W. and Michel, H. (1998) Redox Dependent Changes at the Heme Propionates in Cytochrome *c* Oxidase from *Paracoccus denitrificans*: Direct Evidence from FTIR Difference Spectroscopy in Combination with Heme Propionate <sup>13</sup>C Labeling. *Biochemistry*, **37**, 7400-7406.
- Beroza, P. and Case, D.A. (1996) Including Side Chain Flexibility in Continuum Electrostatic Calculations of Protein Titration. *The Journal of Physical Chemistry*, **100**, 20156-20163.
- Berthomieu, C., Marboutin, L., Dupeyrat, F. and Bouyer, P. (2006) Electrochemically induced FTIR difference spectroscopy in the mid- to far infrared (200 microm) domain: A new setup for the analysis of metal-ligand interactions in redox proteins. *Biopolymers*, **82**, 363-367.
- Biel, S., Simon, J., Gross, R., Ruiz, T., Ruitenber, M. and Kröger, A. (2002) Reconstitution of coupled fumarate respiration in liposomes by incorporating the electron transport enzymes isolated from *Wolinella succinogenes*. *European Journal of Biochemistry*, **269**, 1974-1983.
- Bonetti, G., Vecchi, A. and Viappiani, C. (1997) Reaction volume of water formation detected by time-resolved photoacoustics: photoinduced proton transfer between o-nitrobenzaldehyde and hydroxyls in water. *Chemical Physics Letters*, **269**, 268-273.
- Boucher, L.J. and Katz, J.J. (1967) The Infrared Spectra of Metalloporphyrins (4000-160  $\text{cm}^{-1}$ ). *J. Am. Chem. Soc.*, **89**, 1340-1345.
- Boucher, L.J. and Katz, J.J. (2002) The Infrared Spectra of Metalloporphyrins (4000-160  $\text{cm}^{-1}$ ). *Journal of the American Chemical Society*, **89**, 1340-1345.

- Breton, J. (1997) Efficient exchange of the primary quinone acceptor Q(A) in isolated reaction centers of *Rhodospseudomonas viridis*. *Proc Natl Acad Sci U S A*, **94**, 11318-11323.
- Breton, J. and Nabedryk, E. (1996) Protein-quinone interactions in the bacterial photosynthetic reaction center: light-induced FTIR difference spectroscopy of the quinone vibrations. *Biochimica et Biophysica Acta (BBA) - Bioenergetics*, **1275**, 84-90.
- Breton, J., Nabedryk, E., Allen, J.P. and Williams, J.C. (1996) Protein response to Q reduction in wild type and EL(L104) *Rb. Sphaeroides* reaction centers investigated by light-induced FTIR difference spectroscopy. *Biophys. J.*, **70**, A355.
- Breton, J., Thibodeau, D., Berthomieu, C., Mäntele, W., Verméglio, A. and Nabedryk, E. (1991) Probing the primary quinone environment in photosynthetic bacterial reaction centers by light-induced FTIR difference spectroscopy. *FEBS Lett.*, **278**, 257-260.
- Brudler, R., de Groot, H.J.M., van Liemt, W.B.S., Gast, P., Hoff, A.J., Lugtenburg, J. and Gerwert, K. (1995) FTIR spectroscopy shows weak symmetric hydrogen bonding of the QB carbonyl groups in *Rhodobacter sphaeroides* R26 reaction centres. *FEBS Letters*, **370**, 88-92.
- Buchanan, S., Michel, H. and Gerwert, K. (1992) Light-Induced Charge Separation in *Rhodospseudomonas viridis* Reaction Centers Monitored by Fourier-Transform Infrared Difference Spectroscopy: The Quinone Vibrations. *Biochemistry*, **31**, 1314-1322.
- Cartling, B. (1983) Intermediate and stable redox states of Cytochrome c studied by low temperature resonance Raman spectroscopy. *Biophys. J.*, **83**, 191-205.
- Cecchini, G. (2003) Function and structure of complex II of the respiratory chain. *Annu Rev Biochem.*, **72**, 77-109.
- Chirgadze, Y.N., Fedorov, O.V. and Trushina, N.P. (1975) Estimation of amino acid residue side-chain absorption in the infrared spectra of protein solutions in heavy water. *Biopolymers*, **14**, 679-694.
- Chu, H.-A., Gardner, M.T., O'Brien, J.P. and Babcock, G.T. (1999) Low-Frequency Fourier Transform Infrared Spectroscopy of the Oxygen-Evolving and Quinone Acceptor Complexes in Photosystem II. *Biochemistry*, **38**, 4533-4541.
- Corrie, J.E.T., Munasinghe, V.R.N., Trentham, D.R. and Barth, A. (2008) Studies of decarboxylation in photolysis of alpha-carboxy-2-nitrobenzyl (CNB) caged compounds. *Photochem. Photobiol. Sci.*, **7**, 84-97.

- Costa, H., Santos, H., Turner, D. and Xavier, A. (1992) Involvement of a labile axial histidine in coupling electron and proton transfer in *Methylophilus methylotrophus* cytochrome *c*". *Eur J Biochem.*, **208**, 427-433.
- Deacon, G. and Phillips, R. (1980) Relationships between the carbon-oxygen stretching frequencies of carboxylate complexes and the type of carboxylate coordination. *Coord. Chem. Rev.*, **33**, 227-250.
- Deisenhofer, J. and Michel, H. (1989) The photosynthetic reaction centre from the purple bacterium *Rhodospseudomonas viridis*. *EMBO J.*, **8**, 2149-2169.
- Denmark, S.E., Thorarensen, A. and Middleton, D.S. (1996) Tandem [4 + 2]/[3 + 2] Cycloadditions of Nitroalkenes. 9. Synthesis of (-)-Rosmarinecine. *Journal of the American Chemical Society*, **118**, 8266-8277.
- Dollinger, G., Eisenstein, L., Lin, S.L., Nakanishi, K. and Termini, J. (1986) Fourier transform infrared difference spectroscopy of bacteriorhodopsin and its photoproducts regenerated with deuterated tyrosine. *Biochemistry*, **25**, 6524-6533.
- Dörr, S., Schade, U. and Hellwig, P. (2008) Far infrared spectroscopy on hemoproteins: A model compound study from 1800-100 cm<sup>-1</sup>. *Vibrational Spectroscopy*, **47**, 59-65.
- Dörr, S., Schade, U., Hellwig, P. and Ortolani, M. (2007) Characterization of Temperature-Dependent Iron-Imidazole Vibrational Modes in Far Infrared. *The Journal of Physical Chemistry B*, **111**, 14418-14422.
- Dörr, S., Wolpert, M. and Hellwig, P. (2006) Study on the redox state dependent gamma(CH) vibrational modes of the *c*-type heme. *Biopolymers*, **82**, 349-352.
- Dunbrack, R.L. and Cohen, F.E. (1997) Bayesian statistical analysis of protein side-chain rotamer preferences. *Protein Sci.* , **6**, 1661-1681.
- Dunbrack, R.L. and Karplus, M. (1994) Conformational analysis of the backbone-dependent rotamer preferences of protein sidechains. *Nature Structural Biology* **1**, 334 - 340.
- Dutton, P. (1978) Redox Potentiometry: Determination of Midpoint Potentials of Oxidation-Reduction Components in Biological Electron Transfer Systems. *Methods in enzymology*, **54**, 411-435.
- Džafic, E., Klein, O., Screpanti, E., Hunte, C. and Mäntele, W. (2009) Flexibility and dynamics of NhaA Na<sup>+</sup>/H<sup>+</sup>-antiporter of *Escherichia coli* studied by Fourier transform infrared spectroscopy. *Spectrochimica Acta Part A: Molecular and Biomolecular Spectroscopy*, **72**, 102-109.
- Enger, E.D. and Frederick C. (2003) Concepts in Biology, 10th Ed. *McGraw-Hill*

- Ermiler, U., Fritsch, G., Buchanan, S. and Michel, H. (1994) Structure of the photosynthetic reaction centre from *Rhodobacter sphaeroides* at 2.65 Å resolution: cofactors and protein-cofactor interactions. *Structure*, **2**, 925-936.
- Fabian, H. and Mäntele, W. (2002) Infrared spectroscopy of Proteins. *Handbook of Vibrational Spectroscopy* (Chalmers, J. M., and Griffiths, P. R., Eds.) John Wiley & Sons, Ltd., Chichester, **5**, 3399-3425.
- Franzen, S. and Boxer, S.G. (1997) On the Origin of Heme Absorption Band Shifts and Associated Protein Structural Relaxation in Myoglobin Following Flash Photolysis. *Journal of Biological Chemistry*, **272**, 9655-9660.
- Franzen, S., Boxer, S.G., Dyer, R.B. and Woodruff, W.H. (2000) Resonance Raman Studies of Heme Axial Ligation in H93G Myoglobin. *J. Phys. Chem. B*, **104**, 10359-10367.
- Franzen, S., Wallace-Williams, S.E. and Shreve, A.P. (2002) Heme Charge-Transfer Band III Is Vibronically Coupled to the Soret Band. *Journal of the American Chemical Society*, **124**, 7146-7155.
- Frey, P., Whitt, S. and Tobin, J. (1994) A low-barrier hydrogen bond in the catalytic triad of serine proteases. *Science*, **264**, 1927-1930.
- Gee, K.R., Wieboldt, R. and Hess, G.P. (2002) Synthesis and Photochemistry of a New Photolabile Derivative of GABA-Neurotransmitter Release and Receptor Activation in the Microsecond Time Region. *Journal of the American Chemical Society*, **116**, 8366-8367.
- Geisler, V., Ullmann, R. and Kröger, A. (1994) The direction of the proton exchange associated with the redox reactions of menaquinone during electron transport in *Wolinella succinogenes*. *Biochimica et Biophysica Acta (BBA) - Bioenergetics*, **1184**, 219-226.
- Geißler, D., Antonenko, Y.N., Schmidt, R., Keller, S., Krylova, O.O., Wiesner, B., Bendig, J., Pohl, P. and Hagen, V. (2005) (Coumarin-4-yl)methyl Esters as Highly Efficient, Ultrafast Phototriggers for Protons and Their Application to Acidifying Membrane Surfaces<sup>13</sup>. *Angewandte Chemie International Edition*, **44**, 1195-1198.
- Georgescu, R.E., Alexov, E.G. and Gunner, M.R. (2002) Combining conformational flexibility and continuum electrostatics for calculating pKa's in proteins. *Biophys J.*, **83**, 1731-1748.
- Gerwert, K. (1993) Molecular reaction mechanisms of proteins as monitored by time-resolved FTIR spectroscopy. *Curr. Opin. Struct. Biol.*, **3**, 769-773.

- Goormaghtigh, E., Cabiaux, V. and Ruyschaert, J. (1994) Determination of soluble and membrane protein structure by Fourier transform infrared spectroscopy. III. Secondary structures. *Subcell Biochem.*, **23**, 405-450.
- Görne-Tschelnokow, U., Hucho, F., Naumann, D., Barth, A. and Mäntele, W. (1992) Fourier transform infrared (FTIR) spectroscopic investigation of the nicotinic acetylcholine receptor (nAChR). Investigation of agonist binding and receptor conformational changes by flash-induced release of 'caged' carbamoylcholine. *FEBS Lett.*, **309**, 213-217.
- Goulden, J.D.S. (1959) Infra-red spectroscopy of aqueous solutions. *Spectrochimica Acta*, **15**, 657-671.
- Gourion-Arsiquaud, S., Chevance, S., Bouyer, P., Garnier, L., Montillet, J.-L., Bondon, A. and Berthomieu, C. (2005) Identification of a Cd<sup>2+</sup>- and Zn<sup>2+</sup>-Binding Site in Cytochrome *c* Using FTIR Coupled to an ATR Microdialysis Setup and NMR Spectroscopy. *Biochemistry*, **44**, 8652-8663.
- Gray, H. and Winkler, J. (1996) Electron Transfer in Proteins. *Annu. Rev. Biochem.*, **65**, 537-561.
- Gries, C., Hellwig, P. and Mäntele, W. (1997) Spectroelectrochemical investigations of cytochrome *c* oxidase on chemically modified semitransparent electrodes by FTIR-spectroscopy. *Spectroscopy of Biological Molecules: Modern Trends* (Carmona, P., Navarro, R., and Hernanz, A., Eds.), Kluwer, Dordrecht, The Netherlands, 193-194
- Griffiths, P.R. (1986) Fourier Transform Infrared Spectrometry. *John Wiley & Sons, Inc.*
- Guest, C.R. and Noe, L.J. (1988) Picosecond absorption studies on the photodissociation of alpha- and beta-nitrosyl hemoglobin monomers. *Biophysical Journal*, **54**, 731-736.
- Gunner, M.R. and Alexov, E. (2000) A pragmatic approach to structure based calculation of coupled proton and electron transfer in proteins. *Biochimica et Biophysica Acta (BBA) - Bioenergetics*, **1458**, 63-87.
- Haas, A.H. and Lancaster, C.R.D. (2004) Calculated Coupling of Transmembrane Electron and Proton Transfer in Dihemic Quinol:Fumarate Reductase. *Biophysical Journal*, **87**, 4298-4315.
- Haas, A.H., Sauer, U.S., Gross, R., Simon, J., Mäntele, W. and Lancaster, C.R.D. (2005) FTIR Difference Spectra of *Wolinella succinogenes* Quinol:Fumarate Reductase Support a Key Role of Glu C180 within the "E-Pathway Hypothesis" of Coupled Transmembrane Electron and Proton Transfer. *Biochemistry*, **44**, 13949-13961.

- Hägerhäll, C. (1997) Succinate: quinone oxidoreductases: Variations on a conserved theme. *Biochimica et Biophysica Acta (BBA) - Bioenergetics*, **1320**, 107-141.
- Hägerhäll, C., Friden, H., Aasa, R. and Hederstedt, L. (1995) Transmembrane Topology and Axial Ligands to Hemes in the Cytochrome *b* Subunit of *Bacillus subtilis* Succinate:Menaquinone Reductase. *Biochemistry*, **34**, 11080-11089.
- Hagihara, B. and Iizuka, T. (1971) Studies on Low Temperature Spectra of Respiratory Pigments: I. Measurement of Absorption Spectra between Liquid Helium and Room Temperatures. *J. Biochem.*, **69**, 355-362.
- Hagihara, B., Oshino, R. and Iizuka, T. (1974) Studies on Low Temperature Spectra of Respiratory Pigments: II. Spectra of Cytochromes in Respiratory Systems between Liquid Helium and Room Temperatures. *J. Biochem.*, **75**, 45-51.
- Hansen, K.C., Schultz, B.E., Wang, G. and Chan, S.I. (2000) Reaction of *Escherichia coli* cytochrome *bo3* and mitochondrial cytochrome *bc1* with a photoreleasable decylubiquinol. *Biochimica et Biophysica Acta (BBA) - Bioenergetics*, **1456**, 121-137.
- Hasegawa, K., Ono, T.-a. and Noguchi, T. (2000) Vibrational Spectra and Ab Initio DFT Calculations of 4-Methylimidazole and Its Different Protonation Forms: Infrared and Raman Markers of the Protonation State of a Histidine Side Chain. *The Journal of Physical Chemistry B*, **104**, 4253-4265.
- Hays, A.-M.A., Vassiliev, I.R., Golbeck, J.H. and Debus, R.J. (1998) Role of D1-His190 in Proton-Coupled Electron Transfer Reactions in Photosystem II: A Chemical Complementation Study. *Biochemistry*, **37**, 11352-11365.
- Hellwig, P., Behr, J., Ostermeier, C., Richter, O.-M.H., Pfitzner, U., Odenwald, A., Ludwig, B., Michel, H. and Mantele, W. (1998) Involvement of Glutamic Acid 278 in the Redox Reaction of the Cytochrome *c* Oxidase from *Paracoccus denitrificans* Investigated by FTIR Spectroscopy. *Biochemistry*, **37**, 7390-7399.
- Hellwig, P., Mogi, T., Tomson, F.L., Gennis, R.B., Iwata, J., Miyoshi, H. and Mantele, W. (1999) Vibrational Modes of Ubiquinone in Cytochrome *bo3* from *Escherichia coli* Identified by Fourier Transform Infrared Difference Spectroscopy and Specific <sup>13</sup>C Labeling. *Biochemistry*, **38**, 14683-14689.
- Hellwig, P., Rost, B., Kaiser, U., Ostermeier, C., Michel, H. and Mantele, W. (1996) Carboxyl group protonation upon reduction of the *Paracoccus denitrificans* cytochrome *c* oxidase: direct evidence by FTIR spectroscopy. *FEBS Letters*, **385**, 53-57.
- Hellwig, P., Scheide, D., Bungert, S., Mantele, W. and Friedrich, T. (2000) FT-IR Spectroscopic Characterization of NADH:Ubiquinone Oxidoreductase (Complex I) from *Escherichia coli*: Oxidation of FeS Cluster N2 is Coupled with the

- Protonation of an Aspartate or Glutamate Side Chain. *Biochemistry*, **39**, 10884-10891.
- Herres, W. and Gronholz, J. (1985) Part 1: Data acquisition and Fourier transformation, in Understanding FT-IR data processing. *Dr. Alfred Hüthig Publishers, Heidelberg, Germany*.
- Hienerwadel, R., Boussac, A., Breton, J., Diner, B.A. and Berthomieu, C. (1997) Fourier Transform Infrared Difference Spectroscopy of Photosystem II Tyrosine D Using Site-Directed Mutagenesis and Specific Isotope Labeling. *Biochemistry*, **36**, 14712-14723.
- Hienerwadel, R., Grzybek, S., Fogel, C., Kreutz, W., Okamura, M.Y., Paddock, M.L., Breton, J., Navedryk, E. and Maentele, W. (1995) Protonation of Glu L212 following QB- Formation in the Photosynthetic Reaction Center of *Rhodobacter sphaeroides*: Evidence from Time-Resolved Infrared Spectroscopy. *Biochemistry*, **34**, 2832-2843.
- Hirst, J., Wilcox, S.K., Williams, P.A., Blankenship, J., McRee, D.E. and Goodin, D.B. (2001) Replacement of the Axial Histidine Ligand with Imidazole in Cytochrome *c* Peroxidase. 1. Effects on Structure. *Biochemistry*, **40**, 1265-1273.
- Huber, R., Satzger, H., Zinth, W. and Wachtveitl, J. (2001) Noncollinear optical parametric amplifiers with output parameters improved by the application of a white light continuum generated in CaF<sub>2</sub>. *Optics Communications*, **194**, 443-448.
- Iizuka, T., Kanegasaki, S., Makino, R., Tanaka, T. and Ishimura, Y. (1985) Studies on Neutrophil *b*-Type Cytochrome in Situ by Low Temperature Absorption Spectroscopy. *J. Biol. Chem.*, **260**, 12049-12053.
- Iwaki, M., Yakovlev, G., Hirst, J., Osyczka, A., Dutton, P.L., Marshall, D. and Rich, P.R. (2005) Direct Observation of Redox-Linked Histidine Protonation Changes in the Iron-Sulfur Protein of the Cytochrome *bc*<sub>1</sub> Complex by ATR-FTIR Spectroscopy. *Biochemistry*, **44**, 4230-4237.
- Janko, K. and Reichert, J. (1987) Proton concentration jumps and generation of transmembrane pH-gradients by photolysis of 4-formyl-6-methoxy-3-nitrophenoxyacetic acid. *Biochimica et Biophysica Acta (BBA) - Biomembranes*, **905**, 409-416.
- Jongeward, K., Magde, D., Taube, D. and Traylor, T. (1988) Picosecond kinetics of cytochromes *b*<sub>5</sub> and *c*. *J. Biol. Chem.*, **263**, 6027-6030.
- Jongeward, K.A., Marsters, J.C., Mitchell, M.J., Magde, D. and Sharma, V.S. (1986) Picosecond geminate recombination of nitrosylmyoglobins. *Biochemical and Biophysical Research Communications*, **140**, 962-966.



- Kaplan, J. and Ellis-Davies, G. (1988) Photolabile chelators for the rapid photorelease of divalent cations. *PNAS*, **85**, 6571-6575.
- Kaplan, J., Forbush, B. and Hoffman, J. (1978) Rapid Photolytic Release of Adenosine 5'-Triphosphate from a Protected Analogue: Utilization by the Na:K Pump of Human Red Blood Cell Ghosts. *Biochemistry*, **17**, 1929-1935.
- Karp, G. (2008) Cell and Molecular Biology, 5th Ed. *Wiley*.
- Kimura, Y., Mizusawa, N., Ishii, A., Yamanari, T. and Ono, T.-a. (2003) Changes of Low-Frequency Vibrational Modes Induced by Universal <sup>15</sup>N- and <sup>13</sup>C-Isotope Labeling in S2/S1 FTIR Difference Spectrum of Oxygen-Evolving Complex. *Biochemistry*, **42**, 13170-13177.
- Körtner, C., Lauterbach, F., Tripier, D., Unden, G. and Kröger, A. (1990) *Wolinella succinogenes* fumarate reductase contains a diheme cytochrome *b*. *Molec. Microbiology*, **4**, 855-860.
- Kröger, A., Biel, S., Simon, J., Gross, R., Unden, G. and Lancaster, C.R.D. (2002) Fumarate respiration of *Wolinella succinogenes*: enzymology, energetics and coupling mechanism. *Biochimica et Biophysica Acta (BBA) - Bioenergetics*, **1553**, 23-38.
- Kröger, A., Geisler, V., Lemma, E., Theis, F. and Lenger, R. (1992) Bacterial fumarate respiration. *Arch Microbiol.*, **158**, 311–314.
- Kröger, A. and Innerhofer, A. (1976) The Function of the *b* Cytochromes in the Electron Transport from Formate to Fumarate of *Vibrio succinogenes*. *European Journal of Biochemistry*, **69**, 497-506.
- Lancaster, C. (1998) Ubiquinone reduction and protonation in photosynthetic reaction centres from *Rhodospseudomonas viridis*: X-ray structures and their functional implications. *Biochim. Biophys. Acta.*, **1365**, 143-150.
- Lancaster, C. (2004) Respiratory Chain Complex II and Succinate:Quinone Oxidoreductases. *Encyclopedia of Biological Chemistry (Lennarz, W.J., Lane, M.D., eds.)*, Elsevier, Oxford, U.K., **3**, 681-687.
- Lancaster, C., Ermler, U. and Michel, H. (1995) *Anoxygenic Photosynthetic Bacteria (Blankenship, R.E., Madigan, M.T. and Bauer, C.E., eds.)*, Kluwer Academic, Dordrecht, 503-526.
- Lancaster, C., Groß, R., Haas, A., Ritter, M., Mäntele, W., Simon, J. and Kröger, A. (2000) Essential role of Glu-C66 for menaquinol oxidation indicates transmembrane electrochemical potential generation by *Wolinella succinogenes* fumarate reductase. *PNAS*, **97**, 13051-13056.

- Lancaster, C., Haas, A., Madej, M. and Mileni, M. (2006) Recent progress on obtaining theoretical and experimental support for the “E-pathway hypothesis” of coupled transmembrane electron and proton transfer in dihaem-containing quinol:fumarate reductase. *Biochim. Biophys. Acta, Bioenerg.*, **1757**, 988-995.
- Lancaster, C.R.D. (2001) Succinate:quinone oxidoreductases. *Handbook of Metalloproteins* (Wieghardt, K., Huber, R., Poulos, T., Messerschmidt, A., eds.), Wiley, Chichester, U.K., **1**, 379-401.
- Lancaster, C.R.D. (2002) *Wolinella succinogenes* quinol:fumarate reductase--2.2-Å resolution crystal structure and the E-pathway hypothesis of coupled transmembrane proton and electron transfer. *Biochimica et Biophysica Acta (BBA) - Biomembranes*, **1565**, 215-231.
- Lancaster, C.R.D. (2003) The structure of *Wolinella succinogenes* quinol:fumarate reductase and its relevance to the superfamily of succinate:quinone oxidoreductases. *Adv. Prot. Chem.*, **63**, 131-149.
- Lancaster, C.R.D., Groß, R. and Simon, J. (2001) A third crystal form of *Wolinella succinogenes* quinol:fumarate reductase reveals domain closure at the site of fumarate reduction. *European Journal of Biochemistry*, **268**, 1820-1827.
- Lancaster, C.R.D., Herzog, E., Juhnke, H.D., Madej, M.G., Mueller, F.G., Paul, R. and Schleidt, P.G. (2008) Electroneutral and electrogenic catalysis by dihaem-containing succinate:quinone oxidoreductases. *Biochemical Society Transactions*, **36**, 996-1000.
- Lancaster, C.R.D., Kröger, A., Auer, M. and Michel, H. (1999) Structure of fumarate reductase from *Wolinella succinogenes* at 2.2Å resolution. *Nature*, **402**, 377-385.
- Lancaster, C.R.D., Sauer, U.S., Groß, R., Haas, A.H., Graf, J., Schwalbe, H., Mäntele, W., Simon, J. and Madej, M.G. (2005) Experimental support for the “E pathway hypothesis” of coupled transmembrane e<sup>-</sup> and H<sup>+</sup> transfer in dihemic quinol:fumarate reductase. *PNAS*, **102**, 18860–18865.
- Lancaster, C.R.D. and Simon, J. (2002) Succinate:quinone oxidoreductases from  $\epsilon$ -proteobacteria. *Biochimica et Biophysica Acta (BBA) - Bioenergetics*, **1553**, 84-101.
- Lauterbach, F., Körtner, C., Albracht, S.P., Unden, G. and Kröger, A. (1990) The fumarate reductase operon of *Wolinella succinogenes*. Sequence and expression of the frdA and frdB genes. *Arch Microbiol.*, **154**, 386-393.
- Lemma, E., Hägerhäll, C., Geisler, V., Brandt, U., von Jagow, G. and Kröger, A. (1991) Reactivity of the *Bacillus subtilis* succinate dehydrogenase complex with quinones. *Biochimica et Biophysica Acta (BBA) - Bioenergetics*, **1059**, 281-285.

- Lenz, M.O., Huber, R., Schmidt, B., Gilch, P., Kalmbach, R., Engelhard, M. and Wachtveitl, J. (2006) First Steps of Retinal Photoisomerization in Proteorhodopsin. *Biophysical Journal*, **91**, 255-262.
- Louro, R.O., Catarino, T., Salgueiro, C.A., LeGall, J. and Xavier, A.n.V. (1996) Redox-Bohr effect in the tetrahaem cytochrome *c*<sub>3</sub> from *Desulfovibrio vulgaris*: a model for energy transduction mechanisms. *Journal of Biological Inorganic Chemistry*, **1**, 34-38.
- Ludovici, C., Fröhlich, R., Vogtt, K., Mamat, B. and Lübben, M. (2002) Caged O<sub>2</sub>: Reaction of cytochrome *bo*<sub>3</sub> oxidase with photochemically released dioxygen from a cobalt peroxo complex. *European Journal of Biochemistry*, **269**, 2630-2637.
- Lübben, M. and Gerwert, K. (1996) Redox FTIR difference spectroscopy using caged electrons reveals contributions of carboxyl groups to the catalytic mechanism of haemcopper oxidases. *FEBS Letters*, **397**, 303-307.
- Madej, M.G., Müller, F.G., Ploch, J. and Lancaster, C.R.D. (2009) Limited reversibility of transmembrane proton transfer assisting transmembrane electron transfer in a dihaem-containing succinate:quinone oxidoreductase. *Biochimica et Biophysica Acta (BBA) - Bioenergetics*, **1787**, 593-600.
- Madej, M.G., Nasiri, H.R., Hilgendorff, N.S., Schwalbe, H. and Lancaster, C.R.D. (2006a) Evidence for transmembrane proton transfer in a dihaem-containing membrane protein complex. *EMBO J.*, **25**, 4963-4970.
- Madej, M.G., Nasiri, H.R., Hilgendorff, N.S., Schwalbe, H., Unden, G. and Lancaster, C.R.D. (2006b) Experimental evidence for proton motive force-dependent catalysis by the diheme-containing succinate:menaquinone oxidoreductase from the gram-positive bacterium *Bacillus licheniformis*. *Biochemistry*, **45**, 15049-15055.
- Mäntele, W. (1993) Reaction-induced infrared difference spectroscopy for the study of protein function and reaction mechanisms. *Trends in Biochemical Sciences*, **18**, 197-202.
- Mäntele, W. (1996) Infrared and Fourier transform infrared spectroscopy. *Photosynthesis (Hoff, A. J., and Ames, J., Eds.)*, Kluwer, Dordrecht, The Netherlands., pp. 137-160.
- Marboutin, L., Boussac, A. and Berthomieu, C. (2006) Redox infrared markers of the heme and axial ligands in microperoxidase: bases for the analysis of c-type cytochromes. *Journal of Biological Inorganic Chemistry*, **11**, 811-823.
- Marboutin, L., Desbois, A. and Berthomieu, C. (2009) Low-Frequency Heme, Iron-Ligand, and Ligand Modes of Imidazole and Imidazolate Complexes of Iron Protoporphyrin and Microperoxidase in Aqueous Solution. An Analysis by Far-

- Infrared Difference Spectroscopy. *The Journal of Physical Chemistry B*, **113**, 4492-4499.
- Marriott, G. (1998) Caged Compounds. *Methods in Enzymology*, **291**.
- Martin, C.T., Scholes, C.P. and Chan, S.I. (1985) The identification of histidine ligands to cytochrome *a* in cytochrome *c* oxidase. *Journal of Biological Chemistry*, **260**, 2857-2861.
- Martin, J. and Vos, M. (1992) Femtosecond Biology. *Annual Review of Biophysics and Biomolecular Structure*, **21**, 199-222.
- McMahon, B.H., Fabian, M., Tomson, F., Causgrove, T.P., Bailey, J.A., Rein, F.N., Dyer, R.B., Palmer, G., Gennis, R.B. and Woodruff, W.H. (2004) FTIR studies of internal proton transfer reactions linked to inter-heme electron transfer in bovine cytochrome *c* oxidase. *Biochimica et Biophysica Acta (BBA) - Bioenergetics*, **1655**, 321-331.
- Meganathan, R. and Coffell, R. (1985) Identity of the quinone in *Bacillus alcalophilus*. *J. Bacteriol.*, **164**, 911-913.
- Mesu, J.G., Visser, T., Soulimani, F. and Weckhuysen, B.M. (2005) Infrared and Raman spectroscopic study of pH-induced structural changes of l-histidine in aqueous environment. *Vibrational Spectroscopy*, **39**, 114-125.
- Mezzetti, A. and Leibl, W. (2005) Investigation of ubiquinol formation in isolated photosynthetic reaction centers by rapid-scan Fourier transform IR spectroscopy. *European Biophysics Journal*, **34**, 921-936.
- Mezzetti, A., Leibl, W., Breton, J. and Navedryk, E. (2003) Photoreduction of the quinone pool in the bacterial photosynthetic membrane: identification of infrared marker bands for quinol formation. *FEBS Letters*, **537**, 161-165.
- Mileni, M., Haas, A.H., Mantele, W., Simon, J. and Lancaster, C.R.D. (2005) Probing Heme Propionate Involvement in Transmembrane Proton Transfer Coupled to Electron Transfer in Dihemic Quinol:Fumarate Reductase by <sup>13</sup>C-Labeling and FTIR Difference Spectroscopy. *Biochemistry*, **44**, 16718-16728.
- Mileni, M., MacMillan, F., Tziatzios, C., Zwicker, K., Haas, A.H., Mantele, W., Simon, J. and Lancaster, C.R.D. (2006) Heterologous production in *Wolinella succinogenes* and characterization of the quinol:fumarate reductase enzymes from *Helicobacter pylori* and *Campylobacter jejuni*. *Biochem J.*, **395**, 191-201.
- Mitchell, P. (1961) Coupling of Phosphorylation to Electron and Hydrogen Transfer by a Chemi-Osmotic type of Mechanism. *Nature*, **191**, 144-148.

- Moss, D., Nabedryk, E., Breton, J. and Mäntele, W. (1990) Redox-linked conformational changes in proteins detected by a combination of infrared spectroscopy and protein electrochemistry. *European Journal of Biochemistry*, **187**, 565-572.
- Nabedryk, E., Breton, J., Hienerwadel, R., Fogel, C., Maentele, W., Paddock, M.L. and Okamura, M.Y. (1995) Fourier Transform Infrared Difference Spectroscopy of Secondary Quinone Acceptor Photoreduction in Proton Transfer Mutants of *Rhodobacter sphaeroides*. *Biochemistry*, **34**, 14722-14732.
- Neises, B. and Steglich, W. (1985) Esterification of Carboxylic Acids with Dicyclohexyl-Carbodiimide/4-Dimethylaminopyridine: tert-Butyl Ethyl Fumarate. *Org. Synth.*, **63**, 183-187.
- Nevskaya, N.A. and Chirgadze, Y.N. (1976) Infrared spectra and resonance interactions of amide-I and II vibrations of alpha-helix. *Biopolymers*, **15**, 637-648.
- Nicholls, A. and Honig, B. (1991) A rapid finite difference algorithm, utilizing successive over-relaxation to solve the Poisson-Boltzmann equation. *Journal of Computational Chemistry*, **12**, 435-445.
- Noguchi, T., Inoue, Y. and Tang, X.-S. (1999) Structure of a Histidine Ligand in the Photosynthetic Oxygen-Evolving Complex As Studied by Light-Induced Fourier Transform Infrared Difference Spectroscopy. *Biochemistry*, **38**, 10187-10195.
- Ohnishi, T., Moser, C.C., Page, C.C., Dutton, P.L. and Yano, T. (2000) Simple redoxlinked proton-transfer design: new insights from structures of quinol-fumarate reductase. *Structure*, **8**, R23-R32.
- Page, C.C., Moser, C.C., Chen, X. and Dutton, P.L. (1999) Natural engineering principles of electron tunnelling in biological oxidation-reduction. *Nature*, **402**, 47-52.
- Papa, S. (1976) Proton translocation reactions in the respiratory chains. *Biochimica et Biophysica Acta (BBA) - Reviews on Bioenergetics*, **456**, 39-84.
- Papa, S., Capitanio, N. and Villani, G. (1998) A cooperative model for protonmotive heme-copper oxidases. The role of heme a in the proton pump of cytochrome c oxidase. *FEBS Letters*, **439**, 1-8.
- Papa, S., Lorusso, M. and Capitanio, N. (1994) Mechanistic and phenomenological features of proton pumps in the respiratory chain of mitochondria. *J Bioenerg Biomembr.*, **26**, 609-618.
- Pelliccioli, A. and Wirz, J. (2002) Photoremovable protecting groups: reaction mechanisms and applications. *Photochem Photobiol Sci.*, **1**, 441-458.
- Phan, H. (2009) Fundamental Infrared Spectroscopy.  
[www.guibord.com/french/online\\_articles/electronics](http://www.guibord.com/french/online_articles/electronics), **TN-100**, 1-8.

- Rahmelow, K., Hübner, W. and Ackermann, T. (1998) Infrared Absorbances of Protein Side Chains. *Analytical Biochemistry*, **257**, 1-11.
- Roepe, P., Ahl, P.L., Das Gupta, S.K., Herzfeld, J. and Rothschild, K.J. (2002) Tyrosine and carboxyl protonation changes in the bacteriorhodopsin photocycle. 1. M412 and L550 intermediates. *Biochemistry*, **26**, 6696-6707.
- Rothschild, K.J. (1992) FTIR difference spectroscopy of bacteriorhodopsin: Toward a molecular model. *Journal of Bioenergetics and Biomembranes*, **24**, 147-167.
- Saraste, M. (1999) Oxidative phosphorylation at the fin de siècle. *Science*, **283**, 1488-1493.
- Schaper, K., Mobarekeh, S., Abdollah, M. and Grewer, C. (2002) Synthesis and Photophysical Characterization of a New, Highly Hydrophilic Caging Group. *European Journal of Organic Chemistry*, **2002**, 1037-1046.
- Shelnutt, J.A. (1981) A simple interpretation of Raman excitation spectra of metalloporphyrins. *The Journal of Chemical Physics*, **74**, 6644-6657.
- Simon, J., Gross, R., Ringel, M., Schmidt, E. and Kröger, A. (1998) Deletion and site-directed mutagenesis of the *Wolinella succinogenes* fumarate reductase operon. *European Journal of Biochemistry*, **251**, 418-426.
- Spassov, V.Z., Luecke, H., Gerwert, K. and Bashford, D. (2001) pKa calculations suggest storage of an excess proton in a hydrogen-bonded water network in bacteriorhodopsin. *Journal of Molecular Biology*, **312**, 203-219.
- Tackett, J.E. (1989) FT-IR Characterization of Metal Acetates in Aqueous Solution. *Appl. Spectrosc.*, **43**, 483-489.
- Uden, G., Albracht, S. and Kröger, A. (1984) Redox potentials and kinetic properties of fumarate reductase complex from *Vibrio succinogenes*. Redox potentials and kinetic properties of fumarate reductase complex from *Vibrio succinogenes*. *Biochimica et Biophysica Acta*, **767**, 460-469.
- Uden, G., Hackenberg, H. and Kröger, A. (1980) Isolation and functional aspects of the fumarate reductase involved in the phosphorylative electron transport of *Vibrio succinogenes*. *Biochimica et Biophysica Acta*, **591**, 275-288.
- VanAken, T., Foxall-VanAken, S., Castleman, S. and Ferguson-Miller, S. (1986) Alkyl glycoside detergents: synthesis and applications to the study of membrane proteins. *Methods Enzymol.*, **125**, 27-35.
- Veiseha, M., Veiseha, O., Martinb, M.C., Bertozzic, C. and Zhanga, M. (2007) Single-cell-based sensors and synchrotron FTIR spectroscopy: A hybrid system towards bacterial detection. *Biosensors and Bioelectronics*, **23**, 253-260.

- Venyaminov, S. and Kalnin, N. (1990a) Quantitative IR spectrophotometry of peptide compounds in water (H<sub>2</sub>O) solutions. II. Amide absorption bands of polypeptides and fibrous proteins in alpha-, beta-, and random coil conformations. *Biopolymers*, **30**, 1259-1271.
- Venyaminov, S.Y. and Kalnin, N.N. (1990b) Quantitative IR spectrophotometry of peptide compounds in water solutions. I. Spectral parameters of amino acid residue absorption bands. *Biopolymers*, **30**, 1243-1257.
- Verkhovsky, M.I., Jasaitis, A. and Wikström, M. (2001) Ultrafast haem-haem electron transfer in cytochrome *c* oxidase. *Biochimica et Biophysica Acta (BBA) - Bioenergetics*, **1506**, 143-146.
- Viappiani, C., Abbruzzetti, S., Small, J.R., Libertini, L.J. and Small, E.W. (1998) An experimental methodology for measuring volume changes in proton transfer reactions in aqueous solutions. *Biophysical Chemistry*, **73**, 13-22.
- Voet, D., Voet, J.G. and Pratt, C.W. (1999) Oxidative phosphorylation. *in Fundamentals of Biochemistry*.
- Vos, M.H. and Martin, J.-L. (1999) Femtosecond processes in proteins. *Biochimica et Biophysica Acta (BBA) - Bioenergetics*, **1411**, 1-20.
- Walker, J.W., McCray, J.A. and Hess, G.P. (2002) Photolabile protecting groups for an acetylcholine receptor ligand. Synthesis and photochemistry of a new class of o-nitrobenzyl derivatives and their effects on receptor function. *Biochemistry*, **25**, 1799-1805.
- Wang, W., Ye, X., Demidov, A.A., Rosca, F., Sjodin, T., Cao, W., Sheeran, M. and Champion, P.M. (2000) Femtosecond Multicolor Pump-Probe Spectroscopy of Ferrous Cytochrome *c*. *The Journal of Physical Chemistry B*, **104**, 10789-10801.
- Wilson, D.F. and Leigh, J.S. (1972) Heme--Heme interaction in cytochrome *c* oxidase in situ as measured by EPR spectroscopy. *Archives of Biochemistry and Biophysics*, **150**, 154-163.
- Wolpert, M. and Hellwig, P. (2006) Infrared spectra and molar absorption coefficients of the 20 alpha amino acids in aqueous solutions in the spectral range from 1800 to 500 cm<sup>-1</sup>. *Spectrochimica Acta Part A: Molecular and Biomolecular Spectroscopy*, **64**, 987-1001.
- Wolpert, M., Maneg, O., Ludwig, B. and Hellwig, P. (2004) Characterization of the CuA center in the cytochrome *c* oxidase from *Thermus thermophilus* for the spectral range 1800-500 cm<sup>-1</sup> with a combined electrochemical and Fourier transform infrared spectroscopic setup. *Biopolymers*, **74**, 73-76.

- 
- Xerri, B., Flament, J.-P., Petitjean, H., Berthomieu, C. and Berthomieu, D. (2009) Vibrational Modeling of Copper-Histamine Complexes: Metal-Ligand IR Modes Investigation. *The Journal of Physical Chemistry B*, **113**, 15119-15127.
- You, T.J. and Bashford, D. (1995) Conformation and hydrogen ion titration of proteins: a continuum electrostatic model with conformational flexibility. *Biophysical Journal*, **69**, 1721-1733.
- Zhu, L., Sage, J. and Champion, P. (1994) Observation of coherent reaction dynamics in heme proteins. *Science*, **266**, 629-632.



## 7 Appendix

**Table 9** The simulated pH dependence of the occupancy of Glu<sup>0</sup> C180 (cumulative occupancy of all neutral conformers) as a function of the four considered heme redox states.

	5	5.5	6	6.5	7	7.5	8	8.5	9	9.5
$b_D^{ox} b_P^{ox}$	0.983	0.951	0.858	0.685	0.466	0.266	0.054	0.000	0.000	0.000
$b_D^{red} b_P^{ox}$	1.000	1.000	1.000	1.000	1.000	0.972	0.905	0.754	0.505	0.272
$b_D^{ox} b_P^{red}$	1.000	1.000	1.000	0.970	0.905	0.786	0.606	0.329	0.138	0.014
$b_D^{red} b_P^{red}$	1.000	1.000	1.000	1.000	1.000	1.000	1.000	0.978	0.922	0.821

**Table 10** The simulated pH dependence of the difference in occupancy of Glu<sup>0</sup> C180 (cumulative occupancy of all neutral conformers) as a function of the four considered heme redox states.

	5	5.5	6	6.5	7	7.5	8	8.5	9	9.5
$b_D^{ox} b_P^{red}$ - $minus- b_D^{ox} b_P^{ox}$	0.017	0.049	0.142	0.285	0.484	0.520	0.552	0.329	0.138	0.014
$b_D^{red} b_P^{ox}$ - $minus- b_D^{ox} b_P^{ox}$	0.017	0.049	0.142	0.315	0.534	0.706	0.851	0.754	0.505	0.272
$b_D^{red} b_P^{red}$ - $minus- b_D^{ox} b_P^{ox}$	0.017	0.049	0.142	0.315	0.534	0.734	0.946	0.978	0.922	0.821

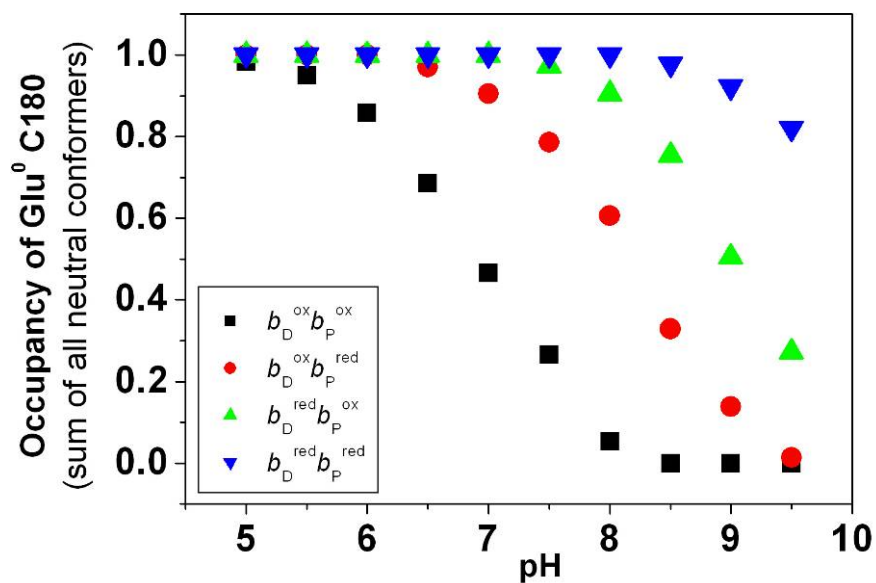


**Figure 46** The simulated pH dependence of the occupancy of Glu<sup>0</sup> C180 (cumulative occupancy of all neutral conformers) as a function of the four considered heme redox states.

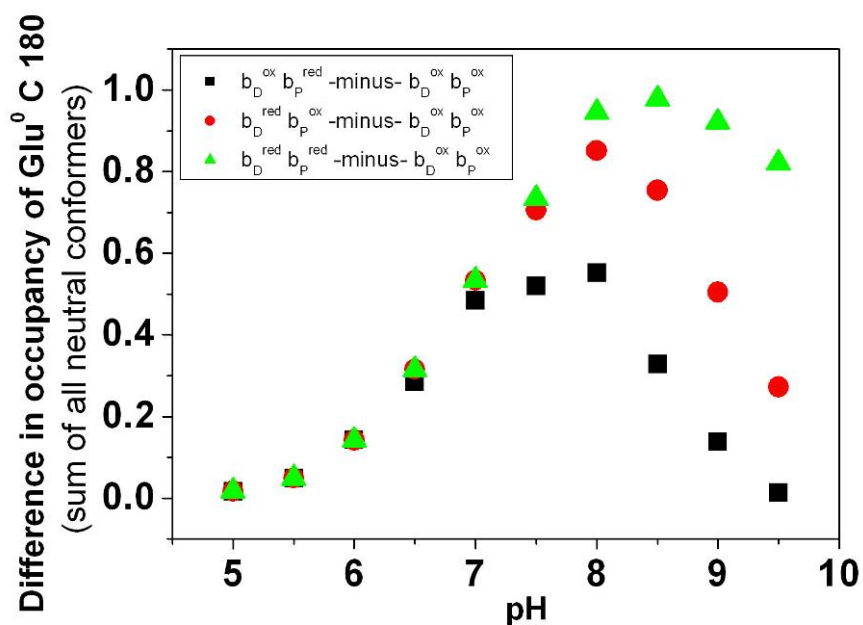


**Figure 47** The simulated pH dependence of the difference in occupancy of Glu<sup>0</sup> C180 (cumulative occupancy of all neutral conformers) as a function of the four considered heme redox states.

## 8 Acknowledgements

I would like to express my extreme gratitude to my supervisor Prof. Roy Lancaster who gave me the opportunity, resources, and excellent supervision for the work for this thesis. I am deeply thankful to him for all the valuable discussions regarding the projects and taking them to new directions, when needed.

I am very thankful to Prof. Hartmut Michel for giving me the opportunity to work in his department.

I am grateful to Prof. Josef Wachtveitl from Johann Wolfgang Goethe University for his precious support and for taking the responsibility of being my university supervisor.

I would like to thank Prof. Werner Mäntele from Johann Wolfgang Goethe University for helping me to carry out all the FTIR experiments and for all the fruitful discussions and teachings.

I thank Prof. Werner Mäntele, Prof Josef Wachtveitl and Prof. Klaus Fendler for devoting their considerable time to take part in my thesis committee meetings.

I am very grateful to Dr. Alexander Haas for his sincere help and teaching in FTIR experiments at the initial stage of the project.

I thank Prof. Petra Hellwig (CNRS-Université de Strasbourg) for the fruitful collaboration, for all help in performance of the Far IR experiments and for valuable suggestions about manuscript.

I would like to thank Dr. Christian Bamann for carrying out the synthesis of the caged fumarate and an active collaboration on project and all valuable suggestions about manuscript.

Very special thanks go to Dr. Sergiu Amarie and Dr. Enela Džafić and for their collaborative support in different projects.

I thank Prof. Herald Schwalbe for his collaborative support in the caged MMAN project and especially Dr. Hamid Nasiri for synthesising the cage compound.

I thank all members of the Lancaster's group, in particular Florian Müller, Philipp Schleidt, Manuela Busch, Dr. Gregor Madej, Dr. Hanno Juhnke and Dr. Elena Herzog for their help in a very friendly lab atmosphere, advice and company they gave me over these years in every stages of the PhD.

Thanks to Ms. Nicole Hilgendorff for excellent technical assistance and for providing *W. succinogenes* QFR samples.

I thank Mrs. Barbara Schiller for helping with computational hardware and software.

I would like to thank MPIBP library stuffs for providing an excellent, timely and significant help during my research work. The ever-smiling stuffs would oblige for all our requests including books and journals from various other sources. This is the first time I have come across such a well-maintained library.

I thank all the department of Molecular Membrane Biology for their interest and their support, in particular Dr. Devrishi Goswami for all support and true friendship demonstrated in and outside the institute.

I thank Dr. Goerg Wille and Dr. Gabriela Schäfer from the Institute for Biophysics, Johann Wolfgang Goethe University for their help in FTIR experiments.

My sincere thank goes to all my friends who are living in India or aboard, especially Dr. Santanu Pal, Dr. Subhas Pan, Anirban Roy and RudraSekhar Manna for being close to me during my staying in Germany and for making me feel at home.

Financial support by the DFG collaborative research centre SFB 472 on "Molecular Bioenergetics", by the DFG Cluster of Excellence "Macromolecular Complexes", by the International Max Planck Research School on the "Structure and Function of Biological

Membranes”, by the Volkswagen Foundation, the CNRS, the Agence National de Recherche, and by the Max Planck Society is gratefully acknowledged.

Last but not the least, I especially would like to thank my beloved parents and my younger brother, for giving me their all well wishes in every situations, when we were near or far, at present and in the past, throughout all my life. I have been greatly influenced by their valuable suggestions and thought provoking advices.

**Rajsekhar Paul**

## 9 Curriculum Vitae

**Name** Rajsekhar Paul  
**Birth** October 11, 1980; Burdwan / West Bengal Province, India  
**Nationality** Indian  
**E-mail** paulrajsekhar@gmail.com

### July 2010 – March 2011

#### Hoffmann-La Roche Ltd., Basel, Switzerland

Lab-head scientist, Formulation R&D Biologics (early stage)

### July 2008 – June 2010

#### Hoffmann-La Roche Ltd., Basel, Switzerland

Postdoc fellow in therapeutic antibody research

### August 2004 – June 2008

#### Max Planck Institute of Biophysics, Frankfurt am Main, Germany

(Johann Wolfgang Goethe University, Frankfurt am Main, Germany)

#### Ph.D. in Biophysics

Supervised by: Prof. Dr. C. Roy D. Lancaster

**Dissertation:** "From static difference to time-resolved spectroscopy of coupled electron and proton transfer in the quinol:fumarate reductase of *Wolinella succinogenes*".

### 2001 – 2003

#### University of Calcutta, Kolkata, India

#### M. Sc. in Chemistry

*Major Field:* Physical Chemistry

*Minor Field:* Organic, Inorganic & Analytical Chemistry.

*Masters Thesis:* "Crystallography & modelling study of association pattern of organic molecules of biological importance and crystal-engineering". Summer project, 2002, Department of Biophysics, Bose Research Institute, Kolkata, India

*Honours:* 1<sup>st</sup> class

### 1998 – 2001

#### University of Calcutta, Kolkata, India

#### B. Sc. in Chemistry (Honours)

*Areas of concentration:* Physical, Organic, Inorganic & Analytical Chemistry,

*Minor Field:* Physics, Mathematics, Environmental science, English & Bengali

*Honours:* 1<sup>st</sup> class